



NRL/MR/6720--04-8750

Advanced Radiation Theory Support Annual Report 2003, Final Report

*Radiation Hydrodynamics Branch
Plasma Physics Division*

April 19, 2004

20040503 091

Approved for public release; distribution is unlimited.

REPORT DOCUMENTATION PAGE				Form Approved OMB No. 0704-0188	
Public reporting burden for this collection of information is estimated to average 1 hour per response, including the time for reviewing instructions, searching existing data sources, gathering and maintaining the data needed, and completing and reviewing this collection of information. Send comments regarding this burden estimate or any other aspect of this collection of information, including suggestions for reducing this burden to Department of Defense, Washington Headquarters Services, Directorate for Information Operations and Reports (0704-0188), 1215 Jefferson Davis Highway, Suite 1204, Arlington, VA 22202-4302. Respondents should be aware that notwithstanding any other provision of law, no person shall be subject to any penalty for failing to comply with a collection of information if it does not display a currently valid OMB control number. PLEASE DO NOT RETURN YOUR FORM TO THE ABOVE ADDRESS.					
1. REPORT DATE (DD-MM-YYYY) 19 April 2004		2. REPORT TYPE Memorandum report		3. DATES COVERED (From - To) 1 October 2002-30 September 2003	
4. TITLE AND SUBTITLE Advanced Radition Theory Support — Annual Report 2003, Final Report				5a. CONTRACT NUMBER	
				5b. GRANT NUMBER	
				5c. PROGRAM ELEMENT NUMBER	
6. AUTHOR(S) J. Davis, J.W. Thornhill, J.L. Giuliani, J.P. Apruzese, Y. Chong, R.W. Clark, A. Velikovich, P. Kepple, A. Dasgupta, and R.E. Terry				5d. PROJECT NUMBER	
				5e. TASK NUMBER	
				5f. WORK UNIT NUMBER	
7. PERFORMING ORGANIZATION NAME(S) AND ADDRESS(ES) Naval Research Laboratory, Code 6720 4555 Overlook Avenue, SW Washington, DC 20375-5320				8. PERFORMING ORGANIZATION REPORT NUMBER NRL/MR/6720--04-8750	
9. SPONSORING / MONITORING AGENCY NAME(S) AND ADDRESS(ES) Defense Threat Radiation Agency 6801 Telegraph Road Alexandria, VA 22310				10. SPONSOR / MONITOR'S ACRONYM(S)	
				11. SPONSOR / MONITOR'S REPORT NUMBER(S)	
12. DISTRIBUTION / AVAILABILITY STATEMENT Approved for public release; distribution is unlimited.					
13. SUPPLEMENTARY NOTES This research was sponsored by Defense Threat Reduction Agency under JO title, "Plasma Radiation Theory Support," MIPR No. 03-2045M.					
14. ABSTRACT This report describes the work of the Radiation Hydrodynamics Branch during FY 2003 in support of the DTRA PRS Program. Critical issues covered are (1) issues and directions for future research, (2) zero- and one-dimensional modeling of DQ experiments, (3) enhanced energy coupling and x-ray emission in z-pinch implosions, (4) confinement and compression of magnetic flux by plasma shells, and (6) flashover and energy coupling in the DQ machine.					
15. SUBJECT TERMS Decade; Enhanced energy dissipation; Flux compression; Large radius implosions; Transport coefficients; Long time implosions; Rayleigh-Taylor instability; Plasma radiation source; Radiation MHD; Z-pinch physics					
16. SECURITY CLASSIFICATION OF:			17. LIMITATION OF ABSTRACT UL	18. NUMBER OF PAGES 103	19a. NAME OF RESPONSIBLE PERSON J. Ward Thornhill
a. REPORT Unclassified	b. ABSTRACT Unclassified	c. THIS PAGE Unclassified			19b. TELEPHONE NUMBER (include area code) (202) 404-4383

CONTENTS

Executive Summary	v
I. Key Issues and Future Directions in PRS Research	1
II. Zero- and One-Dimensional Modeling of DQ Experiments	7
III. Enhanced Energy Coupling and X-ray Emission in Z-pinch Plasma Implosions	21
IV. Confinement and Compression of Magnetic Flux by Plasma Shells	64
V. Two and Three Wire Loads for Large Current Machines	77
VI. Flashover and Energy Coupling in the DQ Machine	90
VII. Gas Puff Nozzle Design for Argon Z Pinches Using Mach2 Simulations	96

EXECUTIVE SUMMARY

This report describes the theory support of DTRA's Plasma Radiation Source (PRS) program carried out by NRL's Radiation Hydrodynamics Branch (Code 6720) in FY 2003. Included is work called for in DTRA MIPR 03-2045M - "Plasma Radiation Theory Support". This work was also partially supported by Sandia National Laboratories as part of its high energy density physics campaign.

This year Code 6720 assumed partial responsibility for coordinating/planning DTRA's Analysis and Modeling Working Group meeting. As part of this effort a meeting was organized and held on May 22, 2003 in Colorado Springs. The purpose of the meeting was to review and discuss the physics and engineering issues affecting long implosion, 12 cm diameter nozzle, experiments on DE and DQ. In addition, recommendations for the priority issues to be studied in the series of DE and DQ experiments to be performed in the later half of 2003 were made. The minutes and recommendations of this meeting are reported in Section (I) of this report. The remaining six sections, three of which (III) - (V) have been submitted for journal publication, are summarized in the proceeding paragraphs, as follows:

(II) To help achieve the near term goal of 40-60 kJ of Ar K-yield on Decade Quad the 2003 DQ experiments are analyzed from a 0D and 1D model perspective, beginning with a discussion of the analyzes that was provided to the PRS community prior to the 2003 DQ shots. These analyzes are then updated to account for the reduced current that was delivered to the experimental loads. There is substantial contrast between the two perspectives. The 0D model supports the contention that the 12 cm diameter nozzle's performance on DQ was significantly degraded from its performance on DE. On the other hand, the 1D model assessment is that the 12 cm diameter nozzle performed similarly on both machines. In general the 1D yield results followed the same trend as found in the experiments. Both models show that in excess of 9 kJ/cm of K-shell emission is potentially achievable with a 12 cm diameter DQ nozzle at the present level of current delivery from DQ.

(III) Recent experiments conducted on the Saturn pulsed-power generator at Sandia National Laboratories have produced large amounts of x-ray output, which cannot be accounted for in conventional MHD calculations. In these experiments, the Saturn current had a rise-time of 180 ns in contrast to a rise-time of 60 ns in Saturn's earlier mode of operation. In both aluminum and

tungsten wire-array Z-pinch implosions, 2 to 4 times more x-ray output was generated than could be supplied according to one-dimensional magneto-hydrodynamic calculations by the combined action of $\mathbf{j} \times \mathbf{B}$ acceleration forces and Ohmic heating. In this section, we reexamine the problem of coupling transmission line circuits to plasma fluid equations and derive expressions for the Z-pinch load circuit resistance and inductance that relate these quantities in a 1-D analysis to the surface resistivity of the fluid, and to the magnetic field that is stored in the vacuum diode, respectively. Enhanced energy coupling in this analysis, therefore comes from enhancements to the surface resistivity, and we show that plasma resistivities approximately three orders of magnitude larger than classical are needed in order to achieve energy inputs that are comparable to the Saturn experimental x-ray outputs. The challenge to the DTRA program is to channel this energy into enhanced x-ray outputs that are of long term interest to the program.

(IV) Confinement and compression of magnetic flux by plasma shells is of interest for a variety of applications associated with keV x-ray production in pulsed-power driven Z-pinch plasma radiation sources (PRS). Confinement of a field with the field of the pinch current can help stabilize the implosion of a shell from a large initial radius. Compression of the azimuthal magnetic flux in the PRS (secondary) circuit with a plasma shell driven by field of the primary circuit may represent a new opportunity for using low-cost, relatively slow pulsed power to generate large amounts of keV x-rays. The magnetic field has to be compressed and/or confined by low-mass plasma shells emitting soft x-ray radiation that limits the temperature and conductivity of the shell plasma. The thickness of a plasma shell is established self-consistently during the implosion, and it is not obvious that it becomes thick enough to confine or compress the magnetic flux. The results of analytical theory and numerical simulations demonstrate that the flux-compressing capability of a low-beta plasma shell is surprisingly good because the shell is shown to dynamically adjust its thickness so that it always remains of the order of its skin depth. The self-similar profiles of confined magnetic field predicted by the theory are consistently reproduced in the simulations.

(V) Imploding a few high-Z wires at large radius onto a massive wire core is another idea for producing copious amounts of > 5 keV x rays being pursued to meet DTRA's long term goals. In this section energetic implosions using two or three load wires to create a focused axial stagnation of dense wire cores midst the assembled precursor plasma are examined with respect to the trade-

off between the implosion mass lost to precursor ablation and the mass or kinetic energy available at stagnation. The calculated kinetic energy at stagnation serves as the primary source for the output x-radiation.

(VI) The 12 cm diameter argon experimental shots taken during the October 2003 campaign on DQ all exhibited substantial evidence of current flashover at the insulator stack. In this section, the effect of this current flashover on K-shell yield production is analyzed using 1D and 2D radiation MHD models. From this analysis we conclude that, in terms of the general energetics of the flashover event, the K-shell yield attained on DQ was not significantly reduced by the presence of flashovers. This is not to say that azimuthal perturbations and a more pronounced r-z perturbation than were modeled, perhaps brought on by an asymmetric power flow from the flashover or tube misalignment, could not account for the observed yield performance.

(VII) This section is available as a separate document, upon request from Code 6720. It is the Final Report from NumerEx to the Naval Research Laboratory (contract No. N00173-03-P-6201). The title of this document is Gas Puff Nozzle Design for Argon Z-pinches Using Mach2 Simulations. The report discusses the improvements NumerEx has made towards Mach2's capability of simulating the implosion dynamics of a Z pinch. These improvements include: 1) A grid boundary shape created by interpolating along a discrete curve read from a file. 2) Inclusion of a tabular collisional radiative equilibrium model for equation of state and radiation transport. 3) Corrections to the energy-based voltage model for coupling the external circuit to the plasma and diode region for Lagrangian problems, and 4) Determination of the proper plasma-to-vacuum coupling scheme for enhanced circuit-to-simulation coupling fidelity for Eulerian simulations.

I. Key Issues and Future Directions in PRS Research

On May 22, 2003, a DTRA-sponsored meeting was held in Colorado Springs to discuss outstanding issues in PRS physics and possible means of resolving and clarifying those issues via collaboration between experimental and modeling efforts. The meeting was chaired by J. Apruzese of NRL Code 6720. The following is a summary of the meeting and the group's findings.

The emphasis of the PRS Working Group meeting was to share common experiences being gained in physics and technology of long implosions from large radii (within the technical constraints of Double Eagle (DE), which limits K-shell producing implosions to about 260 ns and no more than 12 cm outer diameter) and to formulate recommendations for the future work. Its purpose was

1) Review and discuss:

- the engineering and physics issues to be addressed in long implosion experiments on DE and Decade Quad (DQ) with 12-cm outer diameter nozzles and in the supporting modeling efforts,
- the design aspects of the 15 cm diameter nozzle and its testing on DQ;

2) Develop recommendations for the priority issues to be studied in a new campaign on DE .

The review part included informal status reports and presentations of

- Henry Sze on the TPSD 12 cm diameter nozzle design and performance;
- Phil Coleman on pre-ionization issues
- Bob Terry and Mike Frese on the status of 2-D RMHD modeling in support of DE and DQ experiments

The discussion was focused on the following main topics, which are listed below. Their order corresponds to the community's suggestions for a better understanding for the progress of the PRS program in the immediate future, as established by consensus which involved voting (the voting results are listed at the end of this report):

1. Determination of the optimum mass ratio of shells and central jet (more generally, optimum radial/axial density distributions) for K-shell yield improvement.
2. Determination of how much of the K-shell yield comes from the atoms injected from each plenum (inner/outer shell, central jet), the role of inter-shell mixing.
3. Determination of the fate and role in the implosion of the "dark matter," the plasma mass which does not radiate in the K-shell spectrum.
4. The use of the lower-Z gas in the outer shell to improve yield.
5. Status and the need for pre-ionization.

The main recommendation of the PRS Working Group to DTRA is to provide for an (at least) 7-week experimental campaign on Double Eagle, with associated simulation and analysis, to address the above issues in the order of their priority. There was a general agreement among the participants of the Working Group that a completion of

this study with 12-cm nozzles is a must before meaningful steps towards designing 14-16 cm diameter nozzles for DQ and DE could be taken.

Some other issues addressed in the discussion:

- the role of (enhanced) resistive component in energy coupling to the pinch and its effect on the K-shell yield;
- additional requirements to the load design (including pre-ionization) and performance due to the constraints imposed by the debris shielding task;
- diagnostics (fielding of new diagnostics, restoration of some that already exist).

H. Sze reviewed the 12 cm nozzle design and its characteristics. Recently completed measurements of gas flow in the 12 cm nozzle, with central jet, were described. Combining gas flow timing with a central jet and an appropriate recess of the nozzle with respect to the cathode plane appears to be sufficient to control zippering, which produces a tighter pinch (and a higher power), compared to other 2-shell implosions. High-quality Z-pinchs with short FWHM x-ray pulse widths observed on DE in recent experiments demonstrate significant achievement in the technology. H. Sze indicated that although 300+ ns, 12 cm diameter are not optimal parameters for DE, this facility is the best the community has for studies that require good reproducibility and advanced diagnostics. These results are in a reasonable agreement with the TWG and MKQ scaling models, and translate into a 15-20 kJ/cm prediction of the optimized K-shell yield on DQ, implying over 60 kJ total yields, if the pinch lights up uniformly over its length. (It was noted by C. Coverdale that the proportionality between the yield and the pinch length cannot be taken for granted. P. Coleman reminded the group that uniform K-emission was observed in some DE shots with the 1-2-3-4 nozzle). Topics selected for discussion by the team will build on this achievement, to push the radiative performance to the limit and elucidating the relevant implosion physics.

Preionization

P. Coleman started the discussion of pre-ionization. Study of the pre-ionization issue is important and it can become increasingly more relevant as driving voltage and gas density decrease and initial load radius and implosion time increase. It is still not clear that pre-ionization, as presently conducted, has a consistent effect on implosion dynamics and on radiation yield. The effects may be difficult to measure because of variations in other parameters (e.g., current and mass vary by at least ~5%). [A point was made, that it has not been shown that the radiation from the pinch is azimuthally symmetric – also adding to measurement ambiguities.]

It was agreed that the following describes the state of understanding of the pre-ionization:

- DM2 experiments have shown more consistent K-shell output, when the pre-ionizer was used;
- Some good shots were also obtained without the pre-ionizer;

- Providing the azimuthally uniform pre-ionization can come into conflict with the debris shield technical constraints

It was also suggested that the prepulses, associated with DE and DQ, may be more than sufficient to preionize the gas: on DE, a 5% "toe" current of 200 kA flows through the target ~50 ns before the main pulse; on Z, duration of the 7% "toe" of 1 MA is about the same. Even with a low level prepulse on DQ, 1 % of peak current flows through the load for ~10 ns. To explore further the prepulse-induced pre-ionization may require a bench test, which can simulate current-time characteristics of DQ. Since the main issue here is the reproducibility of the positive effect, if any, of the pre-ionization on the K-shell yield, the results of a considerable number of otherwise identical shots made with and without pre-ionization need to be compared. This translates into a requirement of at least one test week on DE, which should be used by the team for 8 and 12 cm nozzle shots with and without pre-ionization, so as to establish the pre-ionizer's effect. Of course, this study can and should be combined with the study of other issues, like robustness of the optimal mass/density distribution, etc. It was agreed that shots should be properly instrumented so that useful data can be provided to modelers – at this time it is not even clear what pre-ionization levels are being obtained. (B. Weber has measured ~1% ionization, under specific conditions.) R. Terry suggested that if the benefit of the pre-ionizer is inconclusive, then "new technology" could be attempted, such as e-beams or lasers.

Reviewing the status of the 2-D modeling, **R. Terry** highlighted the status of numerical

		Mach2	Delta	1-D Code 6720 NRL
Code Validation, Level 1	Algorithm checks	70 – 100 %	?	100%
Level 2	Physics checks	20 %	?	80 %
Level 3	Design guidance	5 – 10 %	?	50 % * (can not track some of the 2-, 3-D effects)

and physical testing of Mach2 code, incorporation of the NRL radiation physics package into it, and compared the practical applicability of 2-D codes Mach2 and Delta vs. the 1-D RMHD code of NRL Code 6720. The results of his very rough comparison are listed in the table.

M. Frese discussed the recent development of the Mach 2 code and showed the initial predictions for Quad 12 cm nozzle results. He qualified the results, stating that while energy balance is now satisfied in the code; other checks have not been completed. (Present results indicate > 100 kJ of K-shell radiation.) An important result of the Mach 2 effort is ability to model the pinch phase of the implosion. A sample calculation showed the behavior of several quantities, including the K-output rising up after the main pulse. **S. Chantrenne** reported a number of simulations of the Ar shots on DE performed by herself and P. Steen using their version of Mach2 code and the simulated gas density profiles produced by the Delta code. Their results for total mass scan of the K-shell yield were in good agreement with P. Coleman's experimental data.

Optimal mass distribution, origin of K-shell emission, mixing, etc.

Discussion of this issue started with P. Coleman's remark that the DTRA community is not ready to design and build a 15 - 16 cm diameter nozzle. The essential physics needed to make such a nozzle work as a good radiator is not yet fully understood. Do we need a uniform fill? A gentle gradient peaked near the axis? Two concentric shells imploding on a central jet? H. Sze noted that precisely for this reason we need to learn as much as possible experimenting with the 12-cm diameter nozzle on a well-diagnosed driver, DE. It is necessary, in particular, to observe the structure of K- and L-shell radiating plasma, to reliably measure these yields, as well as the total yield (P. Coleman). Large radii and >2 cm lengths are favored for DH. The presumed benefit of this approach is that the radiation output from such a PRS could contain 20 - 40 % energy in the K region of the spectrum. The main issue is to determine the optimum distribution of mass.

H. Sze suggested that the team proceed with optimization of mass distribution and diagnose the shell dynamics (compression, mixing), including distributions with a central jet. Doping separate shells with Freon and, possibly, with H_2S should answer question with regard to which mechanisms optimize the yield. Estimated number of DE shots is 50. R. Terry commented that it is not clear that multiple shells produce higher yields, compared to solid fills.

The mass optimization effort, taken together with measurements of the ratio of the K-to-total yield, will also show how this affects the DMS design.

Non-radiating ("dark") mass

It is also necessary to know the amount of initial mass that does not participate in K-shell radiation, since it appears to be a significant fraction of the total. This issue is related to current sheath thickness, that if controlled (and this may be very difficult), could produce better yields and/or better K/total ratio. A question remains: if 100 % of mass could be made to radiate - how much would be the increase in the yield? A possible channel for loss of mass - through the pinch ends has been partially tested (P. Coleman), by looking outside the anode with a camera in the visible. The camera showed no light there. M. Krishnan noted that the mass left behind (whose presence is indicated by simulation and some experimental data, mostly from wire array experiments on MAGPIE and Z) should have been seen on the interferograms, which has not been the case.

H. Sze proposed 2 weeks of DE testing be devoted to this problem. A key diagnostic would be the L-shell imaging and spectroscopy. Existing atomic data bases at NRL would have to be enhanced to properly interpret the data obtained in such a campaign.

Low-Z Outer Shell

The reason for considering this issue is that the outer, poorly radiating shell, may act as an initial current carrier, which gets switched to the Ar shell, allowing it to compress rapidly. The shorter conduction in Ar may produce a better pinch, utilizing the

total mass. Previous Titan results, using low Z outer shell have, have shown, that in 200 ns implosions, the yield decreases, as the mass of the H₂ shell increases to 50 % of the total mass. The same was seen by Shishlov in Toms. He qualified his results with a possibility that it was not clear what the initial conditions were; possibly, the fast flow put hydrogen gas in places where it diverted the current from the implosion.

To follow up this line of thought, it was suggested that this approach should be tried with higher Z gasses (CH, CO₂, N₂, O₂)

Enhanced energy coupling.

Experiments have shown that the total radiation from the pinch, in many cases, exceeds the JxB energy derived from the magnetic field surrounding the implosion. Additional energy can be derived from the magnetic energy stored in external inductances, if the pinch has a resistive component. Such effects were seen in Z experiments and in Shishlov's low current (400 kA) implosions, where the resistive component was measured. It is not clear, whether the increased coupling could lead to increased emission of the K-shell lines.

This problem will need to be examined, because the increase in the total radiation would add to significant additional stress of the DMS, or alternately, it may increase the K-emission, producing higher fluence at the test article. If the result of enhanced dissipation is only UV emission, then we might want to minimize it, in order to mitigate the issue of debris shielding. A low-cost approach to addressing this problem (A. Velikovich) would be to improve the accuracy of voltage and inductance measurements on DE, in the same way as implemented by E. Waisman on Z. The effective enhanced resistance should be measured and found consistent with the approximate radial trajectory of the implosion, $r(t)$. These measurements could be analyzed as piggyback experiments on any DE shots.

Diagnostics

The preferred diagnostic for recording the spectra of tracer element lines is the Johann spectrometer (E. Yadlowsky). Detection of the "dark" or "lost" mass would require interferometry and L-shell spectroscopy. It would be most convenient to use radially resolved spectroscopy with McDonald's spectrographs, like the 5-channel spectrograph used at Sandia. Bare bolometers need to be fielded to measure the total radiation yield (P. Coleman). Since the voltage measurements are much less reliable on DE than on Z, this need to be improved, at least by adding shielded B-dot probes (M. Krishnan).

Prioritization

At the end of the meeting, the above topics were prioritized by voting by selecting two subjects most important for the community to address. Each participant voted for two topics of greatest importance.

Topic	Number of votes
Optimizing mass ratio	12
K-emitting shell	9
Non radiating matter	8
Low-Z outer shell	2
Preionization	1

Attendees

NRL 6720: J. Apruzese, R. Terry, A. Velikovich

TPSD: H. Sze, B. Failor, J. Levine, S. Chantrenne, P. Steen

AASC: M. Krishnan, P. Coleman, E. Waisman

Numerex: M. Frese, S. Frese

Sandia: C. Coverdale

Hytech: E Yadlowsky

Ktech: D. Lepell

NGIT: I. Vitkovitsky

II. Zero- and One-Dimensional modeling of DQ Experiments

A. Introduction

In this section the results of our 1D modeling of Decade Quad and Double-Eagle 12 cm diameter nozzle experiments are described. This section begins with a discussion of 0D and 1D analysis that was provided to the PRS community before the 2003 DQ shots were performed. The 0D/1D analyses are then updated by taking into account a more realistic assessment of the current that was delivered to the load in the DQ experiments.

The one-dimensional (1D) models are not capable of modeling all the effects present in multi-dimensional Z-pinch plasmas. However, by a judicious choice of transport coefficients (viscosity, heat conductivity, and ion-electron heat exchange), a reasonable match between calculated and measured K-shell yields can be made over a broad range of experimental conditions for a given nozzle configuration. We cannot fully quantify the extent that our phenomenological model captures the physics of actual multi-dimensional plasma implosions, so to some extent any insights gained by this work are inherently speculative. However, for now (until Mach2 is a fully operational code containing adequate radiation physics), this is likely the best modeling that can be accomplished that includes the essential radiation physics of the implosion. For a more complete description of the 1D modeling see the 2002 Annual report.

B. 0D and 1D K-yield assessment prior to 2003 DQ experiments

The scaling of K-shell radiation with current and imploded mass can crudely be modeled using 0D snowplow scaling models. These models reasonably model the implosion time, peak current into the load, and the specific energy of the load. This specific energy is often represented by the η^* parameter, which is the specific energy divided by the minimum energy per-unit-mass needed to instantaneously ionize the plasma into the K-shell. However the scaling of the K-shell radiation with current, which depends so much on the individual load and machine design, has historically been very speculative. Figure 1 shows 0D model predictions for the 2001 argon experiments on Z.

There are two K-shell yield scaling curves shown in Fig. 1. Curve A is generated using the enclosed "old" Z scaling model (Fig. 2), it is a typical 0D model, which has historically been used to predict K-shell yield. This model shows that a 2 mg/cm load is capable of producing about 125 kJ/cm of K-shell emission. Unfortunately, this model does not adequately represent the rapid fall-off in K-shell yield with mass that was exhibited in the Z experiments using the 4-3-2-1 nozzle. This fall off, for which strong evidence was also exhibited in recent DQ and long pulse Saturn 4-3-2-1 nozzle experiments, is likely to limit the mass that can be imploded by DQ and DH to efficiently produce K-shell emission. The effect may be even more pronounced for larger radius loads. There is speculation that this fall off is inherently an instability effect that occurs in the larger radius implosions. This effect has also been discussed in our Final

reports to DTRA since 1998. These reports attribute the fall off to L-shell radiative cooling rates being larger than currently modeled or possibly to substantial mixing which enhances energy exchange between the hot core and the rest of the plasma. Thus, the ionization levels needed to support K-shell emission would diminish faster with increasing mass than presently modeled. This effect is crudely taken into account by assuming that a necessary requirement for two different loads to produce K-shell radiation at the same efficiency is that they must have approximately the same ionization level, which is largely determined by the ratio of plasma heating to cooling. Taking the heating rate at stagnation as being proportional to $1/2 mv^2/\tau$ and the radiative cooling rate as proportional to $mass^2/\tau$, where τ is a thermalization time, this ratio can be simplified to $\eta^*/mass$. Scaling curve B is attained by reducing the K-shell yield of curve A by $(\eta^*/mass)/.00594$, where .00594 is the ratio of η^* (1.7) to mass (286 $\mu g/cm$) that was achieved in the best 4-3-2-1 nozzle DQ argon experiments to date (shot # 498 - 28 kJ K-shell yield), see Fig. 3. Since this adjustment to the original scaling model does a reasonable job of replicating the observed 4-3-2-1 nozzle K-shell yields from DE, DQ, and Z it is a reasonable scaling model for interpolating the performance of 4-3-2-1 nozzle loads on DH. Likewise the model can be used for extrapolating yield predictions to larger radius DQ and DH loads. However because it is an extrapolation into an unknown larger-radius parameter space, one has to be skeptical about any prognostications derived from this model. An example of this 0D extrapolation to DQ with the 6-4-2-1 nozzle is shown in Fig. 4.

Preliminary 1D results for DQ are also shown in Figure 4. These results are based on a consistent set of transport coefficients that not only reasonably replicates the existing 4-3-2-1 nozzle results for DQ and Z but also reasonably replicates, or so we thought at the time the calculations were made, the 6-4-2-1 nozzle DE experiments. This previous statement is qualified because at the time the calculations were made we thought that the inner to outer mass ratio was 1:1, not 1.8:, as used in the DE experiments. Also, the John Riordan version of the open circuit voltage for long pulse Double-Eagle was used, see Fig 5. This voltage profile is not accurate for the longer times needed to model the 12 cm diameter nozzle experiments. To reasonably match this larger parameter space, the enhancement on viscosity had to be increased to 200. This is a factor of 4 larger than was required to match only the 4-3-2-1 nozzle experiments. This factor of 4 produced little effect on 4-3-2-1 nozzle calculations but it dramatically altered the 12 diameter results. The mistakes made in modeling the DE experiments were discovered after the DQ 12 cm diameter experiments were performed. When the more realistic 300 ns DE open circuit voltage profile, see Fig. 5, and proper mass ratio are employed, it was found that an enhancement of 250 on viscosity (factor of 5 over that used to model just 4-3-2-1) experiments was required to best replicate the 12 cm diameter DE experiments as well as the 4-3-2-1 DQ experiments.

Comparing the 1D to the 0D predicted yields shown in Figure 4 reveals that the 1D models predict substantially less K-yield than either our new 0D or old 0D models for the larger mass 12 cm diameter loads. This is a reflection on the fact that the 1D models show that not only are mass and energy important in determining K-yields as do the 0D models, but also the stagnation physics; some of which is presumably captured by the

phenomenological 1D model. The 1D optimal yield is shown to occur at smaller mass load than that of the 0D predictions. All three models show similar yield behavior for mass loads less than 250 $\mu\text{g}/\text{cm}$. The experiments can be assessed in terms of a 0D or 1D model perspective by comparing these results to the experimental data.

C. Experimental Results

Table 1 summarizes the K-shell yield results from the 12 cm diameter nozzle DQ argon experiments as well as a few selected 4-3-2-1 DQ results and DE 12 cm diameter results. Note, the efficiency listed in this table should be interpreted as a relative measure of the efficiency of converting the energy that enters the diode into K-shell emission. Since the amount of compressional work done on each plasma load is not really known, the energy coupled to the load assuming a 10:1 compression is used as a relative figure of merit of the electrical energy that enters the diode. In other words, we really don't know the absolute efficiency, but if one load's quoted efficiency is 10% and another load's is 20%, then one can say that the 20% conversion efficiency load was twice as efficient as the 10% load. Note, the efficiency of the 12 cm loads tended to increase with the specific energy as represented by η^* in Table 1. The highest efficiency attained for the 12 cm diameter nozzle (13.2 percent) was significantly below the best 4-3-2-1 yield (19.5%). A reasonable goal for the 12 cm diameter loads on DE and DQ would be to achieve the same efficiencies that were achieved using the 4-3-2-1 nozzle.

D. Normalized 0D and 1D assessments of DQ 12 cm diameter nozzle experiments

The current that was coupled to the load in the DQ experiments was found to be significantly less than what was predicted by the equivalent circuit model for DQ, see Fig. 5. In order to analyze the results of these experiments from a 0D and 1D perspective it is necessary to recalculate the yields using a circuit model that more accurately matches the peak current delivered to the load. Little sensitivity was found in terms of K-yield to whether the 6-4-2-1 nozzle or the 6-5-3-2 nozzle were modeled. The results presented here are for the 6-5-3-2 nozzle with an initial mass distribution similar to that measured near the cathode plane. The ratio of inner to outer mass was 2.2:1 and the viscosity is now enhanced by a factor of 250. The DQ open circuit voltage shown in Fig. 5 was multiplied by the factor 0.94 in order to reproduce the peak currents in the 0D/1D models that were achieved in the experiments, see Fig. 6. These peak currents are given as a function of load mass. The K-shell yields as calculated by the 0D/1D models with peak currents given by Fig. 6, are compared with experiment in Fig. 7. Note, the implosion times (not shown) were in good agreement with the experiments but they are sensitive to the choice of initial mass distribution. For the purposes of these calculations, which focussed on insuring that the same amount of energy was available to the theoretical loads as the experimental loads, no initial mass was modeled beyond 6 cm radius.

Based on a comparison of experimental and 1D K-shell yields, see Fig. 7, it appears that a reasonable job of phenomenologically modeling some of the large-radius stagnation

physics with our 1D model was accomplished. While the 1D results are ostensibly only for the 6-5-3-2 nozzle with a 2.2 : 1 inner-to-outer mass ratio, there is not much model sensitivity between the 6-5-3-2 and 6-4-2-1 nozzles. Actually the 1D model predicts slightly more yield for shots 547 and 547, which employed the 6-4-2-1 nozzle, than shown in Fig. 7. This is primarily because they were shorter length pinches, 3.7 cm as opposed to 3.9 cm for the Titan experiments. The 1D and experimental yields and trends (increasing yield with decreasing mass) are in excellent agreement for mass loads greater than 300 $\mu\text{g}/\text{cm}$. The only significant deviation between the model and the experiment was for shot #548, which was the lowest mass load (273 $\mu\text{g}/\text{cm}$). Given that the 1D model shows optimal yields for load mass less than 350 $\mu\text{g}/\text{cm}$ and that there is a paucity of experimental data in this mass region (only one shot) – we should be encouraged to thoroughly explore this region experimentally.

E. Tradeoff between stability and energy coupling

The 2004 DE and DQ large radius experiments are going to systematically explore the sensitivity of K-shell yield to the initial mass distribution. Here we examine this issue with the 1D model that has been benchmarked to agree with the 2.2: 1 mass ratio Double-Eagle experiments. In terms of a 1D model perspective, it is generally true that the more energy coupled to the load – the more K-shell emission will be calculated. This is because the 1D models cannot account for effects due to instabilities. For this reason the 1D models will predict that the distribution with the smallest mass ratio will produce the most K-shell emission. In this section we display the calculated yields for Double Eagle and Decade Quad for the 6-5-3-2 nozzle in which the mass distribution is varied from 2.2: 1 inner-to-outer ratio to a ratio of 1 : 2. Presumably the 2.2 : 1 distribution is more stable than the 1 : 2 distribution because more mass is located close to the axis of the pinch. These calculated yields as a function of load mass and distribution are shown in Figs. 8 and 9 for DQ and DE, respectively. Insights into this tradeoff between stability and energy coupling will be obtained by comparing these results with the upcoming experimental results.

Summary

Once benchmarked to the 4-3-2-1 nozzle experiments performed on DE, DQ and Z the 0D model bases all of its K-shell yield predictions on the load mass and energy coupled to the load as calculated by a 10:1 compression ratio. This model can be used to reasonably interpolate yield behavior for the 4-3-2-1 nozzle on Z, DE, DQ and DH. When the 0D model is extrapolated to predict the performance of the 6-5-3-2 nozzle shot #5161 experiment on DE, see Fig. 9, it also does a reasonable job. However, when the 0D model is extrapolated to predict the performance of DQ 12 cm diameter loads. It substantially over predicts the yields for every experimental mass load tested, see Fig. 7. From a 0D perspective one might be tempted to speculate that because the 0D model systematically over predicts the DQ yields, but not DE's, that the DQ load performance was somehow degraded below that of Double-Eagle.

The 1D model uses a different phenomenological approach than the 0D model in order to match the experimental data base. Rather than fixing a compression ratio or ratio of thermalization to radiation rates as is done in the 0D modeling, the 1D model uses a judicious choice of transport coefficients to benchmark to previous experiments. Thus the 1D model bases its results on a self-consistent coupling of load mass, energy coupling, and implosion/radiation dynamics. Here the 1D model was benchmarked to the data base of 4-3-2-1 experiments as well as the shot 5161 DE 6-5-3-2 experiment. Similar to the 0D model, the 1D model can be used to reasonably interpolate yield behavior for the 4-3-2-1 on Z, DE, DQ, and DH. By construction the 1D model does a reasonable job of representing DE shot 5161's yield behavior. However, unlike the 0D model, the 1D model also reasonably predicts, with one exception, the yield behavior of the DQ experiments (Fig. 7). The one exception was DQ shot #548, which was the lowest mass load (273 $\mu\text{g}/\text{cm}$) experiment. Thus, from a 1D perspective one can say, in direct contrast to the 0D perspective, that the 12 cm diameter loads performed nearly the same on DQ as DE.

The 1D model predicts that the highest DQ K-yields, based on past drive currents, will occur for load masses less than 350 $\mu\text{g}/\text{cm}$ and that yields in excess of 9 kJ/cm are attainable. Unfortunately, the yield prediction for shot #548 was 10 kJ/cm and only 7.2 kJ/cm was achieved. Given the power flow problems, and that this was the only shot taken in the range predicted to give the best yields, we should not be overly discouraged by this result. On the other hand it is discouraging that it required 5.5 MA to achieve 28 kJ yield with the 12 cm diameter nozzle while only 4.6 MA was needed to achieve the same yield with the 8 cm diameter nozzle (approximately same mass). Until it is experimentally demonstrated that the deleterious effects on K-yield due to increased radius, such as instabilities, can be overcome by the larger drive currents attainable at large radius, there is no compelling reason to pursue > 12 cm diameter loads.

The 2004 DQ experiments will address this load design issue by mapping out the tradeoff between stability (higher mass ratio) and more current/energy coupling (lower mass ratio) to search for a parameter regime in which substantially more K-shell yield is produced at 12 cm diameter than 8 cm. The 1D model is little help in this regard in that using the 1D model to make yield predictions for mass distributions other than the benchmarked 2.2:1 distribution is suspect (Fig. 8). For this task our 2D model, which is currently being developed, is better suited.

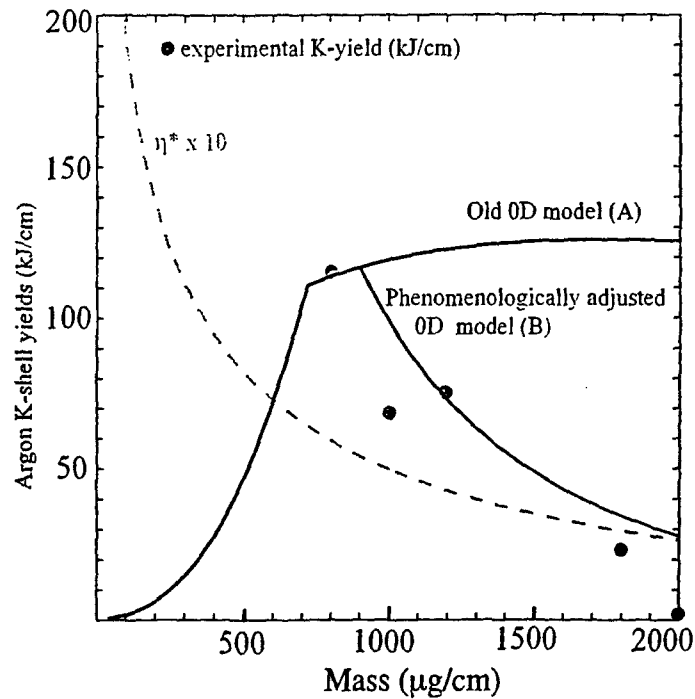


Fig. 1 Calculated and experimental k-shell yields as a function of mass for argon loads on the Z machine. Experimental yields are from 2001 experiments with the 4-3-2-1 nozzle.

Z Scaling of K-shell Emission

(old scaling - taken from Dense Z-Pinches 4th International Conf. pp. 197)
The original published scaling was slightly altered to do a better job of scaling in the low η^* regime. The form currently used is given below:

$$\text{Energy (J/cm)} = (\text{kinetic energy} + \text{internal energy}) \text{ (J/cm)}$$

$$\eta^* = \frac{\text{Energy} \cdot 1.1 \cdot 10^{-5}}{\text{Mass (g/cm)} \cdot Z^{2.41}}$$

Z is the atomic number

$$\alpha = \frac{2.76 \cdot 10^{-12} \cdot Z^{5.96}}{\exp(-20.6/Z \cdot 9)} \text{ maximum } (1.0, \eta^{*2}/(\eta^*+12))$$

$$\beta = \text{minimum of } 0.25 \cdot \text{Energy} \text{ and } \frac{0.3 \cdot \text{Energy} \cdot \text{Mass(g/cm)}}{\alpha}$$

$$\text{K-Yield (J/cm)} = \beta \quad \text{for } \eta^* > 1.75$$

$$\text{K-Yield (J/cm)} = \beta \cdot (\eta^* - 0.75) \quad \text{for } 1.0 < \eta^* < 1.75$$

$$\text{K-Yield (J/cm)} = 0.0 \quad \text{for } \eta^* < 1.0$$

Note, a reasonable approximation for the energy in (J/cm) is given by $I_p^2 \cdot 1800$, which is close to the coupled energy (10:1) compression for most machines. The peak current I_p , is in units of MAs.

Fig. 2

New Z -scaling - phenomenologically
matched to 4-3-2-1 nozzle results

Replace old β by $\frac{\beta \times \eta^*}{\text{Mass } (\mu\text{g/cm}) \times .00594}$

and recalculate K-yield

The maximum efficiency is limited to 18 percent at low η^*
and it is allowed to rise to 27 percent at high η^* .

$$\text{K-yield} = \min(\text{K-yield}, 0.18 \times \text{energy} \times \text{xcon})$$

$$\text{xcon} = \min(1.5, (1. + .6 \times \eta^*/5.0))$$

Fig. 3

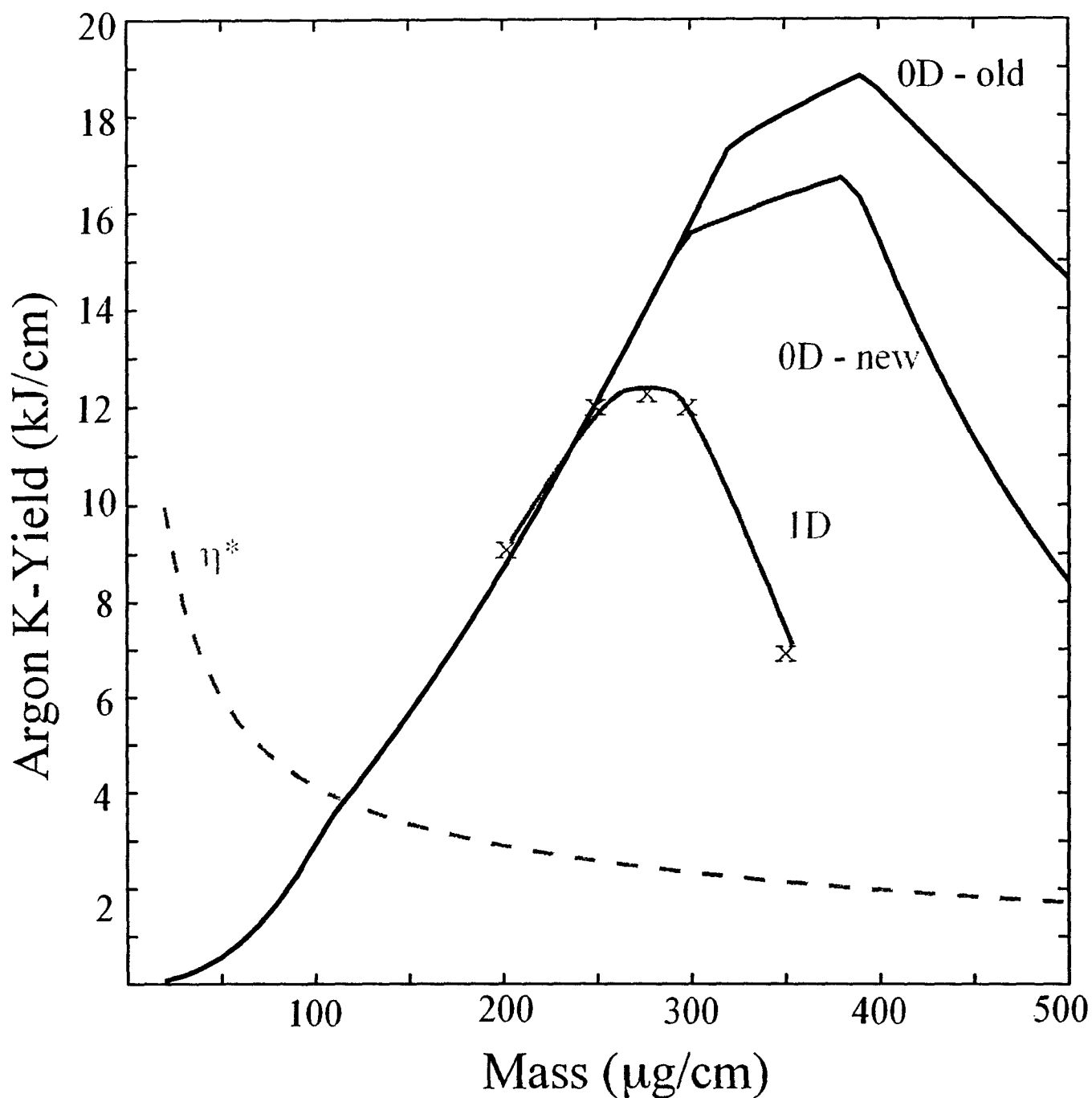


Fig. 4 0D and 1D calculated K-shell yields for DQ with a 12 cm diameter nozzle and assumed inner to outer mass ratio of 1:1 . These calculations were performed prior to the 2003 DQ experiments.

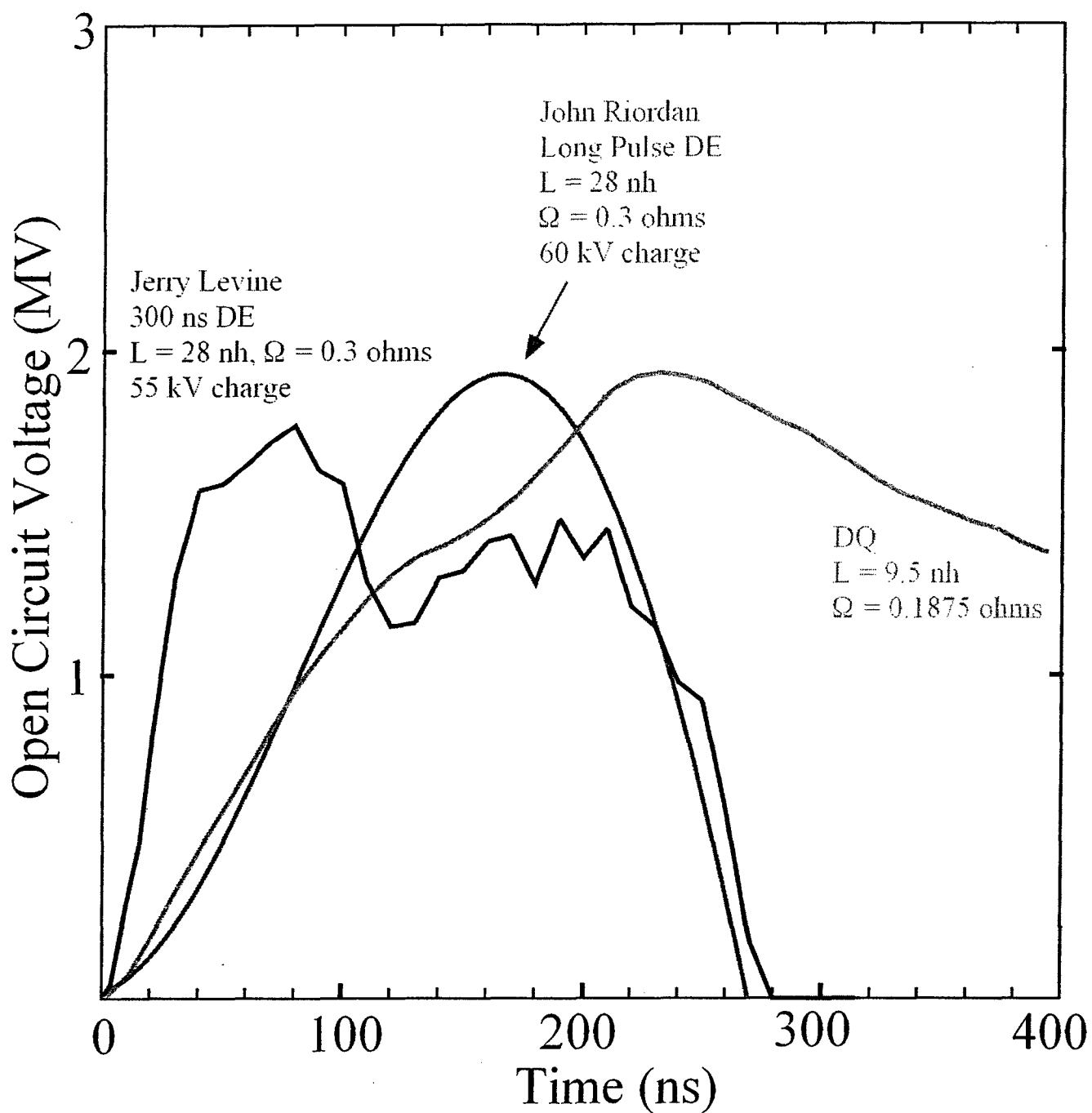


Fig. 5 Double-Eagle and Decade Quad open circuit voltage profiles and circuit parameters.

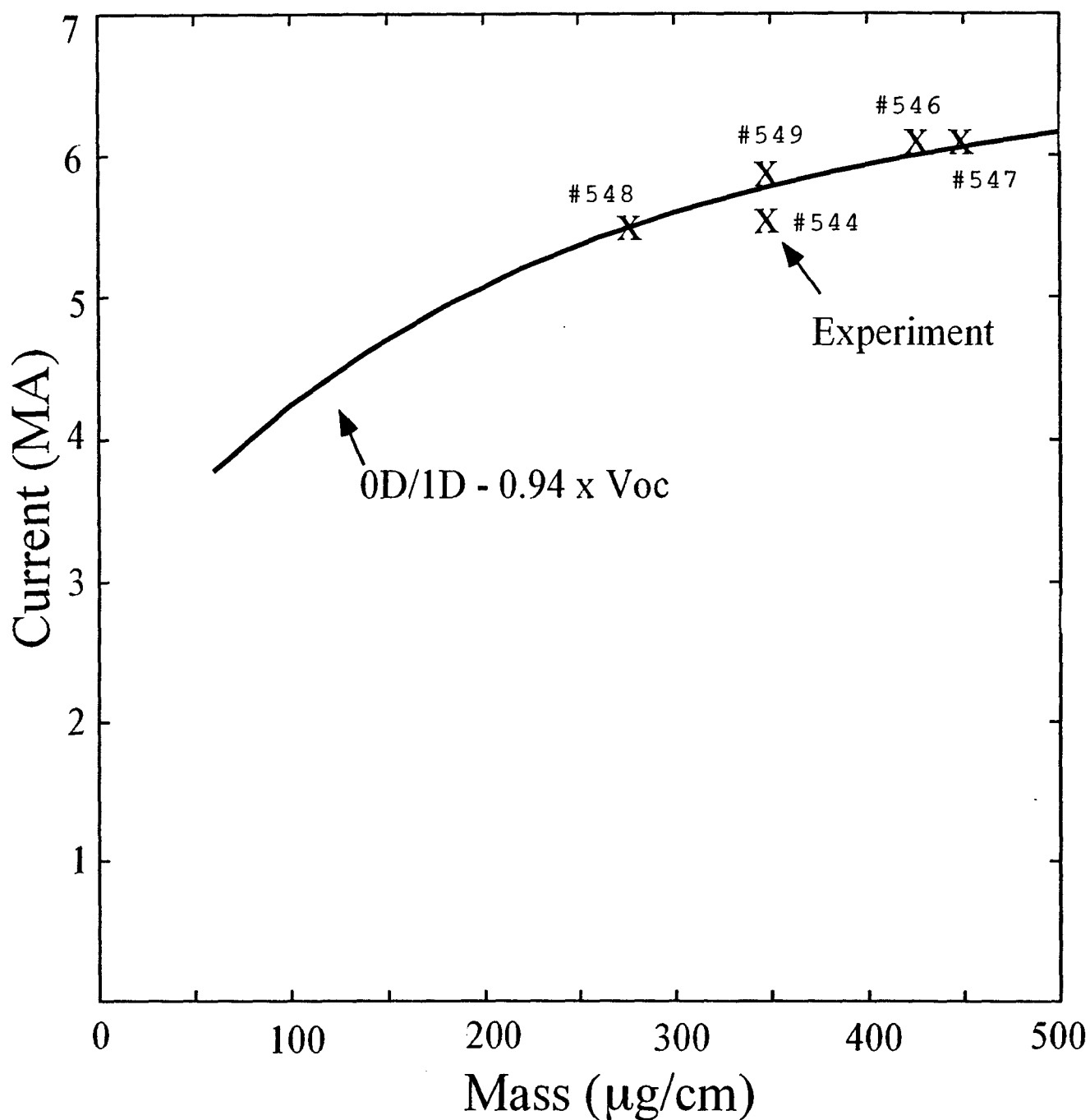


Fig. 6 Calculated and experimental peak currents as a function of load mass for 6-5-3-2 nozzle on DQ. The modeled and experimental inner-to-outer mass ratio is 2.2 : 1.

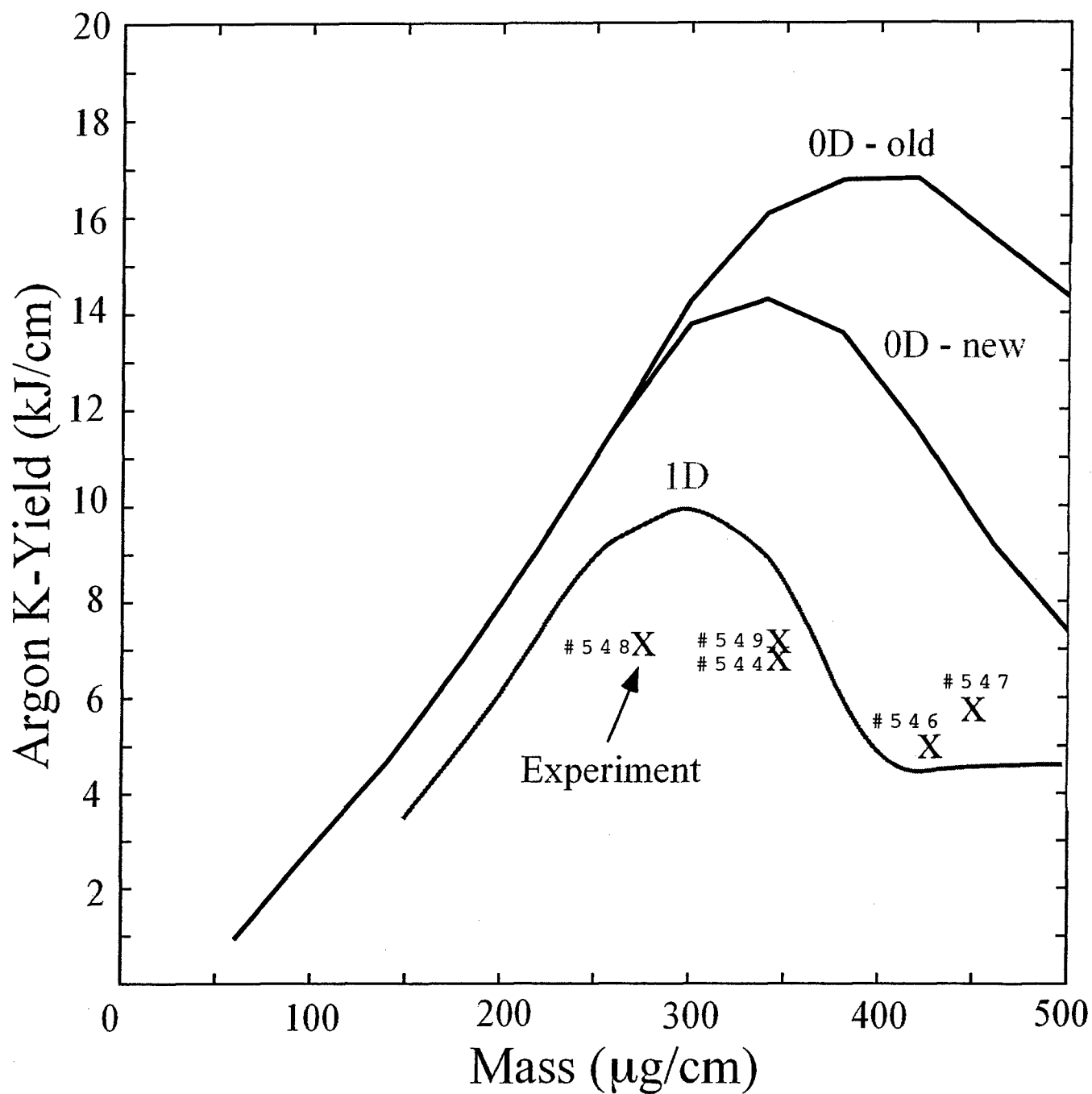


Fig. 7 0D and 1D calculated K-yields as a function of mass for 6-5-3-2 nozzle with 2.2 : 1 inner-to-outer mass ratio. The DQ 12 cm nozzle results are also shown for comparison. Only shots 548, 549 and 544 had a 2.2 : 1 mass ratio.

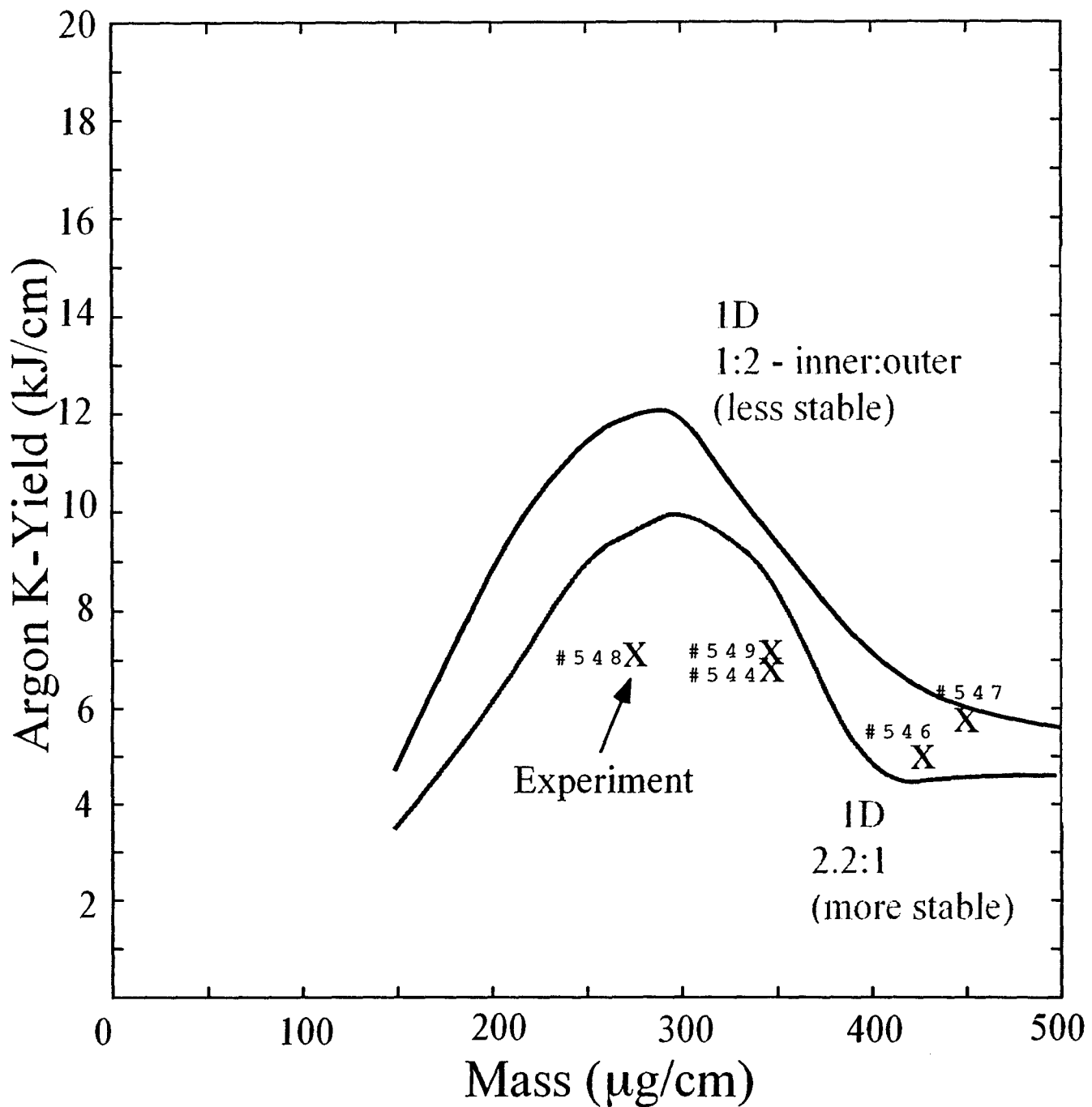


Fig. 8 1D calculated K-yields for 6-5-3-2 nozzle as a function of mass and inner-to-outer nozzle mass ratio on Decade Quad. Experimental results are also shown. Shots 548, 549 and 544 were 6-5-3-2 experiments with 2.2:1 mass ratio. Shots 546 and 547 were 6-4-2-1 experiments with 1.4:1 and 1.8:1 mass ratios, respectively.

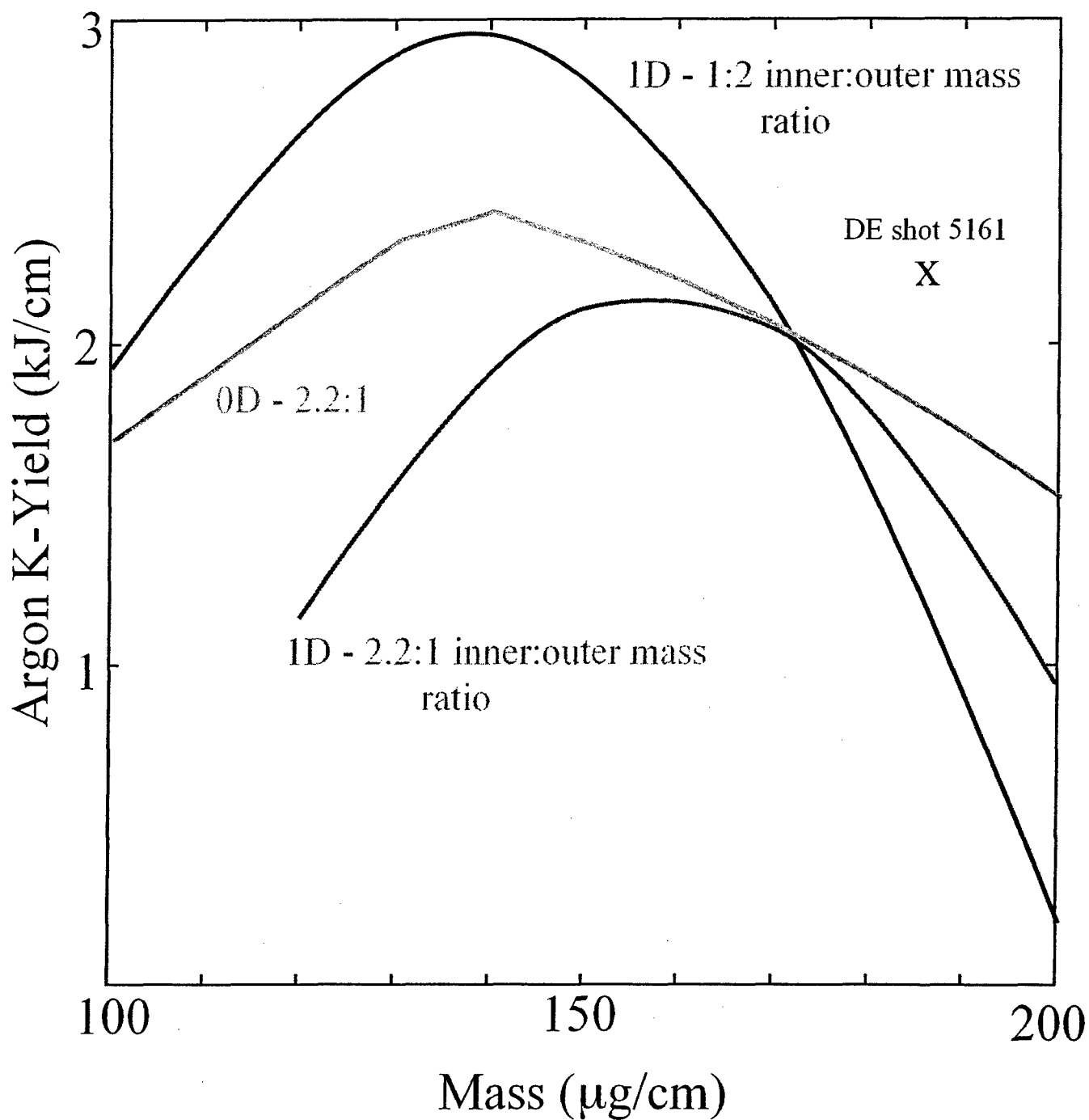


Fig. 9 1D and 0D calculated K-shell yields as a function of mass load and mass distribution. The 6-5-3-2 nozzle is modeled in these calculations.

Table 1

Shot	Mass ($\mu\text{g}/\text{cm}$)	length (cm)	I peak (MA)	K-yield (kJ)	η^*	ϵ (%)
498 (tpsd-8)	286	3.8	4.64	28.7	1.45	19.5
543 (tpsd-8)	443	4.0	5.06	17.4	1.11	9.4
544 (tpsd-12)	348	3.9	5.65	26.1	1.76	11.6
545 (tpsd-12)	348	3.3	5.78	26.2	1.84	13.2
546 (aasc-12)	425	3.7	6.14	18.9	1.70	7.5
547 (aasc-12)	450	3.7	6.15	21.5	1.61	8.5
548 (tpsd-12)	273	3.9	5.53	28.1	2.15	13.1
549 (tpsd-12)	348	3.9	5.83	28.1	1.88	11.8
5161(DE-12)	185	3.8	3.47	9.0	1.25	10.9
4428(DE-4321)	113	4.0	3.7	12.0	2.33	12.5
5134(DE-4321)		3.8	3.8	18.0		18.2

III. Enhanced energy coupling and x-ray emission in Z-pinch plasma implosions

I. INTRODUCTION

The short-circuit current risetime of the Saturn generator at Sandia National Laboratories was recently increased from ~ 60 to ~ 180 ns in order to investigate the effect of current risetime on the implosion dynamics of Z-pinchs. The effect was large. In both aluminum and tungsten wire experiments, significant increases in total x-ray output were observed [1-3] compared to the earlier outputs that were seen in short current-risetime Saturn experiments. Present magnetohydrodynamic (MHD) calculations are unable to generate such yields because the amount of x-ray energy radiated in the experiments is significantly larger than the sum of the $\mathbf{j} \times \mathbf{B}$ work and Ohmic heating calculated using the Saturn circuit model. Such energy discrepancies between Z-pinch calculations and experiment have existed for some time [4-7], but not to the degree seen in these experiments. The energy inputs calculated for these experiments in a one-dimensional (1-D) MHD are in deficit by factors of 2 to 4. Such energy discrepancies pose serious theoretical challenges even as they offer new possibilities for increasing x-ray extraction efficiencies.

In early work on imploding Z pinches, it was observed that the total radiation yield could exceed the 0-D or 1-D estimates of radial kinetic energy by roughly 50%. Giuliani, et al. [8] suggested that enhanced or anomalous resistivity could explain this discrepancy. Peterson, et al. [9] subsequently showed that 2-D MHD calculations could increase the coupled energy by more than a factor of two over the 0-D and 1-D kinetic energy couplings by accounting for mass distributions in the radial and axial directions that lead to reduced peak radial kinetic energy but significantly more pdV work. Initial 2-D calculations of the long current-pulse Saturn experiments [10], however, indicate that they cannot reproduce the high energy coupling and hence the x-ray output seen in these experiments. Further

evidence that significant energy coupling occurs through other than radial kinetic energy generation and pdV work comes from a single wire experiment described in Ref. ([11]). The total energy radiated in this experiment was found to be comparable to that measured in a set of imploding array experiments, even though the recorded pinch sizes were comparable in all cases.

A theoretical mechanism was recently proposed in which energy coupling to a Z-pinch is increased through the generation and storage of additional amounts of magnetic field energy in the Z-pinch plasma. The dissipation of this energy then increases the energy coupling to the plasma [6,7]. It was hypothesized that tubes of magnetic flux build-up within a pinch as an additional effect of Rayleigh-Taylor or $m=0$ instability growth at the surface of the plasma. If tubes of magnetic flux were to form and be trapped within the plasma, the currents that produce them would decouple from the circuit current and effectively increase the energy coupling between the Z-pinch and the generator transmission line. In this paper, however, a different approach to enhanced energy coupling is investigated. First, the problem of coupling transmission lines to Z-pinch plasmas is analyzed. In a 1-D hydrodynamics calculation, this analysis relates the strength of the energy coupling to the plasma's surface resistivity. Hence, enhanced coupling occurs because of increased surface resistivity.

A mechanism for increasing the electron collision frequency at the surface of a pinch was proposed in Ref. [12]; namely, that currents flowing in the low density plasma at the pinch surface acquire drift velocities that can greatly exceed the sound speed. This event leads to the build-up of micro-instabilities that increase the plasma's resistance to the current flow and that inhibit further growth in the drift velocity. How this mechanism operates in detail has yet to be worked out. Consequently, the approach adopted in this paper was to increase energy coupling by phenomenologically increasing the strength of the surface resistivity. The kind of increases that could be applied were guided entirely by the x-ray data obtained in the Saturn experiments.

This data was obtained from three identically configured aluminum wire experiments and is presented in section II. While the three aluminum shots were ostensibly identical, the

x-ray data they produced was not. Large shot-to-shot variations were seen indicating (1) possible small differences in the wire loads or in the Saturn machine operation, or (2) a high level of randomness or sensitivity to the wire breakdown conditions in the experiments, or (3) a high level of sensitivity to the onset of the resistivity changes. In one shot, the total radiated yield was a factor of two larger than in the other two shots, and, in all three shots, significantly more energy was radiated than could be accounted for by conventional MHD resistivity theory.

In section III, the problem of coupling circuit equations to fluid equations is investigated. Under the assumption that the fluid dynamics is one-dimensional, we show that an analytic expression for the circuit resistance and inductance is derivable in terms of surface fluid quantities. The resistance is found to depend on both the surface resistivity and the surface current density of the pinch. Because increases in resistivity increase the rate of current diffusion, the current density at the surface, on which the energy coupling also depends, is lowered. Thus, the energy coupling problem is nonlinear, and MHD calculations are needed to quantitatively assess how increases in circuit resistance actually affect the fluid dynamics. These calculations are described in section IV. Two of the problems investigated in sections IV concern (1) the time history of circuit resistance needed to approximately model the Saturn experiments and (2) the sensitivity of the calculations to variations of this time history.

The Saturn experiments manifest enhanced energy coupling because they produced enhanced x-ray outputs. Thus, fluid calculations must also demonstrate this capability. Some of the modeling issues that this energy channeling raises are investigated in section IV. It is found that, under certain dynamical assumptions, the calculations can convert substantially all of the input energy into x-rays, but not otherwise. Moreover, the x-ray pulses observed in the Saturn experiments, both as to their energy content and the presence or absence of sizable amounts of emission following the main x-ray pulse, are found to correlate well with the assumed behavior of the circuit resistance. Thus, the calculations serve to identify a variety of important issues related to the modeling of Z-pinch dynamics.

Finally, a formula for enhanced resistivity produced by the growth and saturation of a hybrid drift-wave instability [12] is tested in section V by post-processing the principal calculation described in section IV. In this one case, the resistivity increases predicted by the formula do not support the resistivity assumptions that were made in the calculations. By a significant amount, they are neither large enough nor do they occur early enough to offer support to the resistivity assumptions that were built into the calculations. This work is then summarized in section VI.

II. EXPERIMENTAL DATA

Saturn generates sufficient current to drive large wire-number aluminum loads with small interwire gap spacings from radii of two or more centimeters when it is operated in a long current-risetime mode. Small gap spacings, in principle, allow plasma shells to form prior to wire implosion, and these shells implode with greater azimuthal symmetry than when gaps remain present during the run-in. For the aluminum wire shots performed on Saturn in this long current-risetime mode of operation, a gap spacing that produced the most symmetric shell, and thus the most x-ray output, was first empirically determined. This was done by selecting a wire number that maximized the total x-ray power output from a series of aluminum wire experiments in which only the wire number and wire diameter of the arrays were varied while the array mass was kept fixed [2,3]. In these shots, the arrays were 2 cm long, 4 cm in diameter, each contained approximately $616 \mu\text{g}/\text{cm}$, and the wire numbers were 32, 56, 70, 126, 180, and 282. The highest x-ray power was obtained from the 180 wire load. This load was chosen for our 1-D analysis since (1) the pinch had the largest compression and hence, it was the closest to 1-D, i.e., it had the minimum of wire array dynamics and (2) the short x-ray pulse minimized errors in inferring an implosion time. However, this power was highly variable. When the 180 wire shot was repeated 2 more times, large variations in the total x-ray power were observed (Fig. 1). The shots had nearly identical implosion times (± 2 ns), but their x-ray pulses are shifted in Fig. 1 for clarity. However, in shot 2693, the

peak x-ray intensity was twice that measured in the other two shots, and the power pulse had a substantial late-time tail. Shot 2706 also had a late-time tail; however, shot 2636 did not. Similar, but smaller, variations in time were evident in the recorded aluminum K-shell emissions, which are shown in Fig. 2.

Running time integrations of the Fig. 1 powers, which are shown in Fig. 3, produced equally large variations in the total energy radiated, both during and after the main pulse. Twice the energy was radiated in shot 2693 than in the other two shots, but half of this energy was late-time. Shot 2706, on the other hand, had half the energy in its main pulse as shots 2693 and 2636 did, although eventually the same total amount of energy was radiated as in shot 2636. Approximately the same amount (~ 500 kJ) of energy was radiated in the main x-ray pulse of shot 2636 as was seen in the total emissions from shot 2693, but shot 2636 produced essentially no late-time emission.

Initially, when an analysis of Saturn shots 2636, 2693, and 2704 was carried out using a conventional 1-D magnetohydrodynamics (MHD) calculation based on classically calculated transport coefficients [13] and the Saturn circuit model, two to four times more energy was found to be radiated in the experiments than had been supplied in the calculation. The large energies that were radiated in the experiments imply that even larger amounts of energy had coupled to the pinch. As our analysis will show, the pinch had to have a higher impedance than the conventional 1-D calculation had predicted.

A direct measurement of impedance in experiments conducted on the Tomsk IMRI-IV generator [14] had confirmed that large increases in resistivity, and therefore in energy coupling, were taking place late in the pinch implosion as it began to assemble on axis. The calculations described in section IV of this paper are guided by this observation as well as by the x-ray data in Figs. 1-3 from shots 2636, 2693, and 2704. Large increases in the resistance of the plasma as seen by the circuit were introduced into these calculations slightly in advance of pinch assembly, and the turn-on time was taken to be relatively short in accord with the Tomsk experiments and with the Saturn x-ray data. How these resistance increases were made in the calculation is explained in the following section, where

the problem of coupling a set of 1-D fluid equations to a transmission line is examined and a formula relating the circuit resistance to the surface values of the plasma resistivity and current density is derived.

III. ENERGY COUPLING THEORY

The coupling of pulsed-power generators to Z pinches is usefully addressed by separately considering the dynamics of the generator, the diode region, and the Z pinch. Maxwell's equations imply that transmission line energy couples to a pinch at its outer boundary. The location, $b(z, t)$, of this boundary as a function of time is, therefore, an important coupling parameter even though it may not be an easily definable, physical variable. Most theoretical analyses, however, assume it to be well defined. In a non-fluid, slug model description of Z-pinch implosions [15], for example, the pinch boundary is the only variable employed. It is also an important variable in the definition of self-similar solutions, which are used in a variety of approximate hydrodynamics descriptions of Z-pinch dynamics [16]. It was also the important variable in a recent analysis of the free surface dynamics of an ideal fluid consisting of imploding wire-like plasmas [17]. It was used to describe the radiative collapse of hydrogen and helium Z pinches [18], and it is the key variable in the original work of Bennett [19], Pease [20], and Braginskii [21] in their early treatment of Z-pinch equilibria. It is less well defined in more recent treatments of this problem, such as the work on gas-imbedded Z pinches [22] or on Bennett equilibria as it is modified once microturbulence limits are set on the current flow [12]. Most importantly, the outer pinch boundary is sharply defined (minus the presence of coronal plasmas) in all MHD computer calculations of Z-pinch plasma implosions, and it will be assumed to be equally well-defined in the analysis that follows.

A. Generator

The Saturn generator is a voltage-source driven transmission line in which electromagnetic energy flows to, couples to, and reflects from the Z-pinch load. Generally, however, the

generator is modeled as a lumped circuit in which a voltage, $V(t)$, with a given (measured) time history drives a time varying inductance, $L(t)$, and a time varying resistance, $R(t)$:

$$\frac{d(LI)}{dt} + RI = V(t) \quad (1)$$

The inductance and the resistance are sums of time-independent line impedances and time-dependent load impedances: $L(t) = L_{line} + L_{load}(t)$ and $R(t) = R_{line} + R_{load}(t)$.

The energy equation for this simple circuit equation is found by multiplying Eq. (1) through by I :

$$\begin{aligned} VI &= \frac{d}{dt} (U_B^{line} + U_B^{diode}) + \left(R_{line} + R_{load} + \frac{1}{2} \frac{dL_{load}}{dt} \right) I^2 \\ &\equiv \frac{d}{dt} (U_B^{line} + U_B^{diode}) + R_{line} I^2 + P^{load}. \end{aligned} \quad (2)$$

Here, $U_B^{line} \equiv (1/2)L_{line}I^2$ and $U_B^{diode} \equiv (1/2)L_{load}I^2$ are the magnetic field energies stored in the transmission line and in the diode region between the pinch and return current circuitry respectively. This equation describes how once-stored generator energy is converted into the growth of line and diode magnetic field energy, Ohmic heating losses in the line, and a power flow into the Z-pinch load, as described by P^{load} :

$$P^{load} = \left(\frac{1}{2} \frac{dL_{load}}{dt} + R_{load} \right) I^2. \quad (3)$$

B. Diode

The transmission line terminates at the Z-pinch diode. In principle, therefore, the diode's impedance is difficult to compute accurately, and it must be determined empirically. However, if it is assumed that the diode has perfect cylindrical symmetry and perfectly conducting walls, that the region between the pinch and the return current is a vacuum, and that displacement currents within the diode can be neglected, then an approximate evaluation of the electromagnetic fields in the diode can be made [23]. These fields are needed to determine the flow of electromagnetic energy into the diode and into the pinch, and thus,

they relate to the load impedance. Under the above assumptions, Maxwell's equations can be solved subject to the boundary conditions that the current in the Z pinch, $I(t)$, and the voltage drop across the entry surface to the diode, $V_p(t) \equiv -\int_b^R dr E_r(r, z = \ell)$, are known functions of the time. The B-field, in this case, has only an azimuthal component, B_θ , which is determined by applying Stokes' theorem:

$$\mathbf{B} = B_\theta \hat{u}_\theta = \frac{2I(t)}{cr} \hat{u}_\theta, \quad \text{for} \quad b \leq r \leq R \quad \text{and} \quad 0 \leq z \leq \ell, \quad (4)$$

where the vacuum diode geometry is defined by: b , the outer boundary of the pinch, R , the radius of the diode region and of the return current path, and ℓ , both the length of the plasma and the diode region. Maxwell's equations then require that the E-field has a component along the z-direction of the pinch, \hat{u}_z , and one along the radial direction, \hat{u}_r : $\mathbf{E} = E_r \hat{u}_r + E_z \hat{u}_z$, where (from Ref. [23])

$$E_r = -\frac{V_p}{\ell \ln(R/b(t))} \frac{z}{r} < 0, \quad E_z = \left(\frac{V_p}{\ell \ln(R/b(t))} - \frac{2\dot{I}}{c^2} \right) \ln(R/r) > 0, \quad (5)$$

and $\dot{I} \equiv \partial_t I$. Since the walls of the return current path have infinite conductivity, the voltage drop across the entrance to the diode region also appears as a voltage drop across the load. The full voltage drop, $\int dz E_z(r = b, z)$ across the load, however, includes a back EMF and is given by

$$\int_0^\ell dz E_z(r = b, z) = V_p - \frac{2\ell}{c^2} \ln(R/b) \dot{I} = V_p - L_{load} \dot{I}, \quad (6)$$

where

$$L_{load} = \frac{2\ell}{c^2} \ln\left(\frac{R}{b(t)}\right). \quad (7)$$

The neglect of the displacement current is based on the assumption that the electric field energy density, $u_E^{diode} \equiv E^2/(8\pi)$, is negligible relative to $u_B^{diode} \equiv B_\theta^2/(8\pi)$ in the diode. In this case, energy conservation is expressed locally by $\partial_t u_B^{diode} + \nabla \cdot \mathbf{S} = 0$, where \mathbf{S} is the Poynting vector, $\mathbf{S} = (c/(4\pi)) \mathbf{E} \times \mathbf{B}$, and an integration of this equation over the volume of the diode region then yields a global equation for energy conservation of the form,

$$P^{diode} = \partial_t U_B^{diode} + P^{load} + P^{wall}, \quad (8)$$

where P^{diode} is the energy flux into the diode across its entry surface at $z = \ell$:

$$\begin{aligned} P^{diode} &= - \int_{surface} dA \mathbf{S} \cdot \hat{\mathbf{u}}_z \\ &= - \int_b^R 2\pi r dr \frac{c}{4\pi} (E_r(r, z = \ell) B_\theta(r)) = V_p I, \end{aligned} \quad (9)$$

and

$$U_B^{diode}(t) \equiv 2\pi \int_0^\ell dz \int_{b(t)}^R dr r u_B^{diode} = \frac{1}{2} L_{load}(t) I^2, \quad (10)$$

Power losses into the return current walls, P^{wall} , are found by integrating the Poynting flux over the walls of the return current can. They are zero in this analysis (because perfectly conducting walls were assumed in it) but not necessarily in experiments. Power flow into the Z pinch, P^{load} , has two parts, one coming from an integration of the Poynting flux across the surface of the pinch, P^L , and the other, from the magnetic field energy density, or pressure, acting on the moving boundary of the pinch:

$$P^{load} = 2\pi b \dot{b} \ell \frac{(B_\theta(r=b))^2}{8\pi} + P^L = -\frac{1}{2} \frac{dL_{load}}{dt} I^2 + P^L, \quad (11)$$

where $\dot{b} \equiv \partial_t b$. P^{load} cannot be determined from this diode analysis alone. The fields of Eqs. (4) and (5) satisfy Eq. (8) tautologically. To determine P^{load} , one must turn to an analysis of the plasma fluid equations, which govern the main characteristics of an idealized Z-pinch dynamics, i.e., of the dynamics that begin after the wires have broken down and plasma has fully formed.

C. Z-pinch Fluid Theory

Z pinches have been described by one-, two-, or three-dimensional fluid dynamic models, which must, in each case, be coupled to a generator circuit equation self-consistently. Plasmas contain four kinds of fluid energy: kinetic, $u_{KE} \equiv (1/2)\rho v_f^2$, ion thermal, $u_{th}^i \equiv$

$(3/2)n_i k_B T_i$, electron thermal, $u_{th}^e \equiv (3/2)n_e k_B T_e$, and an internal energy of ionization and excitation, u_{ion} . The full set of fluid equations describe the various ways that these energies are either partitioned within the plasma or radiated away. Their coupling to a circuit equation is carried out so as to maintain power flow continuity and overall energy conservation. However, while fluid dynamic models are much more detailed than a 0-D model; they are nevertheless idealized and approximate as well, since, as noted, they do not treat the early-time dynamics by which solid wires explode, break down, and become plasmas or by which gases break down. In addition, computer solutions to fluid equations are resolution limited.

Equations that describe the build-up and decay of electron and ion energy densities are derivable directly by taking energy moments of the electron and ion kinetic equations [13]:

$$\begin{aligned} \partial_t u_{Tot}^e + \nabla \cdot (u_{Tot}^e \mathbf{v}_e + \mathbf{P}_e \cdot \mathbf{v}_e + \mathbf{q}_e) \\ = -n_e e \mathbf{E} \cdot \mathbf{v}_e + Q_e + \mathbf{R}_{ei} \cdot \mathbf{v}_e + Q_e^{inel} - p_{brems}, \end{aligned} \quad (12)$$

$$\begin{aligned} \partial_t u_{Tot}^i + \nabla \cdot (u_{Tot}^i \mathbf{v}_i + \mathbf{P}_i \cdot \mathbf{v}_i + \mathbf{q}_i) \\ = n_i Z e \mathbf{E} \cdot \mathbf{v}_i + Q_i + \mathbf{R}_{ie} \cdot \mathbf{v}_i, \end{aligned} \quad (13)$$

where $u_{Tot}^e \equiv \frac{1}{2} \rho_e v_e^2 + u_{th}^e$ is the sum of electron kinetic and thermal energies, \mathbf{v}_e is the electron fluid velocity, $\mathbf{P}_e \equiv p_e \mathbf{I}_2 + \Pi_e$ is the electron pressure tensor, \mathbf{q}_e is the electron heat flux vector, \mathbf{E} is the electric field, Q_e is the elastic-collision energy transfer rate between electrons and ions, \mathbf{R}_{ei} is the elastic-collision momentum transfer rate between electrons and ions, Q_e^{inel} is the inelastic-collision energy transfer rate between electrons and ions, and p_{brems} is the bremsstrahlung energy loss rate. The quantities, u_{Tot}^i , \mathbf{v}_i , $\mathbf{P}_i \equiv p_i \mathbf{I}_2 + \Pi_i$, \mathbf{q}_i , Q_i , and \mathbf{R}_{ie} are similarly defined for the ions. The term, Q_e^{inel} , describes the rate of increase in the ion excitation and ionization energy density, u_{ion} , which is given by

$$\partial_t u_{ion} + \nabla \cdot (u_{ion} \mathbf{v}_i) = Q_e^{inel} - p_\ell - p_{rr}. \quad (14)$$

Here, p_ℓ and p_{rr} are line and recombination radiation energy density loss rates, respectively.

The fluid equations of a plasma are defined in terms of locally defined center of mass

and relative (or drift) velocities, \mathbf{v}_f and \mathbf{v}_d respectively, in terms of which the electron and ion fluid velocities are given by

$$\mathbf{v}_e = \mathbf{v}_f + \frac{\rho_i}{\rho} \mathbf{v}_d \cong \mathbf{v}_f + \mathbf{v}_d, \quad \mathbf{v}_i = \mathbf{v}_f - \frac{\rho_e}{\rho} \mathbf{v}_d \cong \mathbf{v}_f. \quad (15)$$

where $\rho \equiv \rho_e + \rho_i \cong \rho_i$. An equation describing total energy conservation can then be derived in terms of \mathbf{v}_f and \mathbf{v}_d by adding Eqs. (12) and (13) together and using the condition, $Q_e + \mathbf{R}_{ei} \cdot \mathbf{v}_e = -Q_i - \mathbf{R}_{ie} \cdot \mathbf{v}_i$, for energy conservation in elastic collisions:

$$\begin{aligned} \partial_t u_{Tot} + \nabla \cdot (u_{Tot} \mathbf{v}_f + \mathbf{P} \cdot \mathbf{v}_f + \mathbf{q} + u_{Tot}^e \mathbf{v}_d + \mathbf{P}_e \cdot \mathbf{v}_d) \\ = \mathbf{j} \cdot \mathbf{E} - p_{rad}, \end{aligned} \quad (16)$$

where, $u_{Tot} \equiv u_{Tot}^e + u_{Tot}^i + u_{ion}$, $q \equiv q_e + q_i$, $\mathbf{j} \equiv -n_e e \mathbf{v}_d$ is the electric current density, and $p_{rad} = p_l + p_{rr} + p_{brems}$ is the total radiation loss rate.

The plasma couples to the electromagnetic field by way of the $\mathbf{j} \cdot \mathbf{E}$ term in Eq. (16), which also appears in the energy equation derived from Maxwell's equations. Since displacement currents are small in a plasma, the left hand side of this equation has the same form as the energy equation in the diode:

$$\partial_t u_B^{pl} + \nabla \cdot \mathbf{S}^{pl} = -\mathbf{j} \cdot \mathbf{E}, \quad (17)$$

where $u_B^{pl} \equiv B^2/(8\pi)$ is the magnetic field energy density stored within the plasma. Finally, the addition of Eq. (16) to Eq. (17) produces an equation expressing local total energy conservation:

$$\partial_t (u_{Tot} + u_B^{pl}) + \nabla \cdot (u_{Tot} \mathbf{v}_f + \mathbf{P} \cdot \mathbf{v}_f + \mathbf{q} + u_{th}^e \mathbf{v}_d + \mathbf{P}_e \cdot \mathbf{v}_d + \mathbf{S}^{pl}) = -p_{rad}. \quad (18)$$

The coupling of the plasma fluid to the generator is now accomplished by integrating Eq. (18) over the volume of the plasma. The resulting equation connects the build-up of energy within the plasma to the flow of energy into the plasma from the diode,

$$P^{load} = \frac{d}{dt} (U_{Tot}^{pl} + U_B^{pl}) + P_{rad}, \quad (19)$$

and thus to the flow of energy into the diode from the generator when combined with Eq. (8), where

$$U_{Tot}^{pl} = 2\pi \int_0^\ell dz \int_0^{b(t)} r dr u_{Tot} \quad (20)$$

and U_B^{pl} and P_{rad} are similarly defined integrations over u_B^{pl} and p_{rad} respectively.

When the surface of the integration volume is taken to lie just inside of the plasma boundary, the fluid variables are nonzero and, in particular, the electric field satisfies an Ohm's law, which, in a cylindrically symmetric plasma, is given by

$$E_z = -\frac{v_f}{c} B_\theta + \frac{1}{n_e e} \left\{ \alpha_\perp \frac{j_z}{n_e e} + \beta_\Lambda \partial_r (k_B T_e) \right\} \Big|_{r=b-\epsilon}. \quad (21)$$

Then, because

$$2\pi \int_0^\ell dz \int_0^{b(t)} dr r \left\{ \partial_t u_{Tot}^{pl} + \nabla \cdot (u_{Tot}^{pl} \mathbf{v}_f) \right\} = \frac{dU_{Tot}^{pl}}{dt}, \quad (22)$$

and because the current flows parallel to the surface of the integration volume, whose normal is in the radial direction, it follows from Eqs. (18) and (19) that

$$\begin{aligned} \frac{d}{dt} (U_{Tot}^{pl} + U_B^{pl}) + P_{rad} = \\ \lim_{\epsilon \rightarrow 0+} \left\{ -2\pi b \dot{b} \ell \frac{B_\theta^2}{8\pi} + 2\pi b \ell (q_r + (\mathbf{P} \cdot \mathbf{v}_f)_r - \frac{c}{4\pi} E_z B_\theta) \right\} \Big|_{r=b-\epsilon}. \end{aligned} \quad (23)$$

Taken together, therefore, Eqs. (3), (21), and (23) imply that

$$\begin{aligned} P^{load} = \left(\frac{1}{2} \frac{dL_{load}}{dt} + R_{load} \right) I^2 = \\ - \lim_{\epsilon \rightarrow 0+} \left\{ 2\pi b \dot{b} \ell \frac{B_\theta^2}{8\pi} + 2\pi b \ell (q_r + (\mathbf{P} \cdot \mathbf{v}_f)_r - \frac{c}{4\pi} E_z B_\theta) \right\} \Big|_{r=b-\epsilon}. \end{aligned} \quad (24)$$

Eq. (25) can be used to determine R_{load} and L_{load} provided that the plasma boundary is located where pressure forces make a negligible contribution to the equation. On physical grounds, q_r is strictly zero at the plasma outer surface; however, one cannot, in principle, set the surface pressure to zero unless one sets $n_e = 0$ and $n_i = 0$. However, the current density would then go to zero unless one allows v_d at the surface to become infinitely large. In

Ref. [12], it is this behavior that argues for the growth of micro-instabilities and anomalous resistivity near to and at the plasma surface. This behavior also illustrates one of the ambiguities associated with producing a physically meaningful definition of an outer Z-pinch boundary. However, on setting $(\mathbf{P} \cdot \mathbf{v}_f)_r \cong 0$, one finds first that

$$\frac{1}{2} \frac{dL_{load}}{dt} I^2 + R_{load} I^2 = - \lim_{\epsilon \rightarrow 0^+} \left\{ 2\pi b \ell \frac{B_\theta^2}{8\pi} - \frac{c}{4\pi} E_z B_\theta \right\} \Big|_{r=b-\epsilon}; \quad (25)$$

and then, on substituting Eqs. (4) and (21) into this equation, one infers that

$$\frac{dL_{load}}{dt} = - \frac{2\ell}{c^2 b} \frac{db}{dt} \quad (26)$$

and

$$R_{load} I^2 = 2\pi b \ell \left\{ \frac{I}{2\pi b} \frac{1}{n_e e} \left(\alpha_\perp \frac{j_z}{n_e e} + \beta_\Lambda \partial_r (k_B T_e) \right) \right\} \Big|_{r=b} \quad (27)$$

Eq. (26) for L_{load} is consistent with Eq. (7), while Eq. (27) can be used to express R_{load} in a more physically meaningful form through the definition, first of all, of two areas, A_j and A_{th} , and a thermal velocity, v_{th} :

$$A_j \equiv \frac{I}{j_z(r=b)}, \quad A_{th} \equiv \frac{I}{j_{th}(r=b)}, \quad v_{th} \equiv \sqrt{2k_B T_e / m}, \quad (28)$$

and then, of a thermal current density,

$$j_{th} \equiv n_e e v_{th} \equiv n_e e \sqrt{2k_B T_e / m}, \quad (29)$$

dimensionless transport coefficients, $\hat{\alpha}_\perp$ and $\hat{\beta}_\Lambda$, by Ref. [13]

$$\alpha_\perp = \frac{m n_e}{\tau_e} \hat{\alpha}_\perp, \quad \beta_\Lambda = n_e \hat{\beta}_\Lambda, \quad \kappa_\perp = \frac{n_e k_B^2 T_e}{m} \tau_e \hat{\kappa}_\perp, \quad (30)$$

and a dimensionless temperature gradient,

$$x_{tr} \equiv \frac{v_{th} \tau_e}{T_e} \partial_r T_e \Big|_{r=b}. \quad (31)$$

One then finds that

$$R_{load} = \left\{ \frac{\ell \hat{\alpha}_\perp \eta_0}{A_j} + \frac{1}{2} x_{tr} \hat{\beta}_\Lambda \frac{\ell \eta_0}{A_{th}} \right\} \Big|_{r=b} \quad (32)$$

where the resistivity, η_0 , is defined by

$$\eta_0 \equiv m/(n_e e^2 \tau_e). \quad (33)$$

The above expression for R_{load} has the added benefit that it guarantees the continuity of E_z across the pinch boundary. Thus, one finds, on combining Eqs. (4), (5), (7), and (21), that

$$\begin{aligned} E_z(r = b + \epsilon) &= \frac{1}{\ell} (V_p - L_{load} \dot{I}) \\ &= -\frac{\dot{b}}{c} \left(\frac{2I}{cb} \right) + \frac{1}{n_e e} \left(\alpha_{\perp} \frac{j_z}{n_e e} + \beta_{\Lambda} \partial_r (k_B T_e) \right) \Big|_{r=b-\epsilon} = E_z(r = b - \epsilon). \end{aligned} \quad (34)$$

Using Eq. (26), this equation can be rewritten as

$$V_p = \frac{d}{dt} (L_{load} I) + \frac{1}{n_e e} \left(\alpha_{\perp} \frac{j_z}{n_e e} - \beta_{\Lambda} \partial_r (k_B T_e) \right) \Big|_{r=b}. \quad (35)$$

However, by definition of V_p , the circuit equation [Eq. (1)] can also be rewritten as

$$V(t) = L_{line} \frac{dI}{dt} + R_{line} I + V_p, \quad (36)$$

which identifies V_p as

$$V_p = \frac{d}{dt} (L_{load} I) + R_{load} I. \quad (37)$$

The comparison of Eq. (35) with Eq. (37) provides an expression for R_{load} that is identical to Eq. (33).

Finally, a third expression for R_{load} can be derived, which provides an important check on the accuracy of Z-pinch fluid dynamics calculations when it is compared to the calculation of R_{load} from Eq. (33). To obtain this expression, one integrates Eq. (17) over the volume of the Z-pinch plasma to find [using Eq. (11)] that

$$\frac{dU_B^{pl}}{dt} - P^{load} = -2\pi\ell \int_0^{b(t)} r dr j_z E_z. \quad (38)$$

One can then substitute Eq. (3) into Eq. (36) and solve for R_{load} :

$$R_{load} = \frac{1}{I^2} \left\{ \frac{dU_B^{pl}}{dt} + 2\pi\ell \int_0^{b(t)} r dr j_z E_z \right\} - \frac{1}{2} \frac{dL_{load}}{dt}. \quad (39)$$

In this equation, the volume integral over $j_z E_z = \mathbf{j} \cdot \mathbf{E}$ includes both $\mathbf{v}_f \cdot \mathbf{j} \times \mathbf{B}$ work and Ohmic heating by virtue of Ohm's law [Eq. (21)].

IV. MHD MODELING

The number of approximations built into the above analysis indicates the phenomenological nature of Z-pinch modeling (even when computers are used to solve sets of nonlinearly coupled, energy conserving circuit and fluid equations). It is not entirely surprising, therefore, when such calculations contain insufficient resistive coupling to reproduce the energy coupling inferable from the Saturn experiments. Based on the above analysis, this coupling deficiency can be overcome in 1-D modeling through the introduction of an additional (anomalous) surface resistivity:

$$\hat{\alpha}_{\perp}\eta_0\Big|_{r=b} \rightarrow \hat{\alpha}_{\perp}\eta_0\Big|_{r=b} + \eta_{Anomalous}\Big|_{r=b}. \quad (40)$$

The magnitude and temporal characteristics of $\eta_{Anomalous}$ within the plasma, however, are not determined by coupling considerations; they must be inferred indirectly, if possible, from the influence that $\eta_{Anomalous}$ has on the stagnation dynamics of a Z pinch and from the ability of this dynamics to replicate the x-ray output trends seen in experimental data. In this section, some results are presented from a phenomenological study of the Saturn data in Figs. 1-3 within the context of 1-D MHD calculations.

This study addressed such issues as: how much energy actually couples to a pinch when additions to the circuit resistance are made, how large an increase in circuit resistance is needed in order to double the amount of coupled energy, when and how rapidly can this resistance be applied during the course of the implosion, how sensitive is the calculation to variations in the enhanced resistivity, and, finally, what rate of energy transport is required within a plasma for enhanced energy inputs to show up as enhanced x-ray outputs? These questions were investigated within the context of a 1-D radiative hydrodynamics calculation by (1) specifying a functional form for the anomalous circuit resistance, (2) varying the parameters of the functional form, and (3) comparing the calculated x-ray emission to the experimental x-ray pulses shown in Fig. 1.

One learns by this procedure that the circuit resistance cannot be sizably increased until the pinch nears assembly since otherwise observable amounts of soft x rays are emitted

earlier than when they are seen experimentally. This finding is consistent with the impedance measurement reported in Ref. [14]. One also finds limits on the rate at which energy can be coupled effectively to the plasma because of the large impact that this rate has on the hydrodynamics. These limits are set by both the rate at which energy is transported into the plasma and on the rate at which it is radiated from the plasma. Only when these two rates are sufficiently large does the calculated x-ray output move in the direction of the data shown in Figs. 1-3.

The calculations described in this section were computer intensive; the aluminum model contained 136 energy levels, 22 K-shell states, 77 L-shell states, 125 K-shell lines, and 202 L-shell lines, and the calculations employed a tabular lookup, escape probability method to carry out both the kilovolt and subkilovolt photon transport [24]. Nevertheless, 77 states do not provide an accurate description of the multiplet structure of the L-shell ionization stages; thus, L-shell emissions are not as accurately transported within the plasma as they should be. The transport of soft x rays is more diffusive than that of kilovolt x rays, and thus escape probability methods are more appropriate for the kilovolt emissions than subkilovolt. For this reason, we introduced two parameters into our calculations in order to be able to phenomenologically increase and vary the rates of soft x-ray energy transport and partially compensate for the missing atomic structure. A multiplier, α , on the electron heat flux was introduced as a way of approximately simulating the influence of soft x-ray diffusive transport on the pinch dynamics, and a multiplier, β , was included in the calculation of L-shell emissivities to compensate for missing distributions of L-shell oscillator strength.

In all, four modifications to the MHD were made in this investigation of enhanced energy coupling. The load impedance, the rate of diffusive energy transport, and the rate of soft x-ray emission were all increased as described above. In addition, the value of the anomalous resistivity was specified throughout the plasma. For lack of specific theoretical guidance, we assumed a fixed, gradual, linear reduction by roughly two orders of magnitude from its surface value in the value of $\eta_{Anomalous}$ throughout the plasma interior. By this assumption, resistivity levels remained anomalously high throughout the plasma, which produced

increases in the rate of magnetic field and current diffusion and, therefore, in the amount of Ohmic heating interior to the plasma. The impact that this resistivity assumption had on x-ray conversion efficiencies was, therefore, positive, since it aided the energy transport into the plasma, i.e., steepening of the resistivity gradient at the surface of the pinch serves to reduce the degree of current diffusion and Ohmic heating within the plasma. Energy must then be transported by secondary means into the plasma interior (by pressure forces, electron heat conduction, or soft x-ray transport) in order to be radiated efficiently. The impact that varying the resistivity profile has on the calculations was not addressed in this work. The resistivity was reduced from zone to zone as described above, and this contouring was then kept the same in all of our calculations.

By applying the above phenomenology, we were able to replicate several important features of the Figs. 1-3 Saturn data. For example, when the resistance time history shown in Fig. 4 was employed in a 100 zone 1-D calculation, it produced the total x-ray output pulse shown in Fig. 5. This pulse approximates both the early- and late-time features of the x-ray pulses shown in Fig. 1. The heat flux multiplier, α , had a value of 600 and β , a value of 3 in this calculation. The sensitivity of the calculation to and the validity of the α value used are discussed later in this section. The resistance in Fig. 4 is composed of two parts. One (labeled Braginskii in the figure) was calculated from the surface value of the classical resistivity, $\hat{\alpha}_1 \eta_0$, using Eq. (32), while the other was a prescribed input to the calculation. The prescribed resistance was taken to rise exponentially with a risetime of 5 ns, to peak at 172 ns at a value of 0.658Ω , and to fall exponentially with a faltime of 30 ns. The surface value of $\eta_{Anomalous}$ that was used in the fluid equations was calculated from the prescribed resistance using Eqs. (32) and (40).

Because the circuit resistance had an extended decay, a substantial amount of energy coupled to the plasma following the main x-ray pulse, and this late-time coupling produced the foot (or tail) to the main pulse seen in Fig. 5. The emission spike at the end of the tail was produced by a secondary, late-time implosion, an event often seen in 1-D calculations. In this instance, the presence of this spike correlates with the more subdued late-time spiking

seen in the x-ray pulses of the (3-D) shots 2693 and 2706 (and noted in Fig. 1). In this 100 zone, fiducial calculation, 671 kJ coupled to the pinch in 245 ns; 369 kJ of this coupled energy was emitted in the main x-ray pulse, and 292 kJ, in the tail. Overall, therefore, 661 kJ of the 671 kJ input was radiated. It was divided into 143 kJ of kilovolt and 518 kJ of subkilovolt emissions. Thus, in the 245 ns time interval over which the calculation extended, substantially all of the energy that coupled to the pinch was radiated, and it had to be in order to be comparable to the total x-ray output measured in shots 2636 and 2706 (Fig. 3). For the calculation to produce this result, however, a nearly three order of magnitude increase in the circuit resistance was needed, in agreement with the resistance increases predicted by the 0-D calculations described in Ref. [25]. Finally, we note that, while a comparable amount of energy coupled to the pinch in this calculation as in the experiments, there was much less K-shell emission (by a factor ~ 2.5) in the experiments than in the calculation. Moreover, the calculated K-shell pulse had less late-time structure than was seen experimentally in shots 2693 and 2706 (Fig. 2).

Fig. 4 contains two plots of $R_{load}(t)$. The one labeled surface calculation was obtained from Eqs. (32) and (40) with $\eta_{Anomalous}$ derived from the prescribed part of R_{load} . The dotted curve, labeled volume calculation, was calculated from Eq. (39). When these two calculations are in close agreement at a given time, they indicate that an accurate spatial integration of the magnetic field diffusion equation has been carried out at that time. This accuracy depends on the zoning in the calculation, and deviations between the curves temporarily occurred in the calculation late-time because irregular spacings between zones had been generated by the Lagrangian fluid dynamics. Thus, the quality of the agreement between the surface and volume calculated values of R_{load} (which was generally excellent for all of the calculations described in this section) can be degraded when the number of zones used in the calculation is too small or when their spacing becomes too irregular.

The above, fiducial, calculation was constructed so that the MHD dynamics would couple, transport, and radiate energy at comparable rates, and retard expansion of the plasma following stagnation. Under these conditions, the plasma continues to radiate while the

coupling remains strong, producing a tail on the x-ray pulse as seen in Fig. 5. On the other hand, when the enhanced resistance is taken to fall as fast as it rises (by replacing the resistance of Fig. 4 by a comparably fast rising and falling Gaussian pulse, for example), only a single x-ray pulse is generated, similar to the one observed in shot 2636 (Fig. 1). X-ray emission cuts-off once the energy coupling enhancements are terminated. In this case, the inductive coupling between pinch and diode is reversed as the pinch maintains an outward expansion.

The x-ray emission generated in this fiducial calculation depended critically on four parameters: the magnitude of the heat flux multiplier, the magnitude of the L-shell emissivity multiplier, the maximum value of R_{load} , and the time relative to plasma assembly at which R_{load} achieves its maximum value. Consequently, we determined the sensitivity of the calculation to each of these parameters by varying each parameter in turn about the value it had in the fiducial calculation. The effects of these single parameter variations on energy coupling and x-ray output are presented in Figs. 6-15.

In order to determine the dependence of x-ray production on the strength of diffusive energy transport, a physically based range over which α can be varied needed to be determined. This was done by comparing the heat flux, $q_{rad} = -\kappa_R \partial_r T_e$, due to blackbody radiation to the electron heat flux, $q_e = -\kappa_e \partial_r T_e$, where $\kappa_e = \hat{\kappa}_e (n_e k_B^2 T_e \tau_e) / m_e$ and $\kappa_R = 16\sigma T_e^3 / (3\rho K_R)$. Here, $\hat{\kappa}_e$ is a dimensionless transport coefficient [13], ρ is the plasma density, σ is the Stefan-Boltzmann constant, and K_R is the Rosseland mean opacity per unit mass density. The Rosseland mean for aluminum was recently calculated [26]. It has values ranging between 10^3 and 10^4 cm²/g at the plasma densities and temperatures that were present in our calculations prior to Z-pinch assembly. When employed in our calculations, these temperature and density values predicted blackbody heat fluxes that were more than four orders of magnitude larger than the electron heat flux. Consequently, we varied α up to values of 2000.

In all the calculations in which α was varied, the energy that coupled to the pinch in 200 ns was only slightly affected, ranging narrowly between 500 and 550 kJ. The ability of the plasma to radiate this energy, however, depended sensitively on its ability to conduct the

coupled energy into its interior. The three energy curves shown in Figs. 6 and 7 demonstrate this point. The curve labeled 180 ns in Fig. 6 shows the total x-ray energy radiated in the main pulse, which terminated at 180 ns in these calculations. The other curves in Figs. 6 and 7 show how the total and K-shell x-ray outputs varied, respectively, over a 200 ns period. At first, the total emission rises as more energy is conducted into the plasma, but then it falls because sufficient energy has been conducted inwards to ionize the plasma into He-like ground states. At this point, L-shell emissions turn down while K-shell emissions continue to rise. Once these K-shell emissions slow their rise, saturate, and then fall for $\alpha \geq 600$, L-shell emissions can return to their peak values.

The influence of the L-shell emission rate on x-ray outputs is shown in Figs. 8 and 9. The energies plotted are emissions that were calculated over the first 200 ns of the pinch dynamics. Up to a β level of 2, both the K- and L-shell emissions increase with β because an increased cooling rate moderates the fluid dynamics during plasma assembly and inhibits the subsequent regeneration of kinetic energy. However, as β becomes larger than 2, K-shell emissions decrease rapidly because a growing amount of L-shell cooled plasma is unable to ionize into the K-shell. Throughout these variations in L-shell cooling rate, energy coupling to the plasma remained relatively unchanged.

Both the shape and the magnitude of the measured x-ray pulses place severe restrictions on the time history of the load resistance that is needed to replicate these pulses. When too much heating occurs too early in the implosion, the plasma emits x-rays prematurely and produces a pulse with an early-time foot, which was not seen in the experiments. Moreover, too much early-time heating causes the plasma to overheat during run-in, reducing its compressibility during assembly and, in turn, its x-ray conversion efficiency. Thus, if large and rapid increases in pinch resistance occurred in the experiments, these increases must have taken place near to the time of pinch assembly.

Given these considerations, two sets of calculations were carried out to determine the sensitivity of energy coupling and the accompanying x-ray production to the size and timing of circuit resistance increases. The results of these calculations are shown in Figs. 10-14. In

these calculations, the shape of the resistance pulse was kept the same as shown in Fig. 4, i.e., the rise and fall times were kept unchanged, while variations were made to its peak value and to the time at which it reached this value, while α and β were held at values of 600 and 3 respectively.

In one set of calculations, the maximum value of the load resistance, R_{load}^{max} , was varied while the rise and fall times and the time to peak resistance remained unchanged. The energy coupling and radiative outputs calculated during the first 200 ns of the pinch dynamics are shown in Figs. 10-12. The total energy coupled to the plasma, which is shown in Fig. 10, has been broken into an inductive and a resistive part. The inductive part is defined by

$$E_{ind}(t) \equiv \int_0^t dt' \left(\frac{1}{2} \frac{dL_{load}(t')}{dt'} I(t')^2 \right), \quad (41)$$

and the resistive part by

$$E_{res}(t) \equiv \int_0^t dt' R_{load}(t') I(t')^2. \quad (42)$$

Initially both of these couplings, and thus the total coupling, increase with R_{load}^{max} . However, once R_{load}^{max} becomes larger than 0.3Ω , the inductive coupling falls at roughly at the same rate as the resistive coupling rises, causing the total coupled energy to remain relatively flat. Beyond a peak of 0.6Ω , the rise and fall rates of E_{res} and E_{ind} respectively, increase, and this change correlates with the decline in calculated x-ray emissions, both total and K-shell that are shown in Figs. 11 and 12. This behavior indicates that, when the amount of resistive heating is too large, the plasma cannot radiate coupled energy fast enough to prevent its conversion into kinetic energy.

Finally, the sensitivity of coupled and radiated energy to the time at which the load resistance reaches its maximum value is illustrated in Figs. 13 and 14. In these calculations, R_{load}^{max} was held at a value of 0.653Ω , and the time to peak resistance, $t_0 + \Delta t$, was varied around its Fig. 4 value in which $t_0 = 172ns$. The total and resistive energies that were coupled in these calculations over 200 ns are plotted in Fig. 13 as a function of Δt . Fig. 14 contains similar plots of the calculated total and K-shell radiated energies. As noted above,

these figures demonstrate that too much heating too soon in the implosion reduces the plasma compressibility and the radiative cooling at assembly. Extra energy inputs convert instead into kinetic energy. Hence, the radiative output rises rapidly as $\Delta t \rightarrow 0$, and K-shell emission is maximized at $\Delta t = 0$. When $\Delta t = 2$ ns, the circuit resistance peaks at the time of peak emission, causing the K-shell emission to fall to half of its maximum value. We note finally that the extreme sensitivity, which is seen in all of the above calculations, to small changes in the size, shape, and timing of the enhanced circuit resistance is consistent with the large shot-to-shot variations seen experimentally (Fig. 1) in the x-ray data.

V. PLASMA COLLISIONALITY

In Ref. [12], a resistivity formula based on the growth and saturation of lower-hybrid drift wave micro-instabilities at the surface of a pinch was proposed and its effects on the equilibrium states and the radiative collapse of Z-pinches was investigated. This formula was written in the form of a classical resistivity with an enhanced collision frequency, ν^* , produced by an electron drift-wave interaction:

$$\eta^* = \frac{m\nu^*}{n_e e^2}, \quad \nu^* = \left(\frac{\pi}{8}\right)^{1/2} \left(\frac{v_d}{v_{th}^i}\right)^2 \sqrt{\omega_{ce}\omega_{ci}}, \quad (\text{sec}^{-1}) \quad (43)$$

where ω_{ce} and ω_{ci} are the electron and ion plasma frequencies respectively, $v_d = j_e/(n_e e)$ is the electron drift velocity, and $v_{th}^i = \sqrt{2k_B T_i/m_i}$ is the average ion thermal speed. This resistivity is temperature insensitive, and it increases as the surface density decreases in contrast to Spitzer resistivity, which is essentially density independent and which decreases with temperature increases. As electromagnetic energy flows into and couples to a pinch, its surface temperature rises and its surface density falls. As these changes take place, Spitzer resistivity decreases, while drift-wave resistivity increases.

Because a drift-wave resistivity has properties in common with the surface resistivity employed in the above calculations, it was of interest to compare the two to determine how closely they would match up in, for example, the above, fiducial calculation. This

comparison is made in Fig. 15, which shows the time evolution of four resistivities. The resistivity at the plasma outer boundary, labeled $\eta_{r=b}$ in Fig. 15, was calculated from R_{load} : $\eta_{r=b} = R_{load}I/(\ell j_z(r=b))$. The curve labeled $\eta_{r=r_0}$ shows the resistivity at the nominal inner boundary of the shell-like imploding plasma. It is shown to illustrate the resistivity contouring that was employed in the calculation. The classical resistivity, labeled η_{Brag} , was calculated at the plasma outer boundary using the formula, $\eta_{Brag} = \hat{\alpha}_\perp \eta_0|_{r=b}$ [13]. Finally, the resistivity, labeled η^* , was calculated at the outer boundary of the plasma using the drift-wave formula (Eq. (43)). As expected, it rose more than two orders of magnitude; however, its rise occurred late in time, well after the rise in $\eta_{r=b}$ that was needed to produce the x-ray output shown in Fig. 5.

VI. SUMMARY

Because both Maxwell's equations and the fluid equations describe local flows of energy, Z-pinch to pulsed-power generator coupling is determined by the continuity of the transmission line energy flow across the outer boundary of the pinch. Increases in Z-pinch resistance, therefore, are related to increases in the plasma's surface resistivity (and to its surface area). Resistivity increases can occur when surface conditions are set up during a pulsed-power discharge that stimulate the growth of plasma micro-instabilities (which increase the plasma's surface collisionality) as well as the growth of Rayleigh-Taylor or other implosion instabilities (which are calculated to increase a pinch's surface area). In this paper, the impact on the fluid dynamics of augmenting the surface collisionality was investigated in order to increase the energy coupling and to evaluate how well such augmentations are able to replicate the x-ray behavior seen in a set of identical Saturn experiments. A phenomenological approach to modeling this coupling was adopted for lack of a first-principles theory that accurately describes how micro-instability growth, for example, affects a Z-pinch's surface resistivity.

Four things were learned from this 1-D analysis of the Saturn experiments. One, three orders of magnitude increases in resistance were needed to produce comparable amounts of

energy coupling as were seen experimentally. Two, the rate at which energy is transported within the plasma and the rate at which it is radiated had to be comparable to the energy coupling rate for the added energy inputs to end up as added x-ray outputs. Three, for the calculations to approximately replicate the time history of a given measured x-ray pulse, only a highly restricted range of resistance enhancements could be employed in these calculations. In particular, the presence or absence of a late-time tail depended on the decay rate of the enhanced resistance. And four, the extreme sensitivity of the calculations to variations in (1) the rates of energy transport and loss, (2) the peak value of the enhanced resistance, and (3) the onset time of the rapid resistance enhancements were consistent with the large shot-to-shot variations seen in the Saturn experiments.

Our calculations showed that significant changes in the fluid dynamics occur when the resistive coupling to a Z-pinch becomes competitive with the inductive coupling. As the resistive coupling is increased, Ohmic heating in the outer regions of the plasma is increased. If this heat energy is not transported into the inner regions of the plasma fast enough, the energized surface simply blows away in a 1-D calculation. The analysis of the Saturn aluminum-wire shots presented in this paper has suggested that L-shell emissions have a significant influence on energy transport within the plasma. It is already known experimentally that they have increasing effect on K-shell emissions as the atomic number of the Z-pinch is increased [31]. However, as a caveat, kinetic energy generation is different in one dimensional fluid dynamics than in two- or three-dimensions. Recent work on the early time dynamics of wire arrays has shown that plasma does not blow away when there are gaps between the wires. It flows into the gaps instead. If similar two dimensional behavior persists late-time, it may play a role in the energy coupling problem. In this case, a gap dependent coupling should be determinable experimentally.

Other issues need to be addressed before a more definitive understanding of the Saturn experiments can be worked out. More needs to be learned about the strength of surface micro-instabilities and about their influence on current flow. If enhanced energy coupling is related to the multi-dimensional character of Z-pinch implosions, it should be detectable

in both wire array and gas puff experiments. On the other hand, if it is more prominent in wire array than in gas puff experiments, it may be related more specifically to the way wires break down in time, generating a different implosion dynamics than is predicted by 0-D Z-pinch calculations [32]. In all cases, however, the different fluid dynamic mechanisms that move energy about the plasma and that aid in converting enhanced energy couplings into x rays need to be investigated and more quantitatively understood.

ACKNOWLEDGMENTS

This work was accomplished by a strong collaboration with Ken Whitney, who provided most of the leadership for this investigation.

-
- [1] C. Deeney, C. A. Coverdale, M. R. Douglas, K. W. Struve, R. B. Spielman, W. A. Stygar, D. L. Peterson, N. F. Roderick, M. G. Haines, F. N. Beg, and J. Ruiz-Camacho, *Phys. Plasmas*, **6**, 3576 (1999).
- [2] J. P. Apruzese, J. W. Thornhill, K. G. Whitney, J. Davis, C. Deeney, and C. A. Coverdale, *Phys. Plasmas*, **8**, 3799, (2001).
- [3] C. A. Coverdale, C. Deeney, M. R. Douglas, J. P. Apruzese, K. G. Whitney, J. W. Thornhill, and J. Davis, *Phys. Rev. Lett.*, **88**, 065001-1, (2002).
- [4] J. C. Riordan, J. S. Pearlman, M. Gersten, and J. E. Rauch, in "Sub-Kilovolt X-ray Emission from Imploding Wire Plasmas", AIP Conf. Proc. No. 75, edited by D. Attwood and B. Henke (AIP, New York, 1981), p. 35.
- [5] M. Krishnan, C. Deeney, T. Nash, P. D. LePell, and K. Childers, in "Dense Z-Pinches, Second International Conference", AIP Conf. Proc. No. 195, edited by N. R. Pereira, J. Davis, and N. Rostoker, (AIP, New York, 1989), p. 17.
- [6] L. I. Rudakov, A. L. Velikovich, J. Davis, J. W. Thornhill, J. L. Giuliani, Jr., and C. Deeney, *Phys. Rev. Lett.*, **84**, 3326 (2000).
- [7] A. L. Velikovich, J. Davis, J. W. Thornhill, J. L. Giuliani Jr., L. I. Rudakov, and C. Deeney, *Phys. Plasmas*, **7**, 3265 (2000).
- [8] J. L. Giuliani, Jr., J. E. Rogerson, C. Deeney, T. Nash, R. R. Prasad, and M. Krishnan, *J. Quant. Spectrosc. Radiat. Transfer*, **44**, 471 (1990).
- [9] D. L. Peterson, R. L. Bowers, K. D. McLenithan, C. Deeney, G. A. Chandler, R. B. Spielman, M. K. Matzen, and N. F. Roderick, *Phys. Plasmas*, **5**, 3302 (1998).
- [10] D. L. Peterson, private communication.

- [11] C. Deeney, T. Nash, R. R. Prasad, L. Warren, K. G. Whitney, J. W. Thornhill, and M. C. Coulter, *Phys. Rev. A*, **44**, 6762 (1991).
- [12] A. E. Robson, *Phys. Fluids B*, **3**, 1461 (1991).
- [13] S. I. Braginskii, "Reviews of Plasma Physics", edited by M. A. Leontovich, Consultants Bureau, New York, p. 205 (1965).
- [14] A. Y. Labetsky, R. B. Baksht, V. I. Oreshkin, A. G. Roussikh, and A. V. Shishlov, *IEE Trans. Plasma Sci.*, **30**, 524 (2002).
- [15] J. Katzenstein, *J. Appl. Phys.* **52**, 676 (1981).
- [16] A. B. Bud'ko and M. A. Liberman, *Zhurnal Prikladnoi Mekhaniki i Tekhnicheskoi Fiziki* **30**, 3 (1989).
- [17] A. L. Velikovich, I. V. Sokolov, and A. A. Esaulov, *Phys. Plasmas*, **9**, 1366 (2002).
- [18] A. E. Robson, *Phys. Rev. Lett.* **63**, 2816 (1989); A. E. Robson, *Phys. Fluids B* **1**, 1834 (1989).
- [19] W. H. Bennett, *Phys. Rev.* **45**, 890 (1934).
- [20] R. S. Pease, *Proc. Phys. Soc. London Ser. B* **70**, 11 (1957).
- [21] S. I. Braginskii, *Sov. Phys. JETP* **6**, 494 (1958).
- [22] Carl-Gunne Falthammar, *Phys. Fluids* **4**, 1145 (1961).
- [23] W. M. Manheimer, *Phys. Fluids* **17**, 1767 (1974).
- [24] J. W. Thornhill, J. P. Apruzese, J. Davis, R. W. Clark, A. L. Velikovich, J. L. Giuliani, Jr., Y. K. Chong, K. G. Whitney, C. Deeney, C. A. Coverdale, and F. L. Cochran, *Phys. Plasmas* **8**, 3480 (2001).
- [25] K. G. Whitney, J. W. Thornhill, C. Deeney, C. A. Coverdale, J. P. Apruzese, J. Davis, A. L. Velikovich, and L. I. Rudakov, in "Dense Z-Pinches, Fifth International Conference", AIP Conf. Proc. No. 651, edited by J. Davis, C. Deeney, and N. R. Pereira, (AIP, New York, 2002),

p. 358.

- [26] J. Zeng and J. Yuan, Phys. Rev. E, **66**, 016401-1 (2002).
- [27] N. R. Pereira, N. Rostoker, and J. S. Pearlman, J. Appl. Phys., **55**, 704 (1984).
- [28] N. A. Bobrova and T. L. Razinkova, Sov. J. Plasma Phys. **13**, 53 (1987), trans. from Fiz. Plazmy **13**, 92 (1987).
- [29] M. Coppins, I. D. Culverwell, and M. G. Haines, Phys. Fluids **31**, 2688 (1988).
- [30] D. W. Scudder, Phys. Fluids **26**, 1330 (1983).
- [31] C. Deeney, C. A. Coverdale, M. R. Douglas, T. J. Nash, R. B. Spielman, K. W. Struve, K. G. Whitney, J. W. Thornhill, J. P. Apruzese, R. W. Clark, J. Davis, F. N. Beg, and J. Ruiz-Camacho, Phys. Plasmas, **6**, 2081 (1999).
- [32] S. V. Lebedev, F. N. Beg, S. N. Bland, J. P. Chittenden, A. E. Dangor, M. G. Haines, K. H. Kwek, S. A. Pikuz, and T. A. Shelkovenko, Phys. Plasmas, **8**, 3734 (2001); S. V. Lebedev, R. Aliaga-Rossel, S. N. Bland, J. P. Chittenden, A. E. Dangor, M. G. Haines, and I. H. Mitchell, Phys. Plasmas, **6**, 2016 (1999).

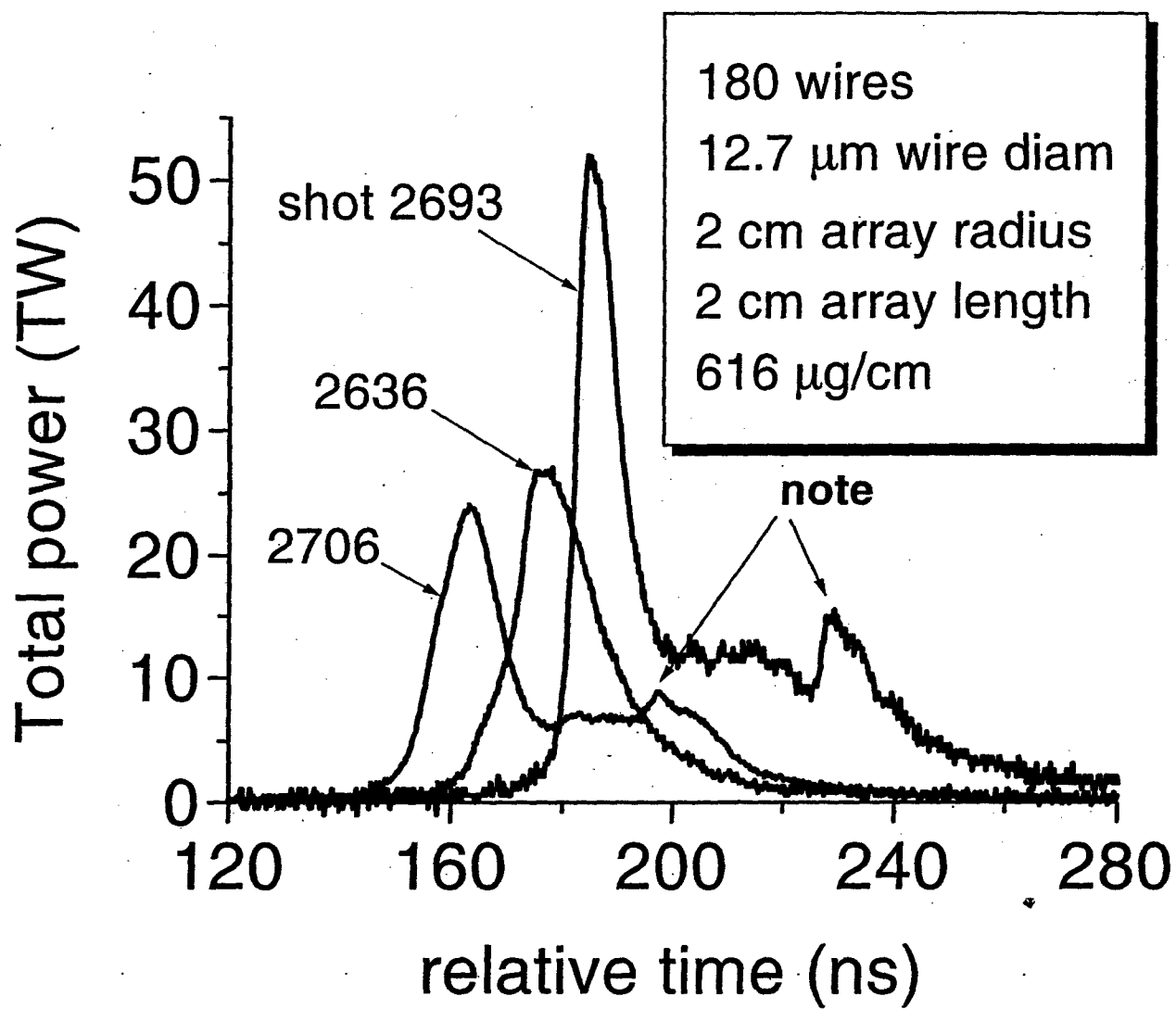


FIG. 1. Measured total x-ray output for three identical shots having the wire array parameters listed in the figure. The time axis has no fiducial.

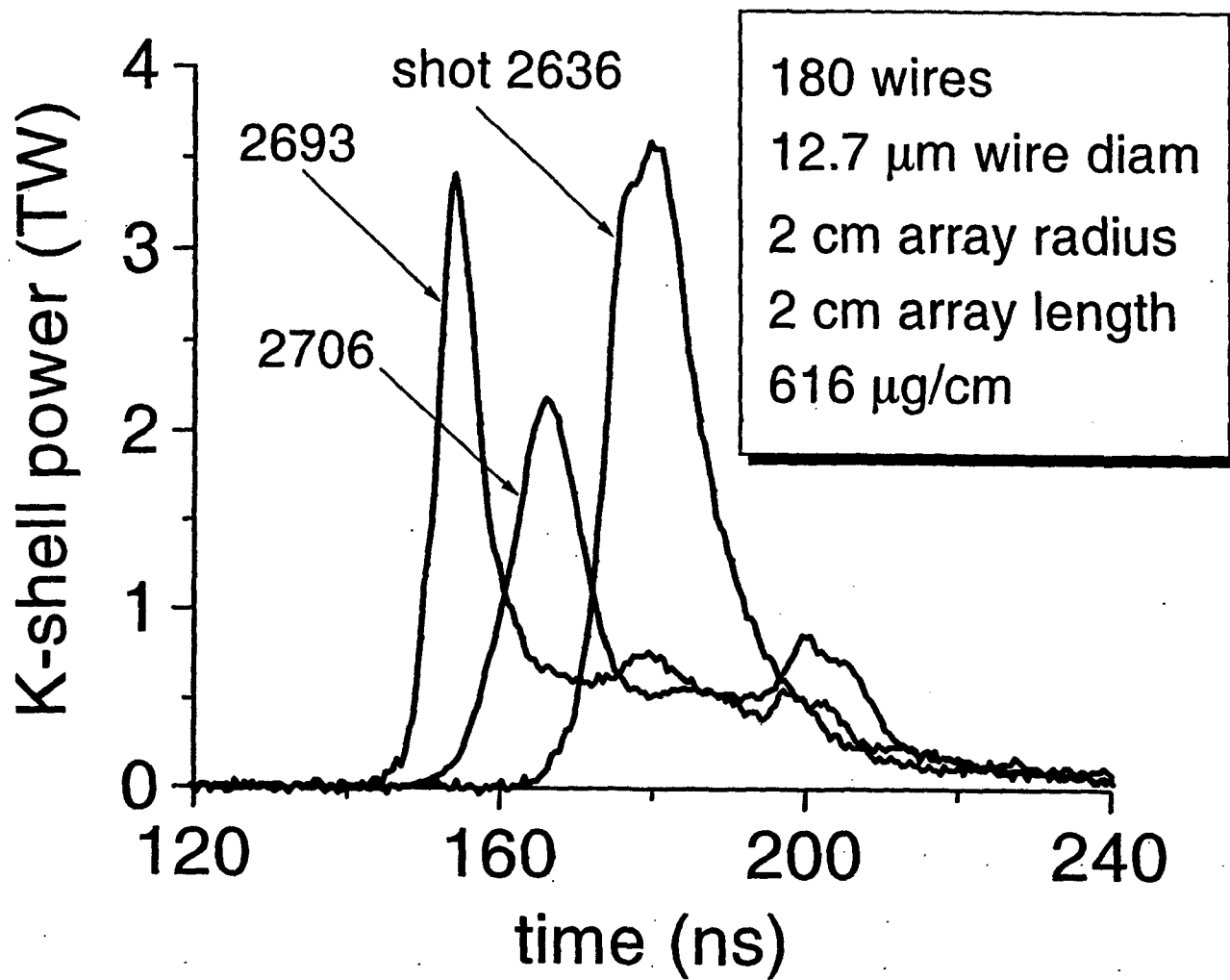


FIG. 2. Measured K-shell x-ray output for the same three identical shots as in Fig. 1 having the wire array parameters listed in the figure. The time axis has no fiducial.

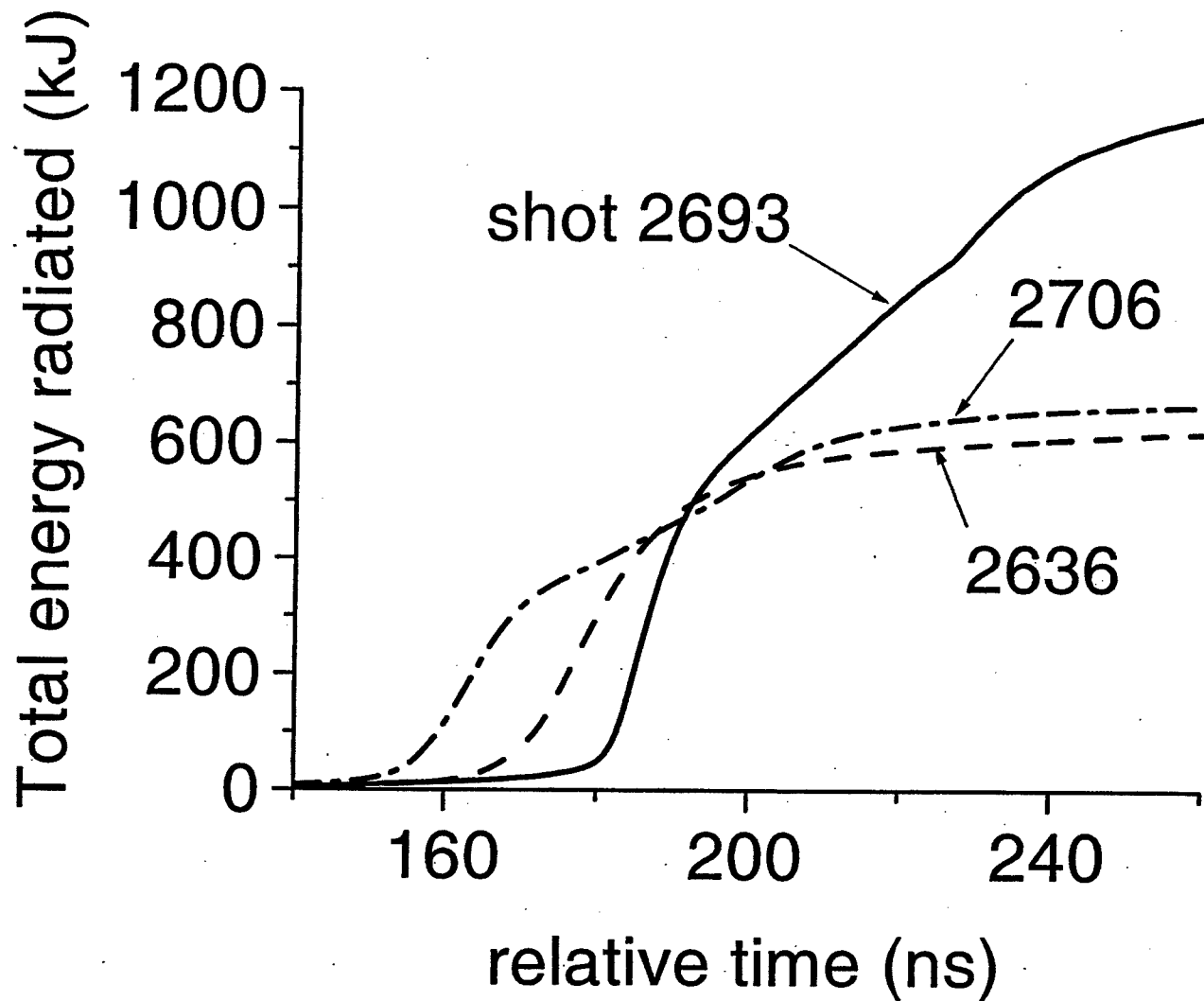


FIG. 3. The running time integrals for the three x-ray pulses shown in Fig. 1 are plotted as a function of the integration time.

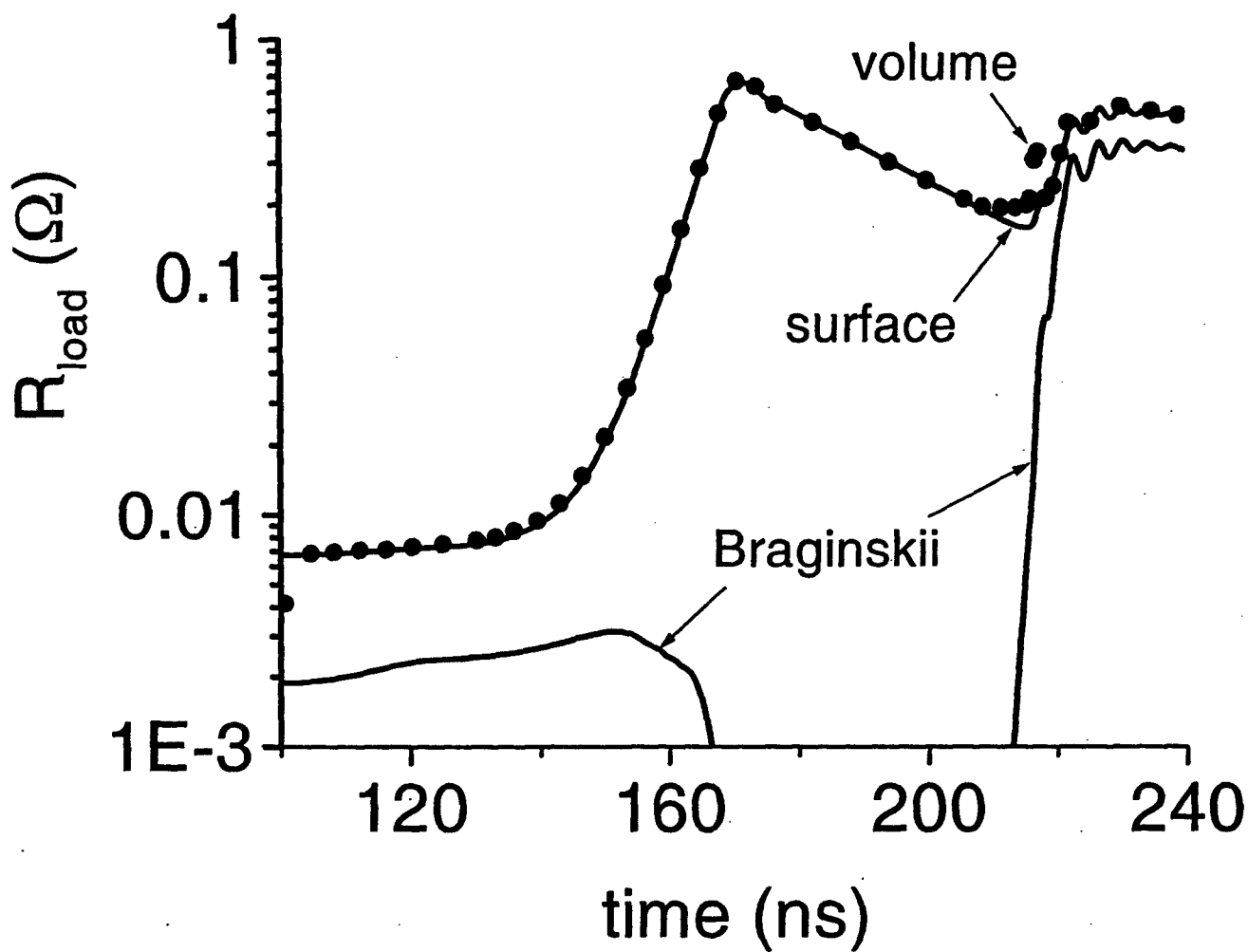


FIG. 4. A circuit resistance, which produces a comparable energy coupling as seen experimentally, is plotted as a function of time. It consists of a part derived from Eq. (32), using Braginskii's formula for electrical resistivity, and another part that is prescribed. The dotted points represent the circuit resistance that was calculated using Eq. (39).

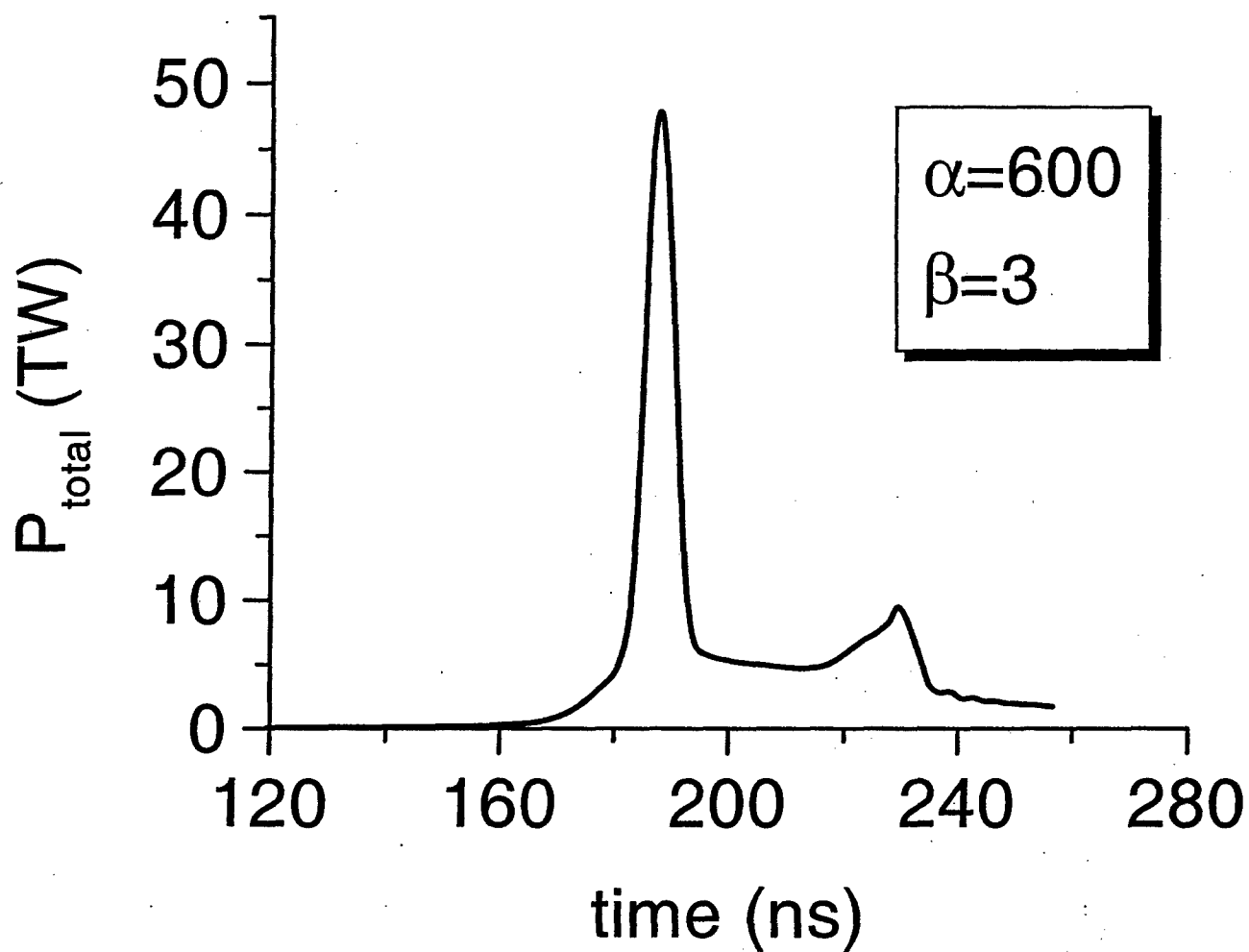


FIG. 5. Total x-ray pulse calculated using the circuit resistance shown in Fig. 4. The multipliers on heat conductivity and L-shell emissivity that were used in the calculation are listed in the figure.

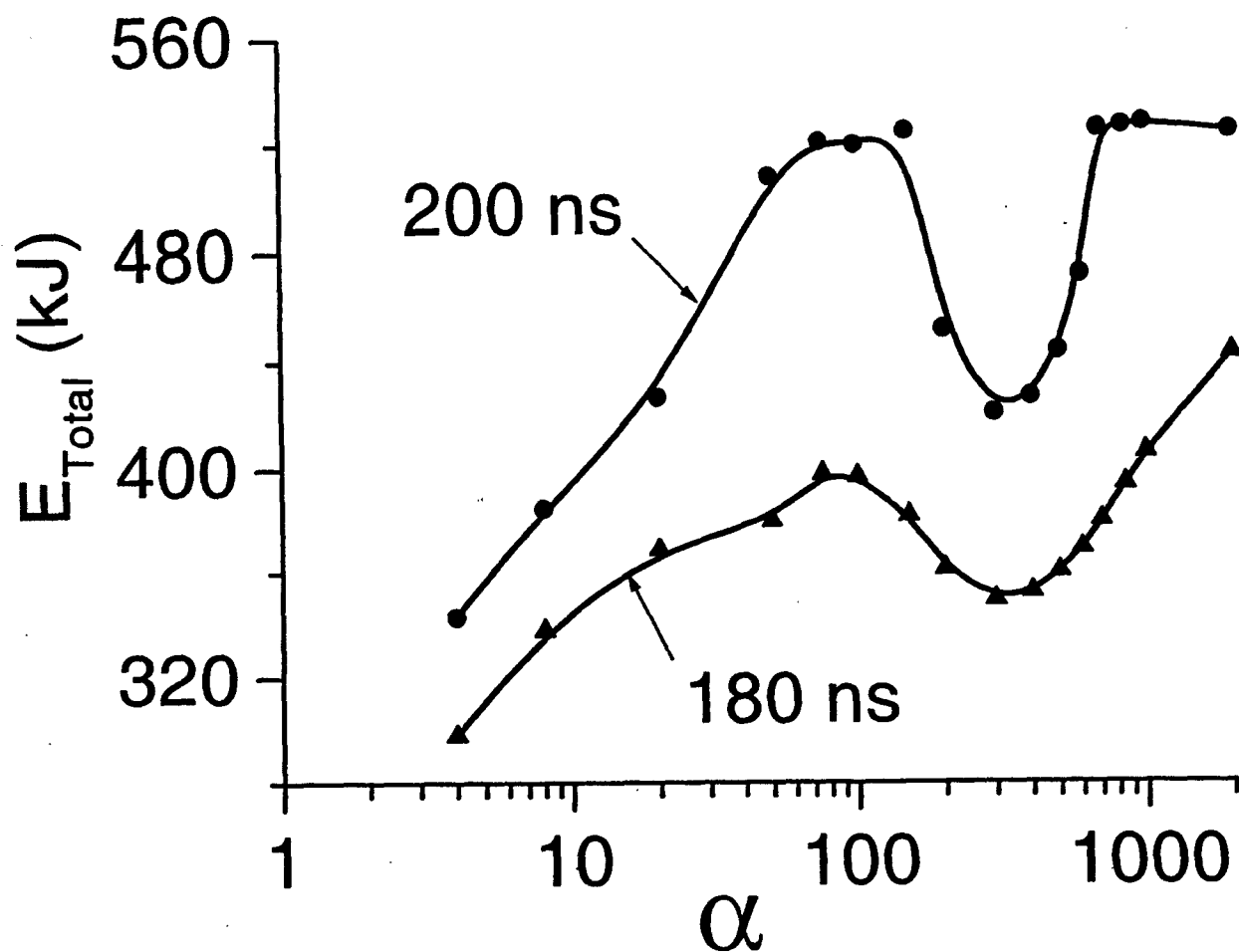


FIG. 6. The variation in the total energy radiated in 180 ns (in the main pulse) and in 200 ns as a function of the heat flux multiplier. The circuit resistance and β multiplier are the same as in Figs. 4 and 5. Spline fits are drawn to the calculated points.

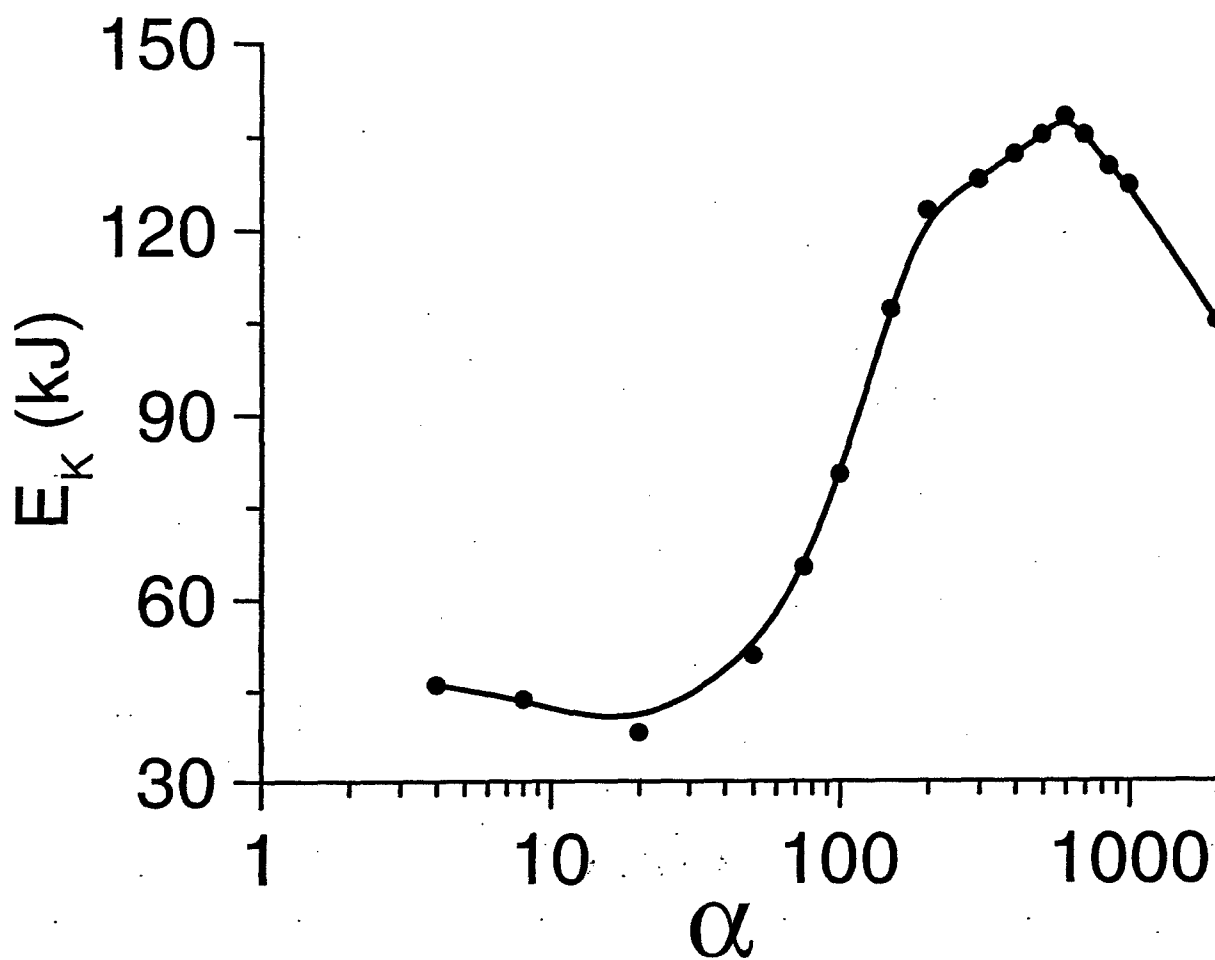


FIG. 7. The variation in the K-shell energy radiated in 200 ns as a function of the heat flux multiplier. The circuit resistance and β multiplier are the same as in Figs. 4 and 5. The calculated K-shell pulse had negligible amounts of emission following the main pulse. A spline fit is drawn to the calculated points.

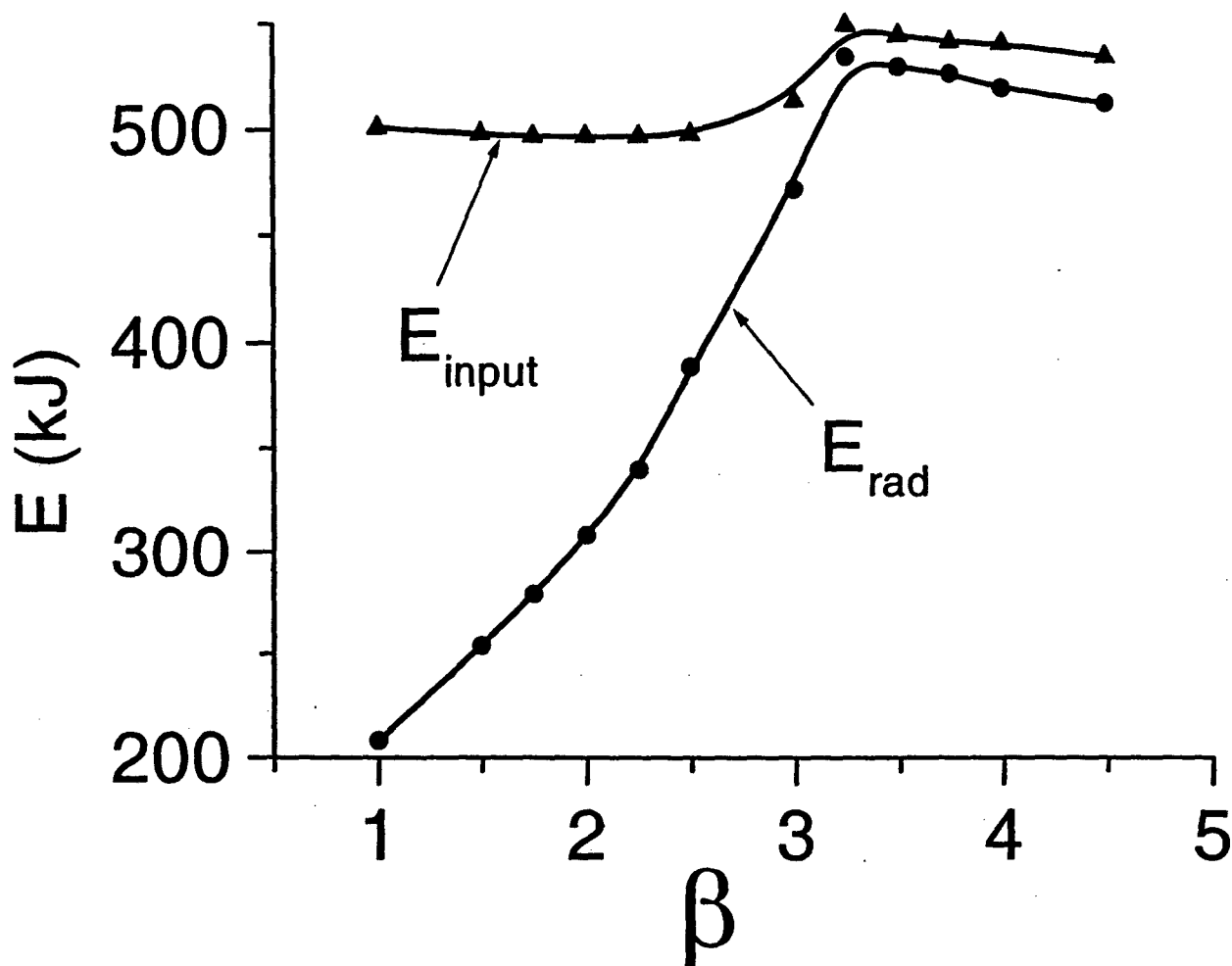


FIG. 8. Variations in the total energy coupled to pinch and in the total energy radiated from the pinch in 200 ns are shown as a function of the L-shell emissivity multiplier. The circuit resistance and α multiplier are the same as in Figs. 4 and 5. Spline fits are drawn to the calculated points.

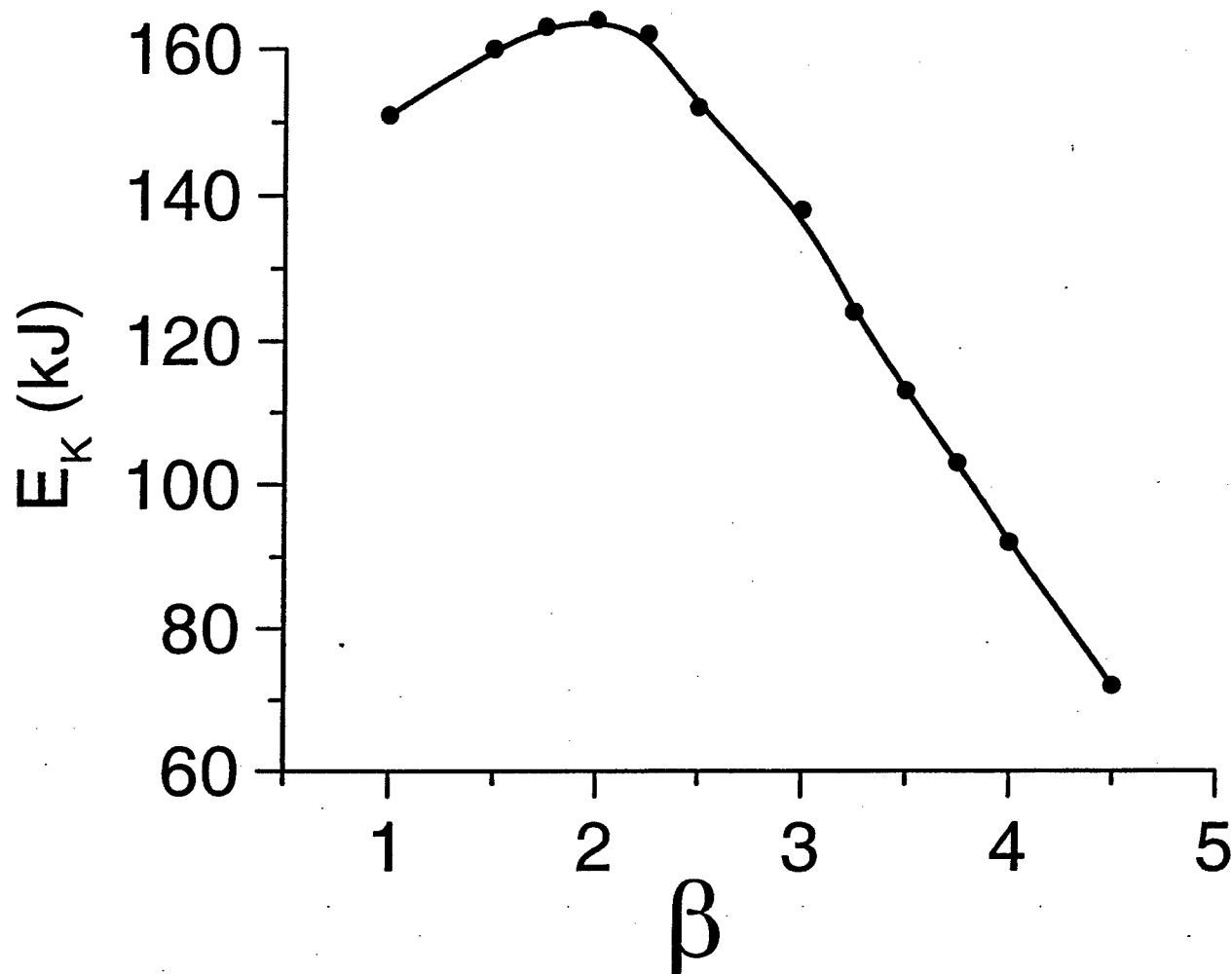


FIG. 9. Variation in the K-shell energy radiated from the pinch in 200 ns is shown as a function of the L-shell emissivity multiplier. The circuit resistance and α multiplier are the same as in Figs. 4 and 5. A spline fit is drawn to the calculated points.

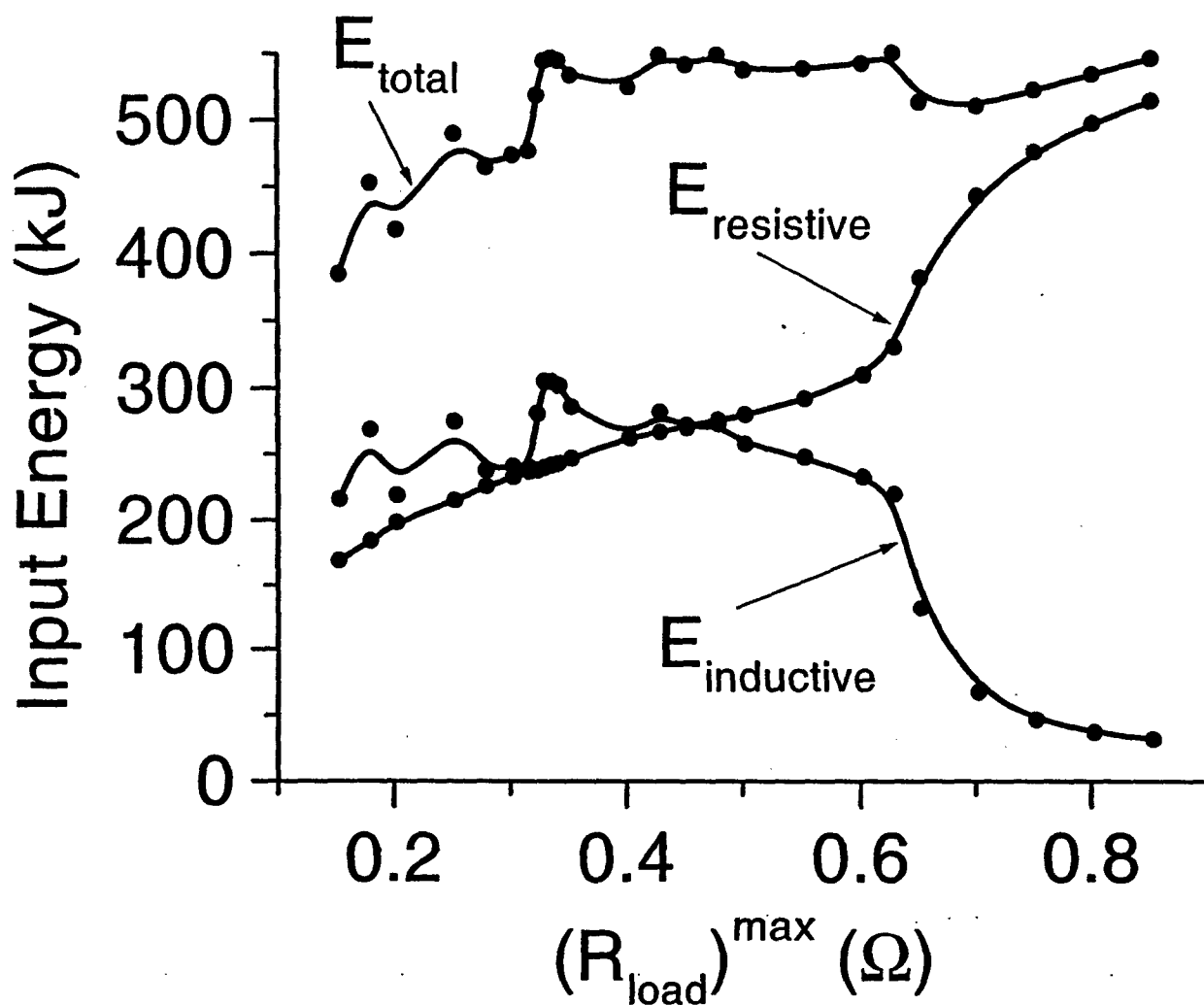


FIG. 10. The total, resistive, and inductive energies coupled to the Z-pinch load are shown as a function of variations in the maximum value of the Fig. 4 circuit resistance. Spline fits are drawn to the calculated points. The oscillations in the inductive coupling at small values of R_{load}^{max} represent numerical error.

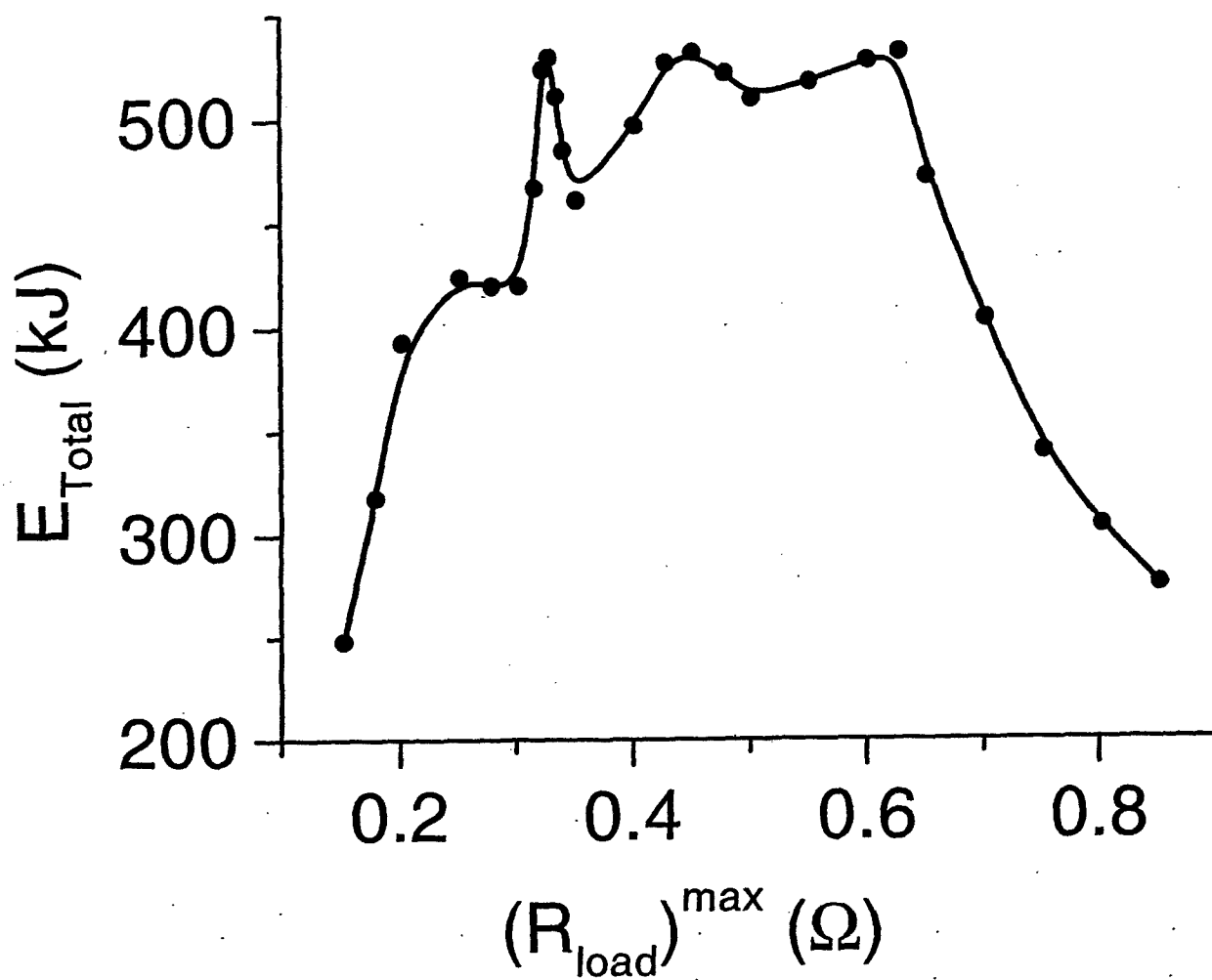


FIG. 11. The total energy radiated from the Z-pinch is shown as a function of variations in the maximum value of the Fig. 4 circuit resistance. A spline fit is drawn to the calculated points.

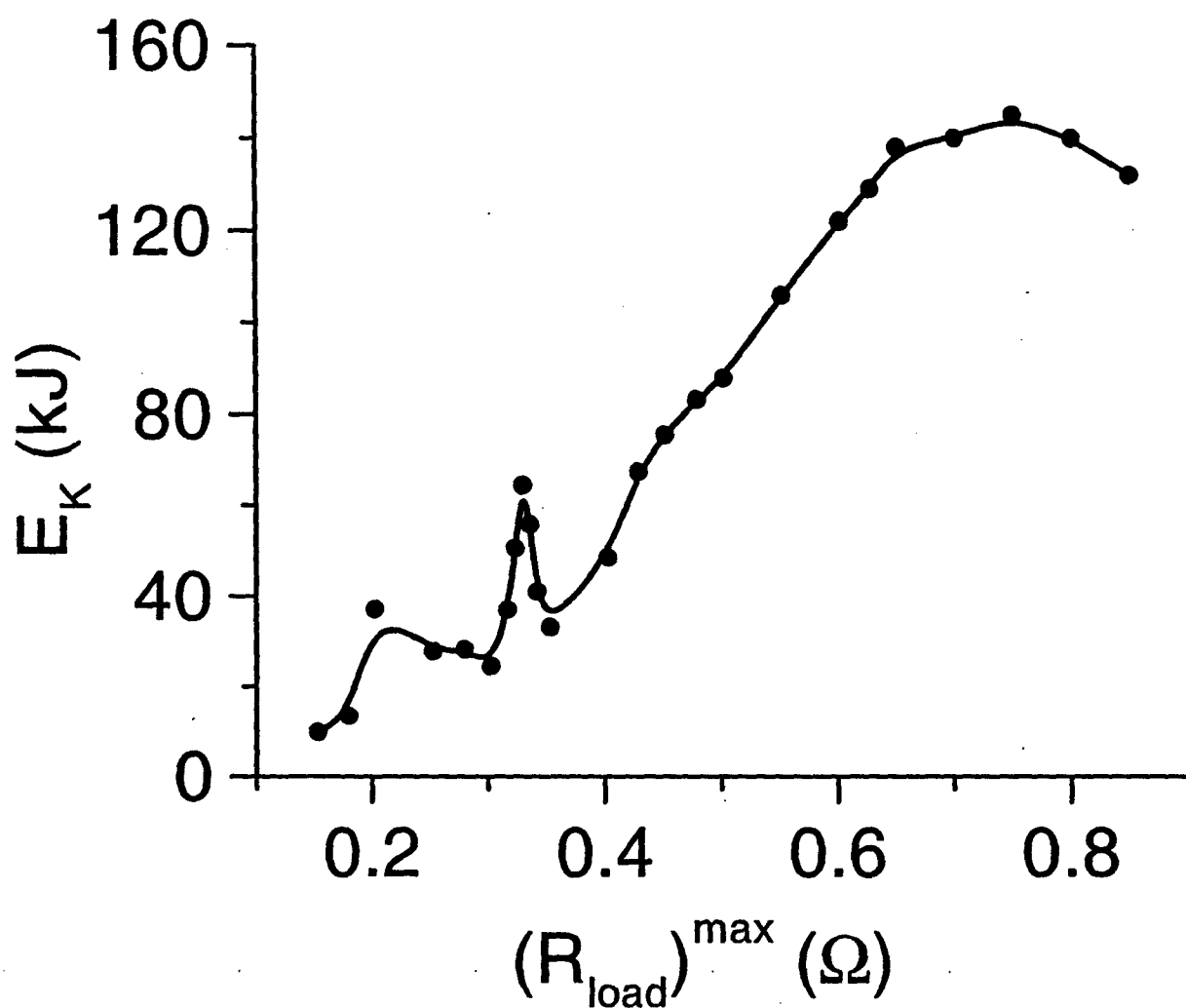


FIG. 12. The K-shell energy radiated from the Z-pinch is shown as a function of variations in the maximum value of the Fig. 4 circuit resistance. A spline fit is drawn to the calculated points.

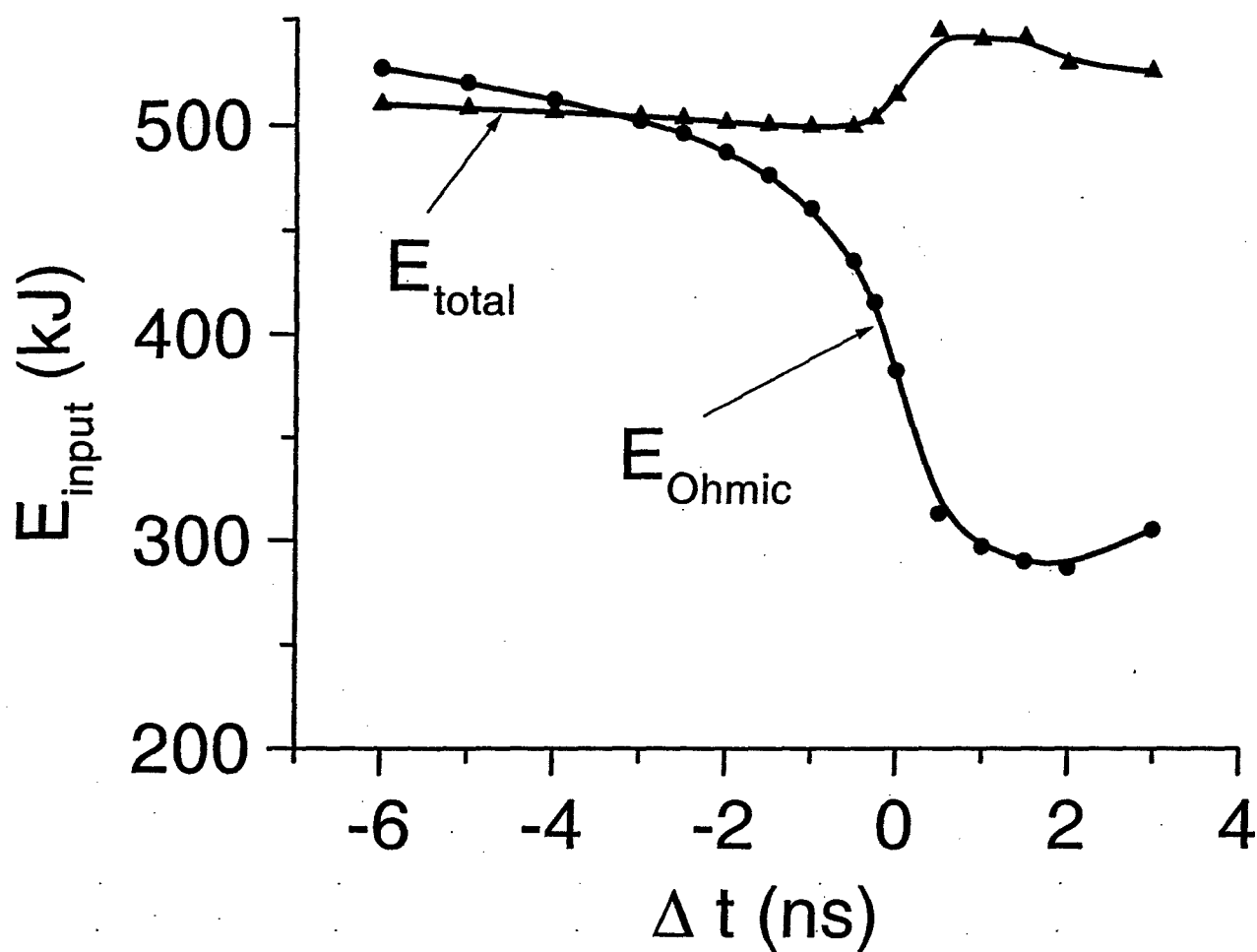


FIG. 13. The total and resistive energies that couple to the Z-pinch are shown as a function of variations in the time to peak resistance of the Fig. 4 circuit resistance. Spline fits are drawn to the calculated points.

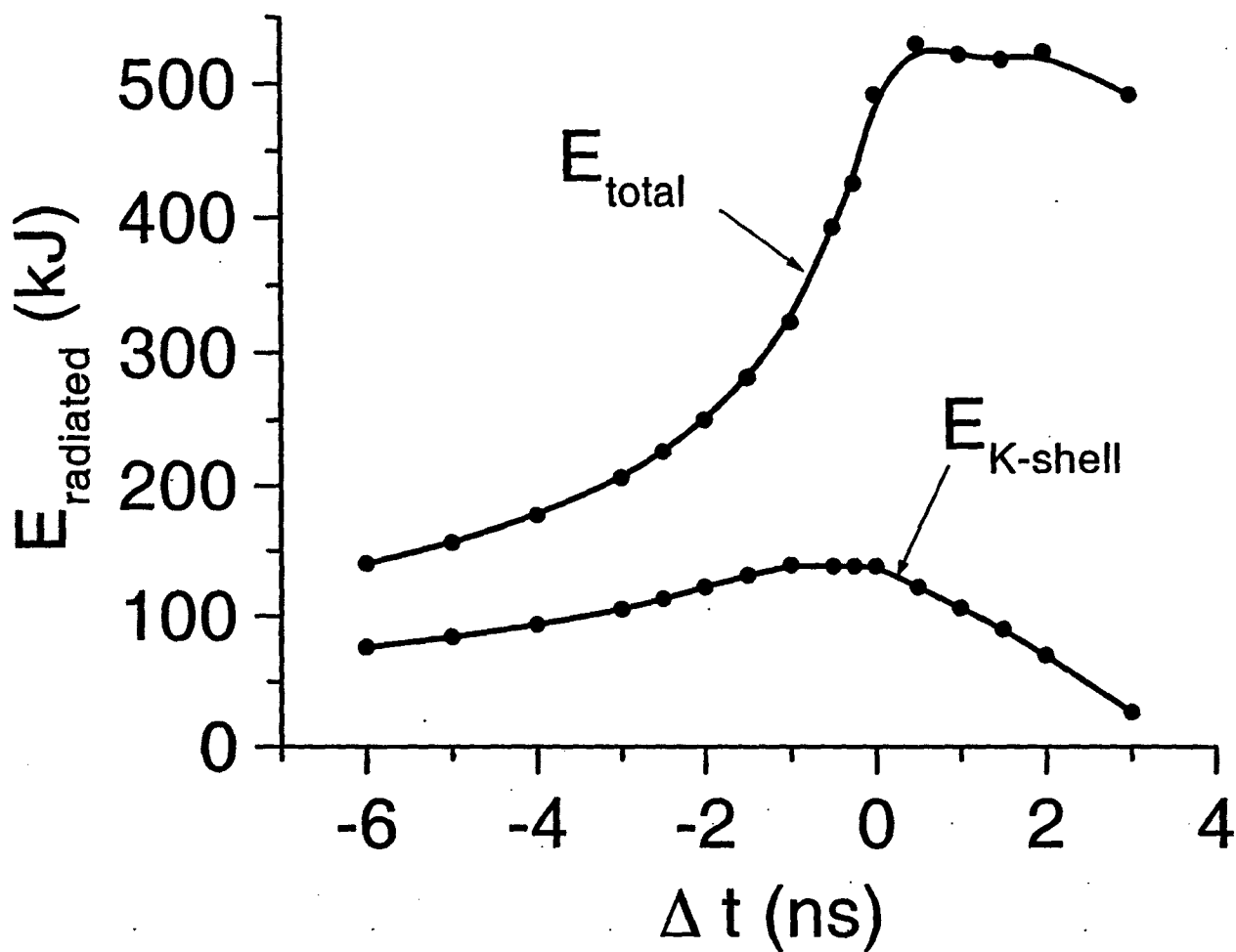


FIG. 14. The total and the K-shell energies that are radiated from the Z-pinch are shown as a function of variations in the time to peak resistance of the Fig. 4 circuit resistance. Spline fits are drawn to the calculated points.

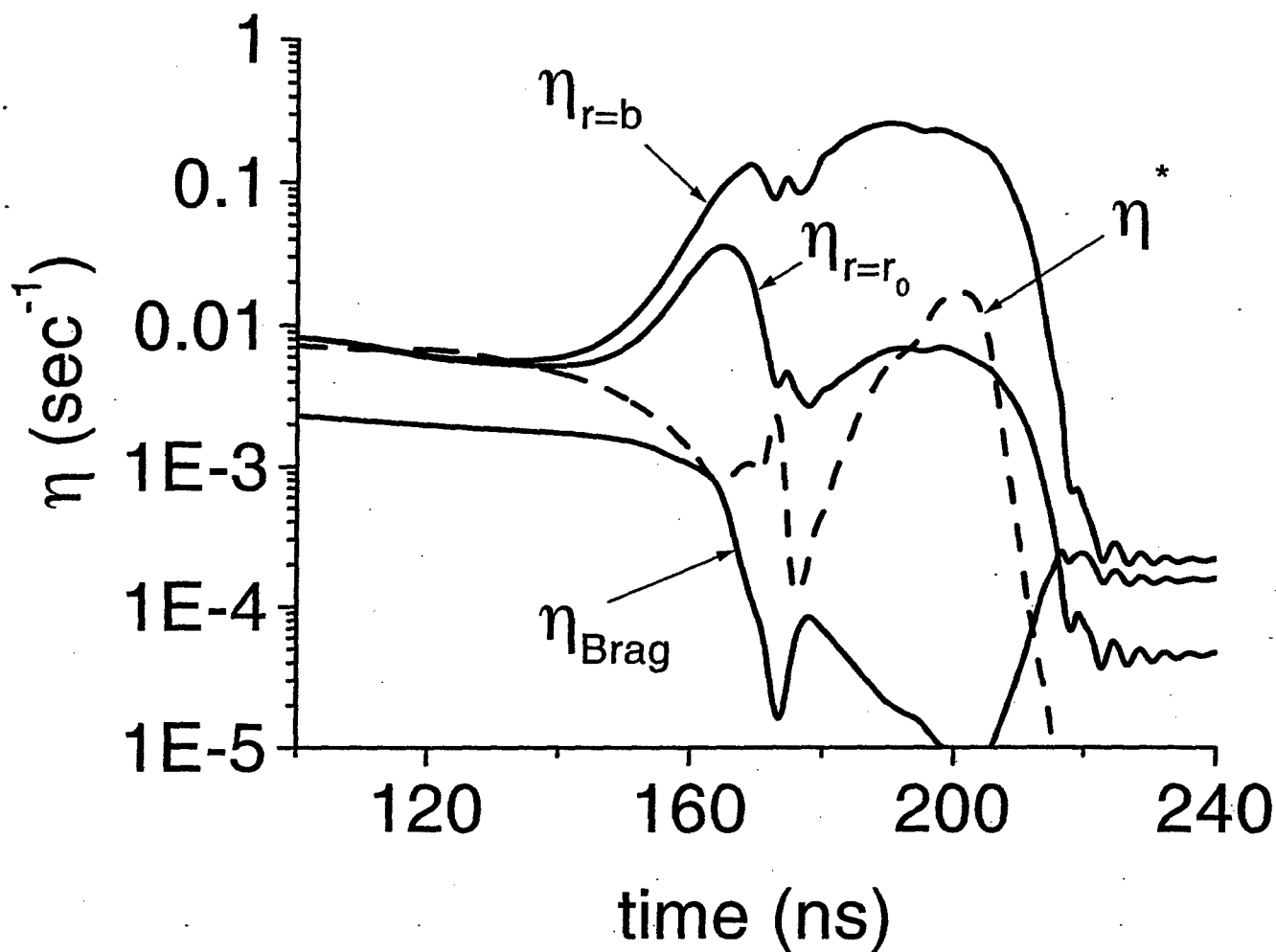


FIG. 15. Four calculated resistivities are shown as functions of time for the Figs. 4 and 5 calculation. The one, labeled η_{Brag} , is derived from $\hat{\alpha}_{\perp}\eta_0$ (η_0 from Eq. (32)). The dashed curve is derived from the drift-wave formula, Eqs. (43). The one, labeled $\eta_{r=b}$, is derived from R_{load} using Eqs. (32) and (40), and the one labeled $\eta_{r=r_0}$ is linearly extrapolated down from $\eta_{r=b}$. r_0 is the inner surface location of the imploding plasma shell.

Confinement and compression of magnetic flux by plasma shells

L. I. Rudakov

Berkeley Scholars, Inc., Springfield, Virginia 22150

A. Chuvatin

Laboratoire de Physique et Technologie des Plasmas, Ecole Polytechnique, 91128 Palaiseau, France

A. L. Velikovich and J. Davis

Plasma Physics Division, Naval Research Laboratory, Washington, DC 20375

(Received 19 May 2003; accepted 4 August 2003)

Confinement and compression of magnetic flux by plasma shells is of interest for a variety of applications associated with keV x-ray production in pulsed-power driven Z-pinch plasma radiation sources (PRS). Confinement of a B_z field with a B_θ field of the pinch current can help stabilize the implosion of a shell from a large initial radius. Compression of the azimuthal magnetic flux in the PRS (secondary) circuit with a plasma shell driven by B_θ field of the primary circuit may represent a new opportunity for using a low-cost, relatively slow pulsed power to generate large amounts of keV x rays. The magnetic field has to be compressed and/or confined by low-mass plasma shells emitting soft x-ray radiation that limits the temperature and conductivity of the shell plasma. The thickness of a plasma shell is established self-consistently during the implosion, and it is not obvious whether or not the shell becomes thick enough to confine or compress the magnetic flux. The results of analytical theory and numerical simulations demonstrate that the flux-compressing capability of a low-beta plasma shell is surprisingly good because the shell is shown to dynamically adjust its thickness so that it always remains of the order of its skin depth. The self-similar profiles of confined magnetic field predicted by the theory are consistently reproduced in the simulations. © 2003 American Institute of Physics. [DOI: 10.1063/1.1614254]

I. INTRODUCTION

Magnetic flux compression (MFC) as a method for generating high magnetic fields and currents has been developed in the late 1950s, independently in the US¹ and in the Soviet Union,² and is still being advanced (see Refs. 3–5 and references therein, as well as the proceedings of the Megagauss conferences). The concept is to compress a closed conducting cavity so rapidly that the magnetic flux trapped inside cannot escape via diffusion through the conducting surface. Then the magnetic field inside the cavity grows in inverse proportion to its shrinking cross-sectional area, due to conservation of the trapped magnetic flux, and so does the induced diamagnetic current that generates this field. In a cylindrical geometry, we can compress either the axial magnetic field inside an annulus, or the azimuthal magnetic field trapped between the central conductor (stator) and the liner imploding onto it (armature). The former configuration—the MC-1-type generator, using the term originally introduced by Sakharov²—produces an ultrahigh pulsed magnetic field (up to ~ 28 MG) in the annulus, whereas the latter one, labeled the MC-2-type generator, produces an ultrahigh current pulse (up to ~ 100 MA) in a load connected to it. These generators are explosively driven, which limits the characteristic velocities of imploding solid conductors at the level of ~ 5 km/s. With initial radii about 5 cm or more, the explosive MFC generators operate in a microsecond range of current and magnetic field rise times. The same time scale is characteristic of other concepts of MFC

generators,⁵ e.g., of those compressing magnetic flux with a converging cylindrical shock wave that converts a dielectric medium into a conductor.⁶

The MFC concept could be advanced to generate currents and fields with nanosecond-range rise times. To make it work the velocity of the conducting liner that compresses the magnetic flux should be of order of 100 km/s. There seems to be no way to accelerate solid conductors to ~ 100 km/s, explosively or otherwise. The magnetic flux could be compressed fast enough only with a low-mass plasma shell. Then the velocities in the desired range, ~ 100 km/s, are well within the reach: In the multi-MA Z-pinch experiments designed to produce keV x rays⁷ or soft x rays to heat a hohlraum,⁸ imploded annular plasmas are routinely accelerated to hundreds of km/s, e.g., see Refs. 9. Hence the shell velocity might not be an issue, but its conductivity can become one, in contrast with the case of a solid conductor. In the latter case, one can ensure that the liner thickness exceeds the skin depth, so that the magnetic flux cannot escape. On the contrary, the in-flight thickness of a plasma liner is not known in advance. Rather, it is determined self-consistently in the course of implosion. With the conductivity of imploding plasma determined by its temperature, which in most cases of interest is controlled by radiative losses, confinement of the compressed magnetic flux is not ensured in advance: the flux can be lost through the plasma shell or be trapped inside it.

A similar theoretical problem had been studied some time ago in connection with the proposal to generate ultrahigh magnetic axial field B_z in a MC-1-like configuration,

with a Z-pinch-driven gas-puff plasma shell used as a conducting liner.¹⁰ It was noted¹¹ that enhanced flux losses characteristic of flux compression could have rendered this concept unworkable. Subsequent theoretical analysis and one-dimensional (1D) simulations¹² had shown that efficient compression of the axial magnetic flux by a plasma shell is possible if the shell velocity is sufficiently high. This conclusion was confirmed in experiments.^{13,14} In particular, there were some indications that in the MFC experiment at 7.5 MA on PROTO-II generator at Sandia, a seed field of 100 kG was compressed to about 42 MG.¹⁴ In Ref. 15, theoretical analysis and experimental observations of improved stability of Z-pinch implosions with external axial magnetic field were reported. More recently, compression of axial magnetic field B_z was studied for the purpose of stabilizing Z-pinch implosions, particularly those starting from large initial radii, in order to increase the K-shell radiation yields of plasma radiation sources (PRS).^{16,17} In contrast with the goal of generating ultrahigh magnetic field, the latter application requires B_z to be as low as possible. It was experimentally demonstrated¹⁷ that stabilization of a double-shell gas-puff load is achieved with a half the initial field B_{z0} (and consequently, a quarter of energy required to compress it) compared to the case of a single shell.¹⁸ Not only the uniformity of radiating pinch plasmas was much better in shots with B_z , but the K-shell yield of neon¹⁷ and argon¹⁶ was shown to increase, for neon by about 40%.

The possibility of generating multi-MA currents via MC-2-like compression of azimuthal magnetic field by an annular plasma liner remained unexplored until it was discussed in Ref. 19 in the context of the authors' concept of a staged Z pinch, where a plasma shell compresses azimuthal magnetic flux initially created inside it by a small seed current passing through a fiber or wire on axis. In late 1990s, Center d'Etudes de Gramat (CEG, France) started an experimental program of K-shell radiation production based on magnetic flux compression, the Sphinx project.²⁰ This effort is aimed at proving MFC to be a viable alternative to more costly conventional power amplification techniques, pulse forming water lines and plasma opening switches. Proof-of-the-principle experiments showing current amplification by MFC were performed on "Z" accelerator at Sandia;²¹ the goals and current status of the Sphinx project are reviewed in Ref. 22.

In this paper, the physics of flux confinement and compression by a dynamic low-beta plasma is studied analytically and numerically. Our main result is that the diffusive losses of compressed magnetic flux do not constitute a serious problem: the plasma is shown to adjust in such a way that its thickness is of the order of its skin depth, and the magnetic flux is essentially conserved. In Sec. II we present analytical theory. In Sec. III, its results will be compared to numerical simulations, and in Sec. IV we conclude with a discussion.

II. THEORY

The problems that we consider here involve acceleration or deceleration of a thin plasma shell by a magnetic pressure.

The best-known example is acceleration of an imploded annular shell to the axis by the azimuthal magnetic field B_θ , converting magnetic energy into the kinetic energy of the shell.^{7,8} When an axial magnetic field B_z is present, which in most cases is small initially, but grows faster than B_θ in the course of implosion ($B_\theta \propto R^{-1}$ and $B_z \propto R^{-2}$), the shell is first accelerated by the pressure of B_θ field and then decelerated by the pressure of B_z field, thus converting its kinetic energy into magnetic energy of the compressed B_z field,¹³⁻¹⁷ as in MC-1 generator. For a current-driven magnetic flux compression of MC-2 type,²⁰⁻²² a plasma shell (armature) is first accelerated by the B_θ field produced in the primary circuit, and then decelerated by the B_θ field in the secondary circuit, thus using its kinetic energy to drive the secondary current.

Let a thin annular shell be initially located at $r=R_0$ and have a radial velocity v_0 towards a perfectly conducting stator column whose radius is R_s . The magnetic field in vacuum between the shell and the stator is produced by the current flowing through the stator and closing through the shell, whose initial value is I_0 . The magnetic field profile in vacuum, at $R_s < r < R_0$, is given by

$$B(r) = \frac{B_0 R_0}{r}, \quad (1)$$

where $B_0 = 2I_0/R_0 c$. Assuming both the stator and the shell to be perfectly conducting, we conclude that magnetic flux trapped in vacuum between them is conserved. Its initial value per unit length is given by

$$\Phi = \int_{R_s}^{R_0} B(r) dr = B_0 R_0 \ln \frac{R_0}{R_s}. \quad (2)$$

Due to conservation of magnetic flux, the right-hand side of Eq. (2) should yield the same value of Φ for R_0 replaced with any other value of the shell radius $r=R$. Therefore, the magnetic field at the surface of the imploding shell at the moment when the shell radius equals R , is given by

$$B(R) = \frac{B_0 R_0}{R} \frac{\ln(R_0/R_s)}{\ln(R/R_s)}. \quad (3)$$

We find the maximum values of magnetic field and current from energy conservation. The initial kinetic energy of the shell is equal to the work done by the magnetic pressure as the shell converges to its minimum radius, $r=R_{\min}$, where it stagnates:

$$\begin{aligned} \frac{1}{2} \mu v_0^2 &= \int_{R_{\min}}^{R_0} \frac{B^2(R)}{8\pi} 2\pi R dR \\ &= \frac{B_0^2 R_0^2 [\ln(R_0/R_s)]^2}{4} \int_{R_{\min}}^{R_0} \frac{dR}{R [\ln(R/R_s)]^2} \\ &= \frac{B_0^2 R_0^2 [\ln(R_0/R_s)]^2}{4} \left[\frac{1}{\ln(R_{\min}/R_s)} - \frac{1}{\ln(R_0/R_s)} \right] \\ &= \frac{B_0^2 R_0^2 \ln(R_0/R_s)}{4} \left(\frac{B_{\max} R_{\min}}{B_0 R_0} - 1 \right) \end{aligned} \quad (4)$$

(here, μ is the shell mass per unit length), so

$$\frac{B_{\max}}{B_0} = \frac{R_0}{R_{\min}} \left(1 + \frac{2\mu v_0^2}{B_0^2 R_0^2 \ln(R_0/R_s)} \right), \quad (5)$$

$$\frac{I_{\max}}{I_0} = 1 + \frac{2\mu v_0^2}{B_0^2 R_0^2 \ln(R_0/R_s)} = \frac{\ln(R_0/R_s)}{\ln(R_{\min}/R_s)}. \quad (6)$$

Equation (6) presents the current amplification as a ratio of two logarithms. To make this ratio large enough (to be of practical interest,²⁰⁻²² magnetic flux compression should amplify the current in the above short-circuit regime at least by a factor of 5–10), the logarithm in the denominator should be small, which implies $R_{\min} - R_s \ll R_{\min}$. It means that the gap spacing between the shell and the stator near stagnation should be much less than the stator radius.

The near-stagnation phase of implosion is the most relevant for current amplification, as well as the most dangerous with respect to the magnetic flux losses, since the radial gradient of magnetic field also peaks at stagnation. Therefore, in what follows we limit ourselves to the radii R that satisfy the inequality $R_0 - R \ll R_0$. In this range, the curvature of the stator and the shell (whose thickness is also assumed to be much less than its radius) is not important, which allows us to use the thin-shell approximation and a planar geometry. In the case of acceleration, a plasma shell of finite conductivity whose thickness (or a characteristic length scale) is $a(t)$, and initial velocity zero, is pushed by a magnetic field $B(t)$ whose time dependence is known. In the case of magnetic flux compression, a plasma shell approaches a perfectly conducting stator, compressing the magnetic field $B(t)$ in the vacuum gap [whose width is $\Delta(t)$] between the shell and the stator. Amplification of the magnetic field is due to compression of magnetic flux in the gap. The magnetic flux, however, is not fully confined to the gap spacing. Some of it is trapped in the plasma shell or lost through it to infinity. We assume that the magnetic field is zero behind the plasma shell, and the flux, having been lost through the shell, is instantly distributed in the infinite space behind it without producing a finite magnetic field there.

The planar limit of Eqs. (5) and (6) corresponds to $R_0 - R_s = \Delta_0 \ll R_0$. Then $\ln(R_0/R_s) \cong \Delta_0/R_0$, the mass per unit length μ is expressed via the mass per unit area M by $\mu = 2\pi R_0 M$, and $R_0/R_{\min} \cong 1$. Equations (5) and (6) in this limit are reduced to

$$\frac{B_{\max}}{B_0} = 1 + \frac{4\pi M v_0^2}{B_0^2 \Delta_0} = \frac{I_{\max}}{I_0}. \quad (7)$$

It is easy to obtain Eq. (7) directly by equating the initial kinetic energy per unit area of the shell $M v_0^2/2$ to the increase in the energy of the compressed field from the initial value $B_0^2 \Delta_0/8\pi$ to the peak value $B_{\max}^2 \Delta_{\min}/8\pi$ at the instant when the shell stagnates, and using the magnetic flux conservation equation appropriate for planar geometry, $B_{\max} \Delta_{\min} = B_0 \Delta_0$, where $\Delta_{\min} = R_{\min} - R_s$ is the minimum gap spacing between the shell and the stator. Formula (7) says that the lower the initial field B_0 is, the higher peak field B_{\max} would be produced, which is not surprising, because the compression ratios required for that must be very high: $\Delta_0/\Delta_{\min} = B_{\max}/B_0$. Since the compression ratio itself is lim-

ited by the instability of the decelerated plasma interface, we can conclude that magnetic field compression ratio is approximately equal to the initial kinetic-to-magnetic energy ratio, and could be made as high as the stability limitations on the radial compression ratio would permit. The question we seek to answer in this study is: What are the additional limitations on magnetic flux compression due to finite conductivity of the plasma shell? Under what conditions do they become critical or turn out to be inessential?

Our physical model is given by the following 1D MHD equations:

$$\frac{\partial \rho}{\partial t} + \frac{\partial}{\partial x}(\rho u) = 0, \quad (8)$$

$$\frac{\partial u}{\partial t} + u \frac{\partial u}{\partial x} + \frac{1}{\rho} \frac{\partial p}{\partial x} + \frac{1}{\rho} \frac{\partial}{\partial x} \frac{B^2}{8\pi} = g(t), \quad (9)$$

$$\frac{\partial B}{\partial t} + \frac{\partial}{\partial x}(Bu) - \frac{\partial}{\partial x} \left(\nu_m \frac{\partial B}{\partial x} \right) = 0. \quad (10)$$

These equations are written in a noninertial reference frame, in which the inner boundary of the plasma shell, which corresponds to $x=0$, is at rest; the effective gravity acceleration in (9) is, of course, $g = -d^2\Delta/dt^2$. The plasma is supposed to be cold, with its kinetic pressure much less than the magnetic pressure (low beta),²³ so that in what follows only the latter is retained in the equation of motion (9). We assume the plasma temperature to be radiation controlled, essentially constant and uniform throughout the bulk of the plasma during the implosion, as in most experimental conditions of interest for keV radiation production in Z-pinch PRS.^{23,24} (Note that by neglecting the thermal pressure, we overestimate the diffusion of magnetic flux through the shell, that is, underestimate the capability of the shell to confine the flux. Indeed, the opposite limiting case of high $\beta_{pl} = 8\pi p/B^2 > 1$ in the volume of the shell accelerated by magnetic pressure to supersonic velocities corresponds to a skin depth much less than the shell thickness, that is, to a perfect confinement of magnetic flux. The 1D simulations—e.g., see Ref. 23—show that $\beta_{pl} \ll 1$ in the volume of the plasma shell at all time prior to stagnation.) Therefore the plasma conductivity σ determined by its temperature, as well as magnetic diffusivity defined as

$$\nu_m = \frac{c^2}{4\pi\sigma} = \text{const} \quad (11)$$

are assumed constant below.²⁴

Our initial and boundary conditions are, respectively,

$$B(0) = B_0, \quad a(0) = a_0, \quad \Delta(0) = \Delta_0,$$

$$\left(\frac{d\Delta}{dt} \right)_{t=0} = -v_0 \quad (12)$$

(the case of shell acceleration from zero velocity corresponds to $v_0=0$),

$$B = B(t) \quad \text{at } x=0; \quad B=0 \quad \text{at } x=a(t) \quad \text{or at } x \rightarrow \infty. \quad (13)$$

The thin-shell approximation assumes the time variation of the boundary conditions to be much slower than it takes for a fast magnetosonic wave to travel across the plasma shell, thus establishing homogeneous deformation throughout the bulk of the plasma (see Refs. 12 and 25 and references therein). We therefore seek a solution of Eqs. (8)–(10) with the initial and boundary conditions (12) and (13) within the class of self-similar solutions with homogeneous deformation, as in Ref. 12. Some particular solution of this type was first investigated in Ref. 26. We choose the time unit as

$$t_0 = \frac{1}{B_0} (8\pi M \Delta_0)^{1/2}, \quad (14)$$

introduce dimensionless time, self-similar coordinate and compression ratio as

$$\tau = t/t_0, \quad \eta = x/a(\tau), \quad \alpha(\tau) = a(\tau)/a_0, \quad (15)$$

and use the self-similarity ansatz

$$u = \frac{a_0}{t_0} \frac{d\alpha}{d\tau} \eta, \quad \rho = \rho_0 \frac{N(\eta)}{\alpha(\tau)}, \quad B = B_0 \beta(\tau) H(\eta). \quad (16)$$

Here, the normalization constant ρ_0 is chosen so that the total areal mass of the plasma shell $M = \rho_0 a_0$. The dimensionless density function $N(\eta)$ should thereby satisfy the normalization condition

$$\int_0^{\eta_m} N(\eta) d\eta = 1, \quad (17)$$

where $\eta = \eta_m$ corresponds to the outer boundary of the plasma shell ($\eta_m = \infty$ if the shell is diffuse).

Substituting (15) and (16) into (8), we find that the continuity equation is identically satisfied with arbitrary density function $N(\eta)$. The equation of motion (9) is reduced to

$$\frac{a_0}{\Delta_0} \ddot{\alpha} \eta + \beta^2 \frac{1}{N} \frac{d}{d\eta} H^2 = -\delta, \quad (18)$$

where $\delta(\tau) = \Delta(\tau)/\Delta_0$ is the dimensionless gap between the shell and the stator, and the dot denotes differentiation with respect to normalized time, τ .

The thin-shell approximation means neglecting the first term in the left-hand side of (18) compared to its right-hand side. It is justified, at least for some time, because of the smallness of the initial ratio a_0/Δ_0 . For our solution to be applicable, we need to verify the smallness of $(a_0/\Delta_0) \times (\ddot{\alpha}/\delta)$ in the process of compression.

The thin-shell approximation allows us to separate the variables in Eq. (18) if the η -dependent term is constant. The choice of this constant

$$N = -\frac{d}{d\eta} H^2 \quad (19)$$

satisfies the normalization condition (17), since the initial and boundary conditions (12), (13) for B imply that

$$H(0) = 1, \quad H(\eta_m) = 0. \quad (20)$$

The solution is physically meaningful only if $N(\eta) \geq 0$ for all η , so the derivative of magnetic field (and thus, the current density) cannot change sign.

Substitution of (19) into (18) yields

$$\ddot{\delta} = \beta^2. \quad (21)$$

Then the induction equation (10) transforms into

$$\alpha^2 \left(\frac{\beta}{\alpha} + \frac{\dot{\alpha}}{\alpha} \right) = \frac{1}{Rm} \frac{1}{H} \frac{d^2 H}{d\eta^2}, \quad (22)$$

where the magnetic Reynolds number is defined as

$$Rm = a_0^2 / \nu_m t_0. \quad (23)$$

The left-hand side of Eq. (22) depends only on τ , the right-hand side on η . The variables in Eq. (22) could only be separated if both the left- and right-hand sides of this equation are equal to some separation constant. We denote this constant $\pm s^2$, depending on its sign. Three options are immediately seen.

(1) Separation constant is positive, $+s^2$. Then the profile shape is exponential:

$$H(\eta) = \exp(-\eta s \sqrt{Rm}) - \frac{2}{\exp(2\eta_m s \sqrt{Rm}) - 1} \sinh(\eta s \sqrt{Rm}). \quad (24)$$

This choice of constants satisfies the boundary conditions (20). If the plasma shell is diffuse and extends to infinity ($\eta_m = \infty$), then only the decaying exponential remains. We see that this solution exists and is physically meaningful [corresponds to a positive $N(\eta)$ in Eq. (19)] for any η_m . In this case the magnetic flux contained in the plasma

$$\begin{aligned} \Phi_{pl}(\tau) &= \int_0^{\Delta_m} B dx = a_0 B_0 \alpha(\tau) \beta(\tau) \int_0^{\eta_m} H(\eta) d\eta \\ &= \frac{a_0 B_0 \alpha(\tau) \beta(\tau)}{s \sqrt{Rm}} \tanh\left(\frac{\eta_m}{2} s \sqrt{Rm}\right) \end{aligned} \quad (25)$$

grows with time.

(2) Separation constant is zero. The magnetic field profile is linear,

$$H(\eta) = 1 - \eta / \eta_m. \quad (26)$$

The shell thickness is finite. Again, the solution is physically meaningful for arbitrary η_m . The magnetic flux contained in the shell is constant in time: as much flux diffuses from the inside as is lost through the outside surface.

(3) Separation constant is negative, $-s^2$. The profile shape is trigonometric

$$H(\eta) = \cos(\eta s \sqrt{Rm}) - \cot(\eta_m s \sqrt{Rm}) \sin(\eta s \sqrt{Rm}). \quad (27)$$

The solution is only physically meaningful for $\eta_m s \sqrt{Rm} < \pi/2$. The magnetic flux contained in the shell decreases with time, since more flux is lost through the outside surface than added via diffusion from the inside.

Let us consider the first option, which obviously is the most interesting physically. We derived two equations, (21) and

$$\frac{\dot{\beta}}{\beta} + \frac{\dot{\alpha}}{\alpha} = \frac{s^2}{\alpha^2}. \quad (28)$$

For the particular case of the exponential solution with $\eta_m = \infty$, we can reduce the number of dimensionless parameters of the system using its symmetry. Indeed, the definition of the length scale $a(t)$ characteristic of the exponential profile allows multiplying it by any number $a(t) \rightarrow \lambda a(t)$. Consequently, we have some arbitrariness in the choice of a_0 and Rm : our exponential solution depends on $xs\sqrt{Rm}/a_0\alpha(t) = xs/\alpha(t)\sqrt{\nu_m t_0}$, a combination, which does not include a_0 at all. Thus we can define a_0 by postulating

$$s = \frac{1}{\sqrt{Rm}}, \quad (29)$$

which simplifies the expressions for the profiles of magnetic field and density,

$$H(\eta) = \exp(-\eta), \quad N(\eta) = 2 \exp(-2\eta), \quad (30)$$

and transforms (28) into

$$\frac{\dot{\beta}}{\beta} + \frac{\dot{\alpha}}{\alpha} = \frac{1}{\alpha^2 Rm}. \quad (31)$$

For the simple case of a shell acceleration by a known magnetic field $B(t) = B_0 \beta(\tau)$ Eqs. (21) and (31) are immediately integrated. In particular,

$$\alpha(\tau) = \left[\frac{2}{Rm \beta^2(\tau)} \left(\alpha_0 + \int_0^\tau \beta^2(\tau') d\tau' \right) \right]^{1/2}, \quad (32)$$

where α_0 is a positive integration constant. When $B(t)$ is either constant, or linearly rising with time, or decreasing as $1/t$, Eq. (32) implies

$$a(t) = \begin{cases} (2\nu_m t)^{1/2}, & B(t) = B_0 \theta(t), \\ (2\nu_m t/3)^{1/2}, & B(t) = B_0 t/t_1, \\ (2\nu_m t(t+t_1)/t_1)^{1/2}, & B(t) = B_0 t_1/(t+t_1). \end{cases} \quad (33)$$

We have substituted here the definition (23) of Rm to convert the result into a dimensional form. Not surprisingly, it does not contain the arbitrary normalization constant, a_0 . The square-root time dependence in (33) is something one expects when dealing with diffusion. Note, however, that the magnetic field profiles are not Gaussian, as typical for self-similar diffusion into an incompressible medium in planar geometry,²⁷⁻³⁰ but rather exponential!

This simple solution allows us to estimate the role of the omitted thermal pressure term in the equation of motion (9). For instance, taking the self-similar solution (33) for constant magnetic pressure, we find that the ratio of the omitted thermal pressure term to the retained magnetic pressure term equals to

$$\frac{\partial p / \partial x}{(\partial / \partial x) B^2 / 8\pi} = \frac{16\pi(1+Z)n_0 T_0 a_0}{(2\nu_m t)^{1/2} B_0^2} \ll 1, \quad (34)$$

where T_0 is the constant temperature of the plasma, and Z is the corresponding average ion charge. The ratio (34) is uniform over the shell volume. It is initially small due to small-

ness of the thermal pressure compared to magnetic pressure, and additionally decreases with time due to diffusion [the short time interval when the term $(2\nu_m t)^{1/2}$ in the denominator is much smaller than a_0 is of no importance because it corresponds to the transient phase when the self-similar profiles are formed, see Sec. III B].

For the case of magnetic flux compression, the time dependence of compressed magnetic field $\beta(\tau)$ is not known in advance; rather, it should be determined self-consistently, together with $\alpha(\tau)$ and $\delta(\tau)$. To close the system (21) and (31), we need one more equation. It can be derived from conservation of magnetic flux. If, for instance, we assume that no flux losses take place through the outer surface (which means a diffuse shell, $\eta_m = \infty$), then we can state

$$\begin{aligned} \Phi_{pl} + \Phi_{vac} &= a_0 B_0 \alpha(\tau) \beta(\tau) + \Delta_0 B_0 \delta(\tau) \beta(\tau) \\ &= \Phi_0 = \text{const} \end{aligned} \quad (35)$$

or

$$\delta = \frac{\Phi_0}{B_0 \Delta_0} \times \frac{1}{\beta} - \frac{a_0}{\Delta_0} \times \alpha = \frac{1}{\beta} + \frac{\Phi_{0,pl}}{\Phi_{0,vac}} \left(\frac{1}{\beta} - \alpha \right). \quad (36)$$

Here,

$$\frac{\Phi_{0,pl}}{\Phi_{0,vac}} = \frac{a_0}{\Delta_0}, \quad (37)$$

denotes the ratio of magnetic fluxes initially contained in the shell plasma and in vacuum between the shell and the stator, respectively. In other words, the initial ratio of magnetic fluxes contained in the gap and in the shell is equal to the ratio of their length scales according to the definition of a_0 given by (29).

Thus we have defined all the dimensionless parameters on which the solution depends in the case of magnetic flux compression. They are the small ratio of initial magnetic energy in the gap to the initial kinetic energy of the shell,

$$\varepsilon = \frac{B_0^2 \Delta_0}{4\pi M v_0^2} \ll 1, \quad (38)$$

the small ratio of initial shell thickness to the initial gap spacing,

$$\phi = \frac{a_0}{\Delta_0} = \frac{\Phi_{0,pl}}{\Phi_{0,vac}} \ll 1, \quad (39)$$

and the magnetic Reynolds number defined by (23) with the length scale a_0 consistent with (29). The magnetic Reynolds number could be either large or small. Recall that its large value implies high conductivity, whereas small Rm corresponds to a strong diffusion of magnetic field. Equation (36) is presented as

$$\delta = \frac{1 + \phi}{\beta} - \phi \alpha. \quad (40)$$

The initial conditions for the variables α , β , δ are

$$\alpha(0) = \beta(0) = \delta(0) = 1. \quad (41)$$

The initial velocity of the shell is $-v_0$, the corresponding normalized combination being $v_0 t_0 / \Delta_0 = (8\pi M v_0^2 / B_0^2 \Delta_0)^{1/2} = (2/\varepsilon)^{1/2}$, see (14) and (38). Therefore, $\dot{\delta}(0) = -(2/\varepsilon)^{1/2}$, which implies

$$\dot{\alpha}(0) = \frac{1+\phi}{Rm} - (2/\varepsilon)^{1/2}, \quad (42)$$

Eqs. (21) and (31) are rewritten in the form

$$\dot{\alpha} = v, \quad (43)$$

$$\dot{\beta} = \frac{\beta(1-\alpha v Rm)}{\alpha^2 Rm}, \quad (44)$$

$$\dot{v} = -\frac{1+\phi-\alpha^4\beta^3 Rm^2}{(1+\phi-\alpha\beta\phi)\alpha^3 Rm^2}. \quad (45)$$

With initial conditions for α , β , and v given by (41), (42), our problem is well defined. In the limit of perfect conductivity, $Rm \rightarrow \infty$, we find from (31), $\beta = 1/\alpha$, as expected from conservation of flux, $\delta = \alpha$, and (43) and (45) reduce to $\ddot{\alpha} = \alpha^{-2}$. This corresponds to the maximum compressed magnetic field at the instant when $\dot{\alpha}(\tau) = 0$ and the plasma shell bounces from it, $\beta_{\max} = 1 + \varepsilon^{-1}$, which exactly reproduces (7), as it should be.

Efficiency of magnetic flux compression is demonstrated in Fig. 1 for Rm ranging between 0.1 and 100 with $\varepsilon = 0.1$, $\phi = 0.01$ and 0.1. A perfect conductor would have amplified the initial magnetic field by a factor of $1 + \varepsilon^{-1} = 11$. Figure 1 shows that even for magnetic Reynolds number Rm as low as 0.1, the peak compression still exceeds 9. The ratio of the skin depth defined as $\Lambda_s = (v_m |\alpha/\dot{\alpha}|)^{1/2}$ to the characteristic thickness of the plasma shell estimated from its density gradient as $a_0 \alpha$, is

$$\frac{\Lambda_s}{a_0 \alpha} = [Rm(2/\varepsilon)^{1/2} - \phi - 1]^{-1/2} \times \left[\frac{\dot{\alpha}(0)}{\alpha(\tau)\dot{\alpha}(\tau)} \right]^{1/2}. \quad (46)$$

The right-hand side of (46) remains of order unity for most of the implosion.

III. NUMERICAL SIMULATION

A. Formulation of the problem

The above analysis was based on the self-similar solutions of Eqs. (8)–(10), corresponding to certain boundary conditions. The self-similar profiles of density and magnetic field correspond to the case when the magnetic flux is successfully confined and compressed. These profiles are expected to be rapidly established, which means that the shell acceleration or deceleration distances are much smaller than Δ_0 . The self-similar flow, representing an *intermediate asymptotics* of a wider class of solutions,²⁹ is formed when the solution forgets the form of initial motion, but selects from the entire set of information provided by the initial conditions, such as initial density profile, a limited number of parameters determining a self-similar solution.³⁰ The theory does not allow us to model the transient phase when the self-similar flow is formed or to estimate the duration of this phase. It also does not describe the situation near the turning point, when the magnetic fields on both sides of the shell are

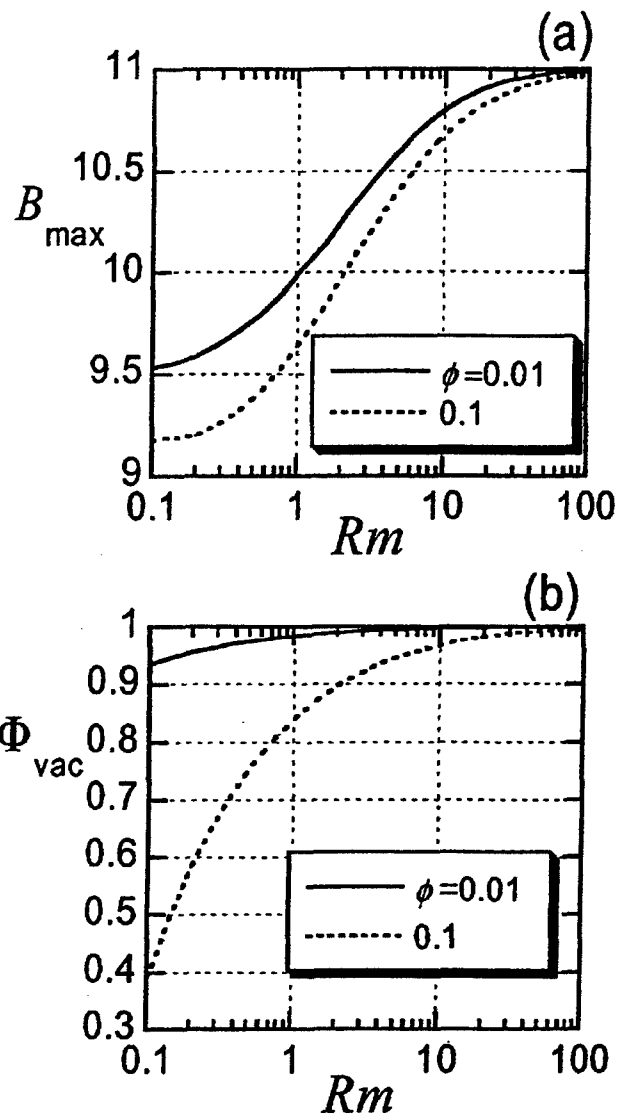


FIG. 1. Peak compressed magnetic field (a) and magnetic flux confined in vacuum between the shell and the stator (b) vs magnetic Reynolds number, calculated for two values of the parameter ϕ (39). Both B_{\max} and Φ_{vac} are normalized to their respective initial values in vacuum.

comparable and have a different time dependence. To investigate these cases, a numerical simulation is needed.

As in Sec. II, we assume the temperature of the accelerated plasma to be radiation controlled (the Joule heating is compensated by radiation losses) and thereby constant, sufficiently low to neglect thermal pressure of the plasma in comparison with the magnetic pressure. Our basic equations therefore are those of continuity and motion, and the induction equations for a two-component magnetic field, which are presented below in Lagrangian variables for an inertial reference frame

$$\frac{\partial}{\partial t} \left(\frac{1}{\rho} \right) = \frac{\partial u}{\partial \xi}, \quad (47)$$

$$\frac{\partial u}{\partial t} + \frac{\partial}{\partial \xi} (B_y^2 + B_z^2) = 0, \quad (48)$$

$$\frac{\partial}{\partial t} \left(\frac{B_y}{\rho} \right) = \frac{\partial}{\partial \xi} \left(\frac{\rho}{Rm} \frac{\partial B_y}{\partial \xi} \right), \quad \frac{\partial}{\partial t} \left(\frac{B_z}{\rho} \right) = \frac{\partial}{\partial \xi} \left(\frac{\rho}{Rm} \frac{\partial B_z}{\partial \xi} \right), \quad (49)$$

where

$$\xi \equiv \int_{x_{\min}}^x \rho(x', t) dx' \quad (50)$$

is the Lagrangian mass coordinate, and Rm the magnetic Reynolds number. The system (47)–(49) is further approximated by an algebraic system of equations for discrete values of unknown functions ρ , u , and $B_{x,y}$ on a 1D spatial grid, ξ_i , and solved numerically. We used a fully conservative finite difference approximation scheme, as described in detail in Ref. 31. Detailed discussion of this numerical technique is beyond the scope of the present paper. We only note that implementation of such schemes was already shown to be efficient even for solution of much more complicated, two-dimensional (2D) radiative magnetohydrodynamic problems.³²

We use dimensionless variables here. Both components of magnetic field and density are normalized with respect to their initial values, B_{y0} and ρ_0 , respectively. The x -coordinate is normalized with respect to the initial thickness of the shell, a_0 ; the time unit is

$$t_0 \equiv \frac{a_0 \sqrt{8\pi\rho_0}}{B_{y0}}. \quad (51)$$

This definition differs from (14) by a factor of $(a_0/\Delta_0)^{1/2} \ll 1$. Consequently, this normalization makes the magnetic Reynolds number defined by the same Eq. (23) larger by a factor of $(\Delta_0/a_0)^{1/2} \gg 1$.

The energy conservation equation follows from Eqs. (47)–(49). The sum of kinetic and magnetic energies is not conserved because of the Joule dissipation of magnetic energy. $j^2/\sigma \propto (p^2/Rm) \times [(\partial B_y/\partial \xi)^2 + (\partial B_z/\partial \xi)^2]$.

The initial conditions are set as shown in Fig. 2. The computational area extends between $x = x_{\min} < 0$ and $x = x_{\max} > 0$. The plasma shell mass is distributed between $x = 0$ and $x = 1$ (in Fig. 2—uniformly, with constant density $\rho = 1$, but any other initial density profile in the shell is possible). We assume a presence of a uniform low-density plasma with $\rho = \rho_{\min} \ll 1$ at $x_{\min} < x < 0$ and $1 < x < x_{\max}$. The layer between $x = x_{\min}$ and $x = x_{\text{stator}} = -\Delta_0$ represents a motionless, highly conductive electrode, “the stator,” that confines the magnetic flux from the left side of the computational area, and Δ_0 , as above, is the initial distance between the shell and the stator, satisfying the thin-shell assumption of Sec. II, $\Delta_0 \gg a_0$. The corresponding values of the Lagrangian mass coordinate ξ are 0 at $x = x_{\min}$, ξ_{stator} , ξ_0 , and ξ_1 at the inner and outer boundary of the shell, and ξ_{\max} . Mass of the low-density plasma in the gap is taken to be much smaller than that of the plasma shell, $\rho_{\min} \ll 1/|x_{\min}|$, and therefore $\xi_1 \gg \xi_0$.

As in Sec. II, the assumption of constant temperature implies constant values of magnetic viscosity ν_m (11) and magnetic Reynolds number Rm (23). Ideally, the magnetic Reynolds number is finite in the plasma shell, zero in the gap between the shell and the stator and behind the shell, and infinite in the stator. In our numerical simulation, we assume

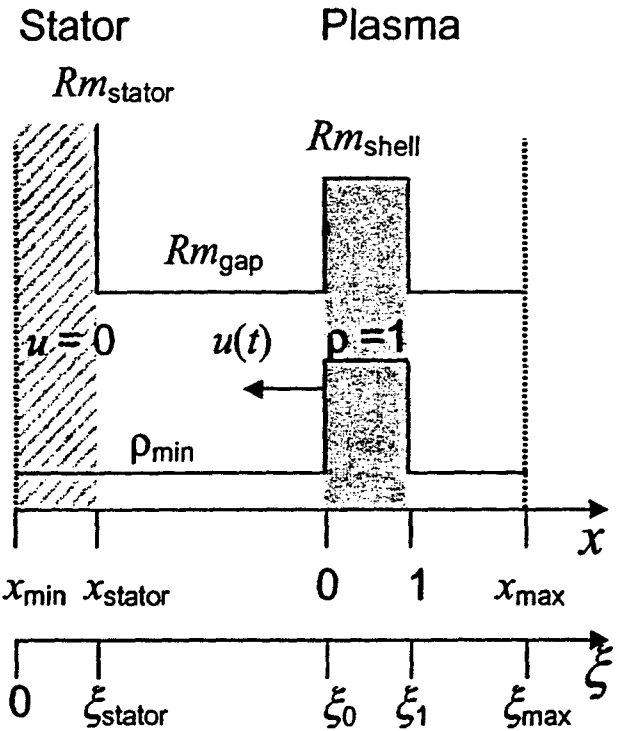


FIG. 2. Schematic of the geometry of our numerical problem. Solid lines are initial profiles of plasma density ρ (the gray area represents the plasma shell, shown for a flat density profile) and magnetic Reynolds number Rm . The shaded area on the left side is the motionless stator. Lagrangian marker ξ_{\max} on the right is the boundary of a low-density “background” plasma ($\rho = \rho_{\max}$), at which external magnetic field can be prescribed. Alternatively, the second stator could be added between x'_{stator} and x_{\max} .

for these respective magnetic Reynolds numbers some finite constant values satisfying the inequalities $Rm_{\text{gap}} \ll Rm_{\text{shell}} \ll Rm_{\text{stator}}$. The value of Rm_{shell} is varied between the limits of weakly conducting ($Rm_{\text{shell}} < 1$) and strongly conducting ($Rm_{\text{shell}} \gg 1$) plasma.

Now we define our boundary conditions. In the motionless, highly conducting stator, we assume

$$u(\xi, t) = 0 \text{ at } 0 \leq \xi \leq \xi_{\text{stator}} \text{ and } B_{y,z}(\xi = 0, t) = 0. \quad (52)$$

The boundary conditions on the other side of the shell depend on the problem addressed. We can have another electrode, like a stator (the case of a magnetic cavity with two walls and with a bouncing shell, see below), and thus impose boundary conditions like (52), where ξ_{stator} and $\xi = 0$ are replaced with ξ'_{stator} and $\xi_{\max} > \xi'_{\text{stator}}$. Alternatively, we can apply an external source, “a generator” of magnetic flux at the right boundary, assuming that

$$u(\xi = \xi_{\max}, t) = 0, \quad B_y(\xi = \xi_{\max}, t) = b(t), \quad (53)$$

where $b(t)$ is a known function. The other component of the magnetic field is maintained constant at this boundary: $B_z(\xi = \xi_{\max}, t)$ equals its initial value, which is either 0 or 1.

B. Simulation results

Figure 3 shows the profiles of density and magnetic field obtained numerically for a constant one-component magnetic field instantly applied to the right side of the computational

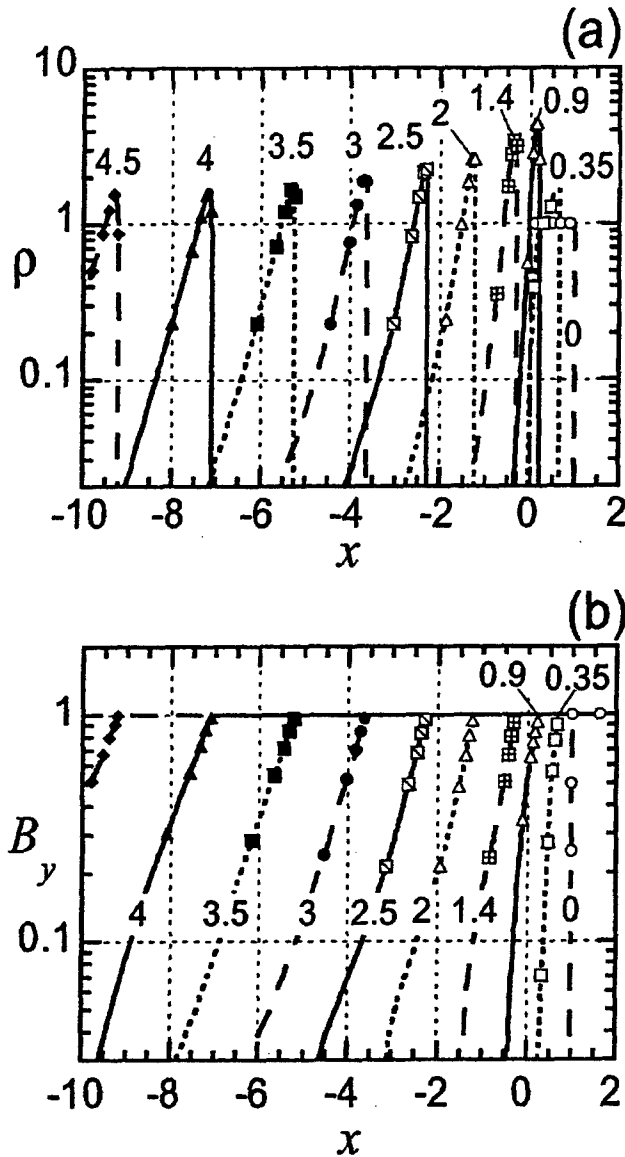


FIG. 3. Successive density (a) and magnetic field (b) profiles obtained numerically for $Rm_{shell} = 10$, $B_z = 0$. The profiles here and below are labeled by the respective times expressed in units (51). The plasma shell is accelerated by a constant external magnetic field.

area: in Eq. (53) $b(t) = \theta(t)$, the Heaviside step function. The profiles are shown vs the dimensionless coordinate

$$x(t, \xi) = \int_0^\xi \frac{d\xi'}{\rho(t, \xi')} + x_{min} \quad (54)$$

shifted by x_{min} , so that the left boundary of the stator corresponds to $\xi = 0$, as shown in Fig. 2. The magnetic pressure accelerates the plasma shell towards the stator, in the negative x direction, while the magnetic flux diffuses through the shell due to its finite conductivity. Here we have chosen $x_{stator} = -70$ (which means $\Delta_0/a_0 = 70$), and a high conductivity of the plasma shell: $Rm_{shell} = 10$. We have taken $B_z = 0$. Here and below, the choice of other constants is arbitrary; we have checked that for $\rho_{min} \leq 10^{-3}$, $Rm_{gap} \leq 10^{-3}$, $Rm_{stator} \geq 10^3$ it does not affect the numerical solution.

The shell, accelerated and compressed by the pressure of the magnetic field B_y from the right, moves to the left. By the time $t = 2$, after the shell has traveled about twice its

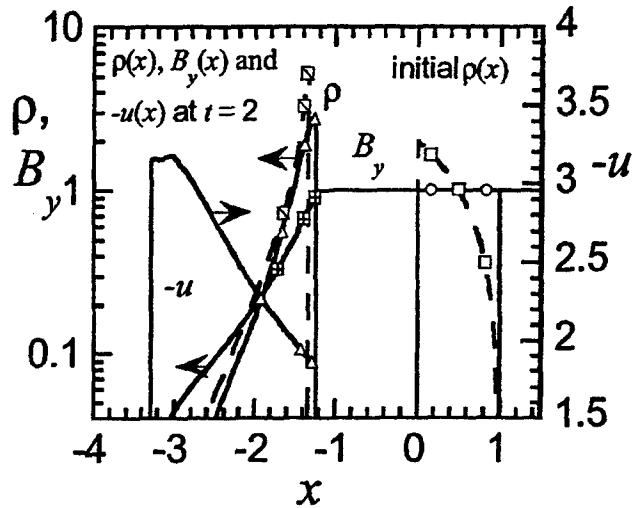


FIG. 4. Initial density profiles (flat—solid curve, same as in Fig. 3, and linear—dashed curve); density (for both cases), velocity and magnetic field profiles (for flat initial density profile) at $t = 2$.

initial thickness, to $x = -2$, the theoretically predicted exponential profiles (which are linear on the semilogarithmic plots of Fig. 3) are seen to be already established with a good accuracy.

Figure 4 illustrates that this agreement holds for a variety of initial profiles. Here the density profiles shown for $t = 2$ in Fig. 2 are compared to those obtained for the initial linear density profile in the shell, $\rho_{shell}(x, 0) = 2(1 - x)$ (dashed lines). In the latter case the initial shell mass is unchanged and the density decreases linearly from $\rho_{shell}(0) = 2$ to $\rho_{shell}(1) = 0$ (if we neglect $\rho_{min} \ll 1$). By $t = 2$, density profiles for both cases approach the exponential shape predicted by the theory. The velocity profile shown in Fig. 4 is close to linear, also in agreement with the theory.

If the plasma shell were incompressible and perfectly conducting, then its zero-dimensional (0D) equation of motion would be $\rho(d^2\Delta_a/dt^2) = B^2$, where Δ_a is the positive distance traveled by the shell. With $\rho = 1$ and $B = 1$, its solution describes a constant acceleration: $\Delta_a = t^2/2$. In Fig. 5, this simple solution is compared to the numerically obtained displacement of the right boundary of the shell, Δ_N . Figure 5 illustrates that, as seen in the figure, after the shell is formed and the analytical profiles are well established, its further acceleration proceeds in agreement with the 0D prediction.

Let us test the theoretical prediction (33) for the in-flight thickness of the accelerated shell. In our units, for the case of $b(t) = \theta(t)$, we obtain

$$a(t) = \sqrt{\frac{2t}{Rm_{shell}}} \quad (55)$$

The shell thickness in the simulation could be estimated from the magnetic field and density profiles obtained numerically as the distance corresponding to an e -fold decrease of the corresponding variable from its peak value at the boundary,

$$\delta_B \equiv x|_{B=B_{max}} - x|_{B=B_{max}/e}, \quad \delta_\rho \equiv x|_{\rho=\rho_{max}} - x|_{\rho=\rho_{max}/e} \quad (56)$$

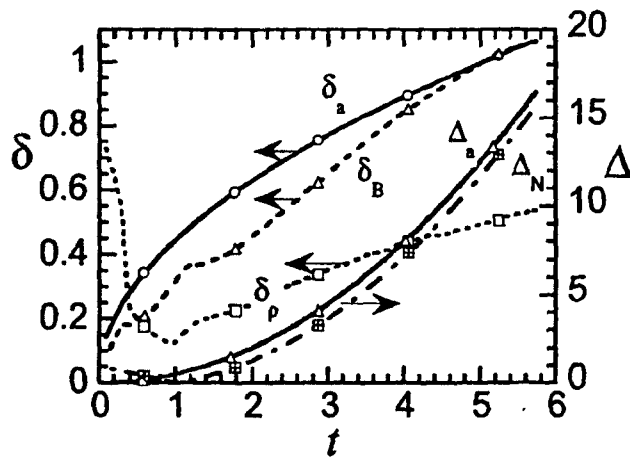


FIG. 5. Comparison of analytically and numerically calculated time variation for the plasma shell thickness [$a(t)$ given by (55) vs numerical estimates of the skin depth $\delta_B(t)$ and the shell thickness $\delta_\rho(t)$ (56)], and the distance traveled by the shell [$\Delta_a(t)$ is an analytical 0D prediction, $\Delta_N(t)$ is the numerical displacement of the right boundary of the shell].

The former estimate corresponds to the formula (55) in the theory; the latter, as demonstrated by Eq. (30), to a half of this thickness.

Figure 5 demonstrates that although the theoretically predicted exponential profiles emerge in the simulations almost immediately, the effective thickness of the shell, estimated as δ_B or $2\delta_\rho$, approaches the corresponding theoretical prediction, $a(t)$, somewhat later, by $t=4-5$.

Finally, at $t > 5$, after the shell has propagated more than 10 times its initial thickness, both the profiles of density and magnetic field and the shell thickness reproduce those found analytically. This is demonstrated by Fig. 6, where the profiles are plotted at the time when the accelerated boundary of the shell has propagated 12 times its initial thickness ($\Delta_N = 12$). For a wide range of magnetic Reynolds numbers, the density and magnetic field profiles are seen to reproduce the theoretical exponential shapes. This figure shows that even for a relatively low magnetic Reynolds number, $Rm_{shell} = 0.5$, with initial thickness of the shell smaller than the skin depth, the plasma shell still confines the driving magnetic flux quite well. However, a small but noticeable part of the magnetic flux is seen to break through the shell during its formation and appears in between the shell and the stator (located at $x_{stator} = -70$, not seen in the figure). The time $t = t^*$ it takes for the shell to reach $x = -12$ exhibits a weak dependence on the plasma conductance (magnetic diffusivity). The difference in t^* appears during the shell initiation, when the center-of-mass displacement still depends on the magnetic field gradient value. Further on, the center-of-mass coordinate varies as t^2 , as it should be. The numerical shell thickness estimated for the conditions of Fig. 6 from Eqs. (56) is in all cases very close to the analytical estimate (55).

To test the theoretical predictions for the waveforms of the driving magnetic field, which are different from a step function, we choose $Rm_{shell} = 10$ and make the calculation taking in (53) $b(t) = t/10$ (linearly growing drive) and $b(t) = 10/(t+10)$ (decreasing drive). In Fig. 7, we compare these two cases with the above case of a constant drive, $b(t)$

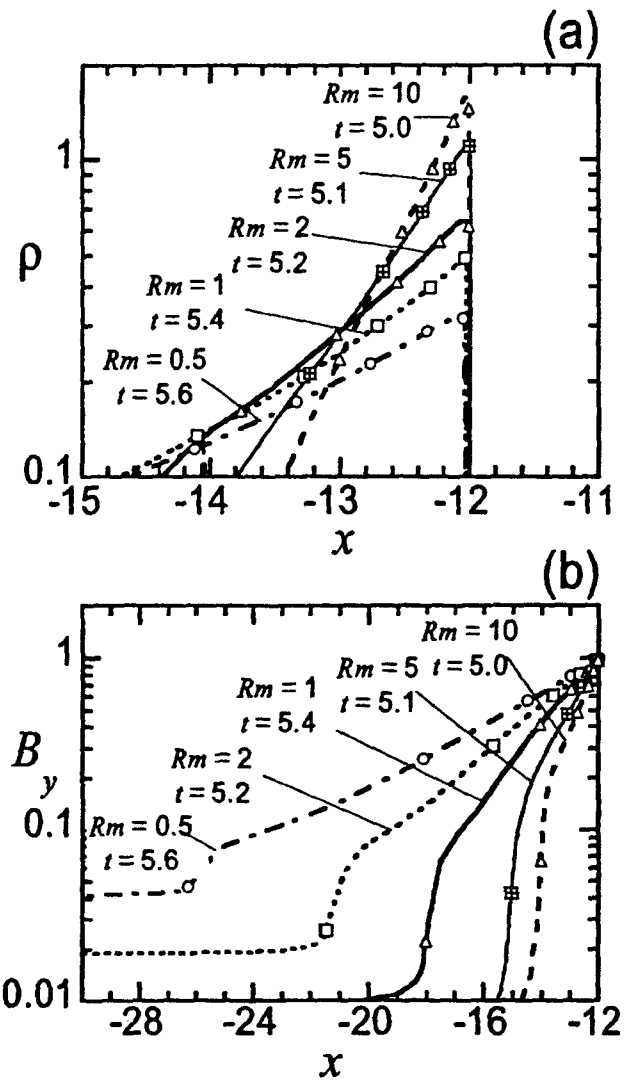


FIG. 6. Density (a) and magnetic field (b) profiles at the times when the right boundary of the shell reaches $x = -12$ for the same conditions as in Figs. 3-5 with the shell magnetic Reynolds number Rm_{shell} varied.

$= \theta(t)$, for two initial density profiles (flat and linear, as in Fig. 4) at the time when the accelerated boundary of the shell reaches $x = -12$. For all cases, the theoretical exponential profiles are reproduced. For the cases of constant, linearly increasing and decreasing drive, the shell reaches this position at $t^* = 5, 11$, and 6 , respectively. Substituting these values of $t = t^*$ into the first, second, and third lines in the right-hand side of Eq. (33), respectively, we find that the theoretically predicted shell thicknesses should relate to each other for these cases as $1:\sqrt{11/15}:4\sqrt{3}/5$, that is, as $1:0.86:1.38$. The ratios estimated from the numerical profiles in Fig. 7 are $1:0.8:1.3$, again, in good agreement with the theory.

Figures 4 and 7 demonstrate that while the shell adjusts itself to the magnetic energy flow through it, the density and magnetic field profiles evolve to the same self-similar shape, "forgetting" much of the initial conditions.^{29,30} We extend this numerical study to investigate the 1D stability or "asymptotic attractor" property of the self-similar solution by testing whether it will evolve from the initial density distribution that is not a single shell at all. Let us start with a

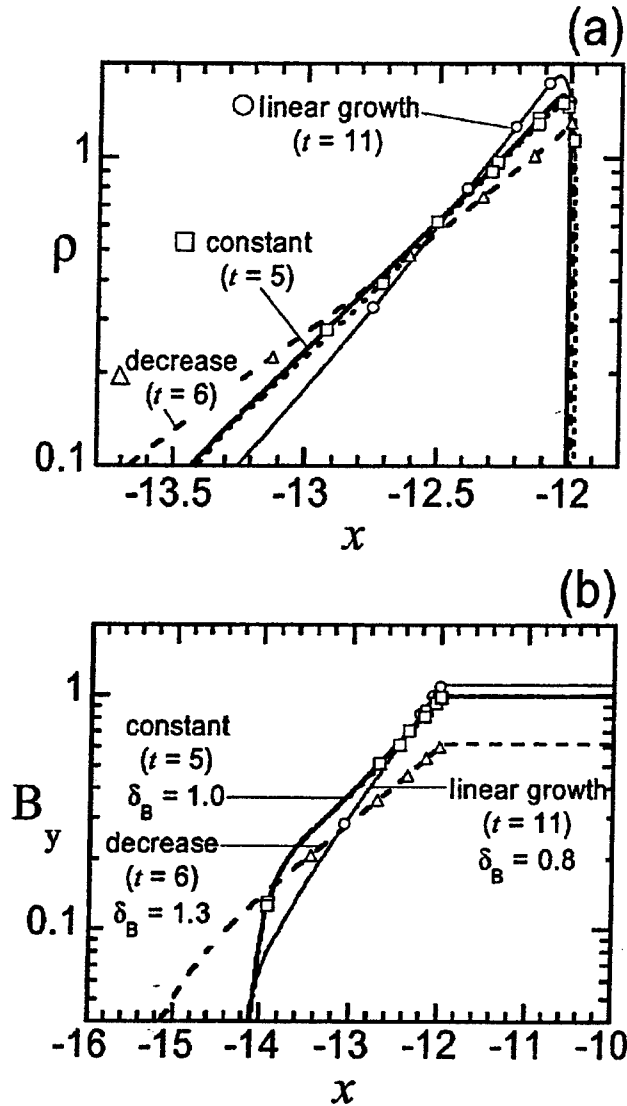


FIG. 7. Density (a) and magnetic field (b) profiles at the times when the right boundary of the shell reaches $x = -12$, as in Fig. 6, for $Rm_{\text{shell}} = 10$ and the waveform of the driving magnetic field varied. Two coinciding curves (squares) for a constant magnetic field drive correspond to the two different initial density distributions of Fig. 4.

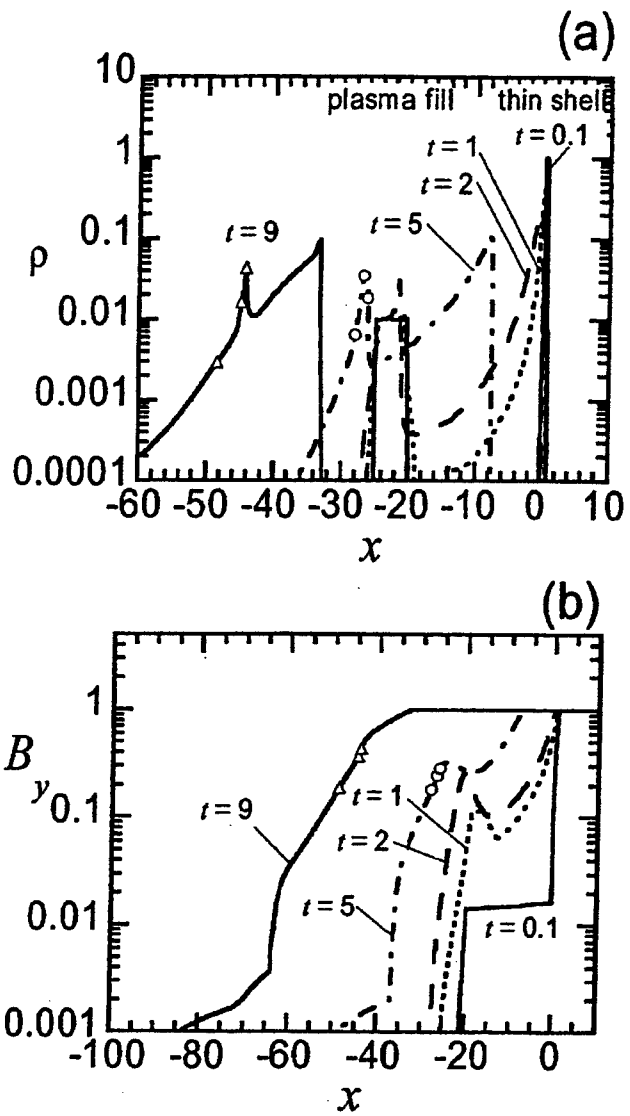


FIG. 8. Density (a) and magnetic field (b) profiles for a plasma load, which initially consists of a weakly conducting thin shell and a thicker low-density fill whose effective magnetic Reynolds number is 50 times higher (see profiles at $t = 0.1$). By $t = 9$, both components merge into a single plasma shell.

shell that consists of two parts, roughly modeling a nested wire array or a double-shell gas puff load.^{9,33} We split the plasma shell into two parts, placing the uniform outer shell with $\rho_{\text{shell}} = 1$ as in Fig. 2 and adding a low-density fill with uniform density $\rho_{\text{fill}} = 0.01$ between $x = -25$ and $x = -20$. The initial density distribution is very close to that shown in Fig. 8 for $t = 0.1$. For both the shell and the fill, we take $Rm_{\text{shell}} = Rm_{\text{fill}} = 0.2$. This means low conductivity of the shell, whose initial thickness and density are unity. For the fill, however, the dimensionless parameter Rm that enters Eq. (49) is much less than its effective magnetic Reynolds number. Indeed, combining the definitions (23) and (51), we find that $Rm \propto a_0 / \sqrt{\rho}$. The density of the fill is 100 times less than the shell density, and its thickness is 5 times greater, implying the value of the effective magnetic Reynolds number $Rm_{\text{fill,eff}} = 0.2 \times 50 = 10$. The shell, therefore, initially is relatively transparent for the magnetic flux, whereas the fill is not. We drive this system with a constant magnetic field,

$b(t) = \theta(t)$, and place the stator electrode very far to the left, at $x_{\text{stator}} = -700$.

If the shell were a solid conductor, the driving magnetic field would freely diffuse, leak through it, at $t > \sqrt{8\pi} \times Rm_{\text{shell}} \approx 1$. Then the shell would be shunted by the plasma fill, and the current switched to it. The effective magnetic Reynolds number for the fill is large; hence the magnetic field would accelerate the fill towards the stator. Since the fill mass is only 5% of the shell mass, it would fly to the stator, leaving the shell behind.

Figure 8 shows that it does not happen this way. It presents the simulated profiles of density and magnetic field at times varying from 0.1 to 9. At $t = 0.1$ the magnetic field already penetrates through the shell and reaches the fill, which has a thickness greater than the skin depth. At the same time, the shell also starts to expand with the velocity equal to a fraction of its center-of-mass velocity. As a result of this expansion, the heavier shell finally captures most of

the current by $t=5$, and the flux leaking stops. Before $t=5$, the magnetic field profile is nonmonotonic, exhibiting a peak in the fill plasma and a decrease towards the shell, where it increases again. This indicates a current reversal, a presence of a closed current loop produced by the compression of some magnetic flux diffused through the shell between the fill and the shell. Later, both parts of the initial density distribution merge, forming a single shell with a self-similar density profile (shown in Fig. 8 for $t=9$). We have therefore demonstrated a "1D stability" of the double-shell distribution: after some transient period, the two components coalesce into a single shell. This stability, demonstrated for the chosen value of the parameter $Rm_{\text{shell}}=0.2$, is not assured for an arbitrarily small value of this parameter. We have found that for a much more diffuse case, $Rm_{\text{shell}} \ll 1$, there is no stability, and the magnetic field diffused through the shell plasma can accelerate its inner part, forming a precursor flow.³⁴ Its description, however, is beyond the scope of the present paper.

We now compare confinement and compression of magnetic flux for the cases of one- and two-component magnetic field, the latter referring to all Z-pinch implosions involving B_z . The plasma shell is enclosed in a cavity bounded by two conducting walls. In addition to the stator located, as before, between $x=x_{\text{min}}$ and $x=x_{\text{stator}}$, the second stator is put on the right side of the computational area, between $x=x'_{\text{stator}}$ and $x=x_{\text{max}}$ (we take $x'_{\text{stator}}=29$). This configuration does not allow driving the plasma shell with an external generator, but we can introduce initial magnetic fields on both sides of the shell and follow their evolution.

We start with the case when the magnetic fields initially separated by the shell are parallel to each other: $B_y^{\text{left}}=0.25$, $B_y^{\text{right}}=1$. There is no field inside the shell initially. The pressure of the larger magnetic field from the right pushes the shell to the left, compressing the magnetic flux of the field to the left of the shell between the shell and the left stator. At the same time, the magnetic field between the shell and the right stator decreases due to expansion of magnetic flux. The increasing magnetic field on the left eventually exceeds the decreasing magnetic field on the right, starting to accelerate the plasma shell back, towards the right stator. This gives rise to oscillations, which are damped due to diffusion of magnetic flux through the shell.

Figure 9 shows the successive density and magnetic field profiles for $Rm_{\text{shell}}=2$. At $t=6.7$ the shell is accelerated towards the left (a). At $t=10$ the magnetic fields equalize from both sides of the shell and the magnetic energy is converted into the kinetic energy of the plasma, see also Fig. 10. At $t=18$ the shell stagnates at its extreme left position. The magnetic flux is compressed (b) and the magnetic field and density profiles are inversed, as was predicted analytically. At $t=26$ the shell has bounced, it travels back to the right and at $t=37$ comes close to its initial position. The exponential profiles are seen to form when the magnetic field is much higher on the one side of the shell than on the other.

Figure 10 shows the time evolution of magnetic and kinetic energy and magnetic fluxes on both sides of the shell. We estimate the relative role of energy dissipation by calculating the sum of magnetic and kinetic energy $E_m + E_m^{\text{plasma}}$

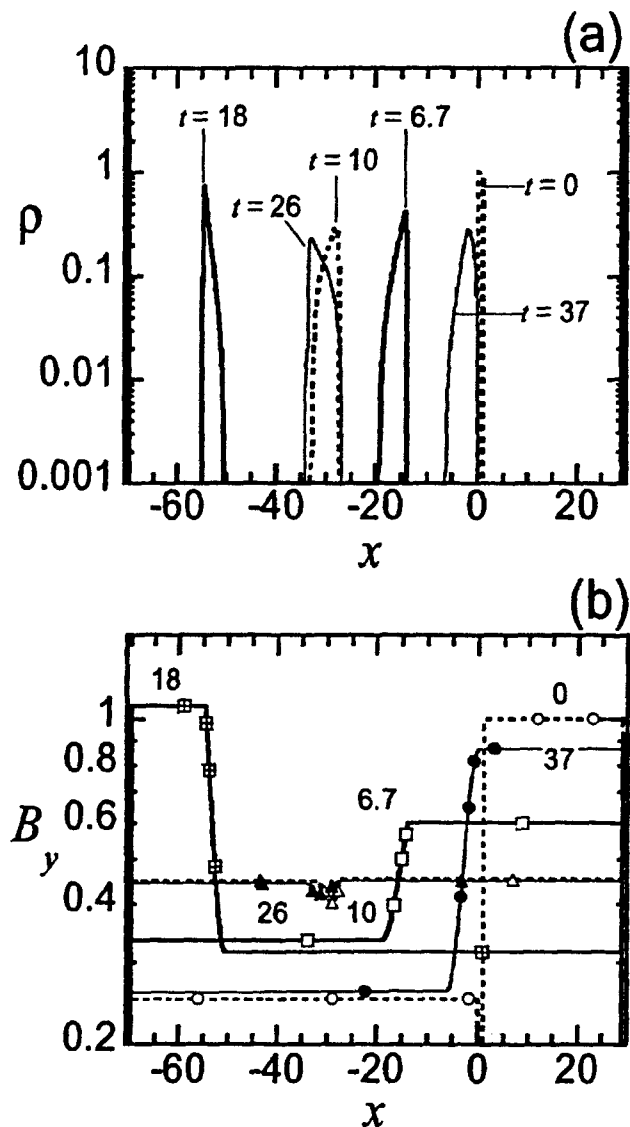


FIG. 9. Successive density (a) and magnetic field (b) profiles for a plasma shell confined in a conducting cavity with a one-component magnetic field, $B_{\text{left}} \parallel B_{\text{right}}$.

+ E_k (which in the absence of Joule losses must be equal to 1 at all time, with all the energies normalized with respect to the initial total energy). The deviation of this sum from unity turns out to be small, less than 10% after 3.5 full oscillations, at $t=60$, which demonstrates that the Joule energy losses are relatively low. The magnetic flux is seen to be pretty much conserved on each side of the shell, and the damping of the oscillations is very weak. This result is favorable for the one-component magnetic flux compression by a plasma shell, like the compression of azimuthal magnetic flux in the secondary circuit with the azimuthal magnetic field of the primary circuit.²⁰⁻²²

A different situation is found for the second case with $B_{\text{left}} \perp B_{\text{right}}$, as in the experiments where the initial axial magnetic field produced by a Helmholtz coil was compressed with the azimuthal magnetic field of the pinch current.¹³⁻¹⁷ We keep the initial and boundary conditions the same as in Figs. 9 and 10, and only change the direction of the initially larger magnetic field on the right, $B_y^{\text{right}}=0$,

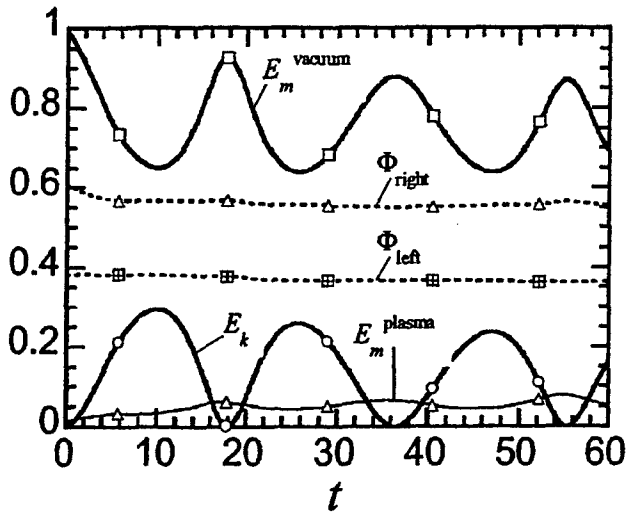


FIG. 10. Time evolution of magnetic fluxes Φ_{left} , Φ_{right} , magnetic E_m and kinetic E_k characteristic energies in the conditions of Fig. 9. Both the fluxes and the energies are normalized to the sum of their respective initial values in the cavity.

$B_z^{\text{right}} = 1$. Figure 11 shows the evolution of density and magnetic field profiles. Near the time of bouncing, when either $B^{\text{right}} \ll B^{\text{left}}$ ($t = 19$), or $B^{\text{right}} \gg B^{\text{left}}$ ($t = 42$), the profiles are still exponential, as they should be. The profiles are seen to be substantially different, however, when both components of the magnetic field are comparable ($t = 11$ and $t = 27$).

Besides, Fig. 12 shows that about one-third of the initial left magnetic flux is lost from the left side of the cavity through diffusion during the first deceleration, by $t = 19$, when the shell compresses B_y flux in the left semicavity, being driven by the pressure of B_z field from the right, in comparison to the case of parallel compressed and driving fields, where the losses of the left B_y flux during the first deceleration are almost negligible. Figure 12 also demonstrates that a two-component magnetic flux compression is not efficient even if the magnetic Reynolds number of the plasma shell is increased from 5 to 10. In a sense, this is consistent with the structure of inductance equation (21), which would have the same form for each of the two components of magnetic field, see (49). None of its solutions can satisfy $B = 0$ and $\nabla B = 0$ at the same time, ensuring a zero flux of magnetic energy through the plasma. Unless the exponential solution, with $B, \nabla B \rightarrow 0$ at $\eta \rightarrow \infty$ is valid for a sufficiently thick target (high effective value of Rm), as in most cases described above, fast losses of magnetic flux are inevitable.

IV. CONCLUSIONS

We have demonstrated that a magnetically accelerated low-beta plasma shell behaves as a self-regulating structure, which adjusts its thickness to the acceleration conditions so that the magnetic flux is confined even for relatively low values of magnetic Reynolds numbers. The case of one-component magnetic field exactly corresponds to the use of the pressure of the azimuthal magnetic field in the primary circuit in order to compress the azimuthal magnetic flux, and thereby amplify the current in the secondary circuit.²⁰⁻²² For

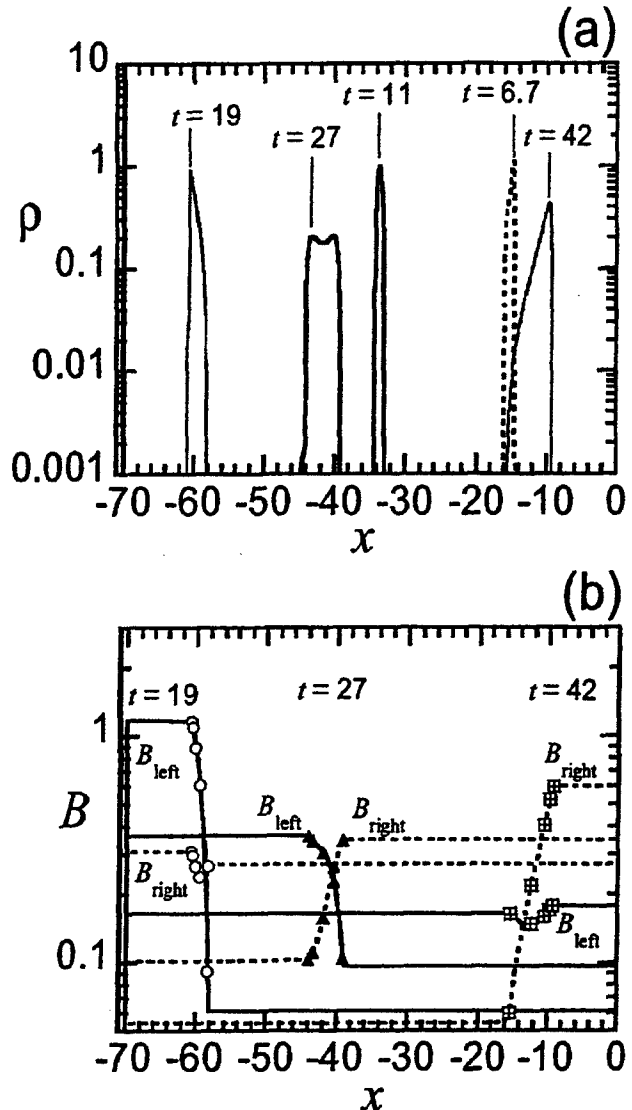


FIG. 11. Successive density (a) and magnetic field (b) profiles for a plasma shell confined in a conducting cavity with a two-component magnetic field, $B_{\text{left}} \perp B_{\text{right}}$.

this case, the profiles of density and magnetic field were shown to approach the asymptotic self-similar exponential profiles predicted by the theory. Transition to the same asymptotic profiles was demonstrated for plasma shells starting from a wide variety of initial conditions, including a plasma shell, which is initially split into two nested subshells. Confinement of magnetic flux was found to be less effective for the case of a two-component magnetic field, which corresponds to the Z-pinch implosions with B_z , as in Refs. 13-17.

The analytical and numerical problems addressed in this paper are highly idealized. Planar geometry and a considerably simplified physical model permitted us to find exact analytical solutions of some problems under study, and allowed us to use a relatively simple and robust numerical approximation technique for testing the theory. This is, in our opinion, a necessary step in the study of acceleration of plasma shells for the purpose of radiation production with magnetic field geometry different from that of a classical Z-pinch. Even a realistic, systematic 1D radiation-hydro-

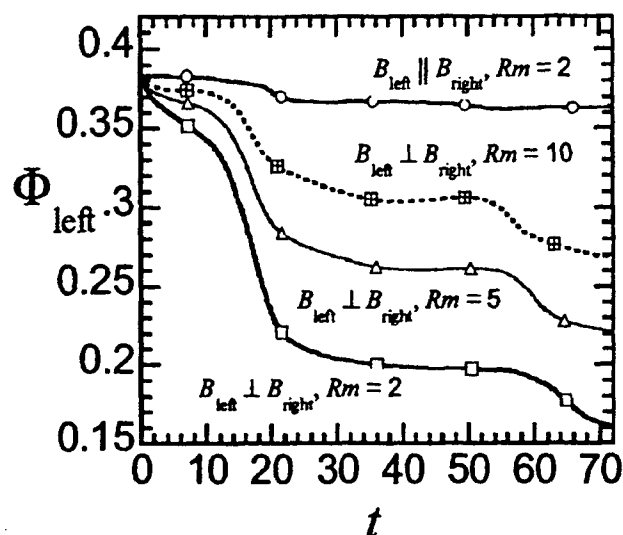


FIG. 12. Time evolution of magnetic flux in the left semicavity, Φ_{left} , for the conditions of Fig. 11 ($B_{\text{left}} \perp B_{\text{right}}$) at three values of magnetic Reynolds number. Confinement of the magnetic flux is not good even for the highest value of $Rm_{\text{shell}} = 10$.

analysis of Z-pinch implosions with B_z , has never, to our knowledge, been performed, to say nothing about adequate 2D modeling. A similar analysis is timely for the future experiments on keV radiation production based on the MFC approach.^{20–22} Basic physics established in the present work will be helpful for advancing in this direction.

ACKNOWLEDGMENTS

L.I.R. wishes to thank A. V. Gordeev for stimulating discussions of the issues of magnetic acceleration over many years. A.C. is grateful to V. A. Gasilov for many helpful discussions.

The work of L.R., A.V., and J.D. was supported by the U.S. Defense Threat Reduction Agency, the work of A.C.—by the French Centre National de la Recherche Scientifique (CNRS).

¹C. M. Fowler, W. B. Garn, and R. S. Caird, *J. Appl. Phys.* **31**, 588 (1960).

²A. D. Sakharov, R. Z. Lyudaev, E. N. Smirnov, Y. I. Plyushch, A. I. Pavlovskii, V. K. Chernyshev, E. A. Feoktistov, E. I. Zharinov, and Y. A. Zysin, *Sov. Phys. Dokl.* **165**, 65 (1965); A. D. Sakharov, *Phys. Usp.* **161**, 51 (1991) [reprinted from *Sov. Phys. Usp.* **88**, 725 (1966)].

³C. M. Fowler, *Physica B* **246**, 158 (1998).

⁴A. I. Bykov, M. I. Dolotenko, N. P. Kolokolchikov, V. D. Selemir, and O. M. Tatsenko, *Physica B* **294**, 574 (2001).

⁵H. Knoepfel, *Pulsed High Magnetic Fields: Physical Effects and Generation Methods Concerning Pulsed Fields up to the Megaersted Level* (North-Holland, London, 1970).

⁶E. I. Bichenkov, S. D. Gilev, and A. M. Trubachev, *J. Appl. Mech. Tech. Phys.* **5**, 125 (1980); K. Nagayama, *Appl. Phys. Lett.* **38**, 109 (1981).

⁷N. R. Pereira and J. Davis, *J. Appl. Phys.* **64**, R1 (1988).

⁸M. K. Matzen, *Phys. Plasmas* **4**, 1519 (1997).

⁹C. Deeney, M. R. Douglas, R. B. Spielman, T. J. Nash, D. L. Peterson, P. L'Eplattenier, G. A. Chandler, J. F. Seaman, and K. W. Struve, *Phys. Rev. Lett.* **81**, 4883 (1998); C. Deeney, C. A. Coverdale, M. R. Douglas, T. J. Nash, R. B. Spielman, K. W. Struve, K. G. Whitney, J. W. Thornhill, J. P. Apruzese, R. W. Clark, J. Davis, F. N. Beg, and J. Ruiz-Camacho, *Phys. Plasmas* **61**, 2081 (1999); H. Sze, J. Banister, P. L. Coleman, B. H. Failor, A. Fisher, J. S. Levine, Y. Song, E. M. Waisman, J. P. Apruzese, R. W. Clark, J. Davis, D. Mosher, J. W. Thornhill, A. L. Velikovich, B. V. Weber, C. A. Coverdale, C. Deeney, T. Gilliland, J. McGurn, R. Spielman, K. Struve, W. Stygar, and D. Bell, *ibid.* **8**, 3135 (2001).

¹⁰F. S. Felber, M. A. Liberman, and A. L. Velikovich, *Appl. Phys. Lett.* **46**, 1042 (1985).

¹¹G. E. Vekshtein, *Sov. Tech. Phys. Lett.* **10**, 319 (1984).

¹²A. L. Velikovich, S. M. Gol'berg, M. A. Liberman, and F. S. Felber, *Sov. Phys. JETP* **61**, 261 (1985); F. S. Felber, M. A. Liberman, and A. L. Velikovich, *Phys. Fluids* **31**, 3675 (1988).

¹³R. B. Baksht, A. L. Velikovich, B. A. Kablambaev, M. A. Liberman, A. V. Luchinskii, and N. A. Ratakhin, *Sov. Phys. Tech. Phys.* **32**, 145 (1987); F. S. Felber, F. J. Wessel, N. C. Wild, H. U. Rahman, A. Fisher, C. M. Fowler, M. A. Liberman, and A. L. Velikovich, *J. Appl. Phys.* **64**, 3831 (1988).

¹⁴F. S. Felber, M. M. Malley, F. J. Wessel, M. K. Matzen, M. A. Palmer, R. B. Spielman, M. A. Liberman, and A. L. Velikovich, *Phys. Fluids* **31**, 2053 (1988).

¹⁵L. I. Rudakov, in *Dense Z-Pinches*, 2nd International Conference on Dense Z-Pinches, Laguna Beach, CA, 1989, edited by N. R. Pereira, J. Davis, and N. Rostoker, AIP Conf. Proc. Vol. 195 (AIP, New York, 1989), p. 290.

¹⁶S. A. Sorokin and S. A. Chaikovskii, *Plasma Phys. Rep.* **22**, 897 (1996).

¹⁷A. V. Shishlov, R. B. Baksht, S. A. Chaikovskii, A. Y. Labetsky, V. I. Oreshkin, A. G. Roussikh, and A. V. Fedyunin, in *Dense Z-Pinches*, 5th International Conference on Dense Z-Pinches, Albuquerque, NM, 2002, edited by J. Davis, C. Deeney, and N. R. Pereira, AIP Conf. Proc. Vol. 651 (AIP, Melville, NY, 2002), p. 117.

¹⁸A. B. Bud'ko, F. S. Felber, A. I. Klee, M. A. Liberman, and A. L. Velikovich, *Phys. Fluids B* **1**, 598 (1989).

¹⁹H. U. Rahman, F. J. Wessel, and N. Rostoker, *Phys. Rev. Lett.* **74**, 714 (1995).

²⁰P. Monjaux, J. P. Bedoch, Y. Cazal, R. Lampes, A. Morell, and B. Roques, in *PPPS-2001: Pulsed Power Plasma Science 2001*, the 28th IEEE International Conference on Plasma Science and the 13th IEEE International Pulsed Power Conference, Rio Hotel in Las Vegas, Nevada U.S.A. 17–22 June 2001, edited by R. Reinovsky and M. Newton (IEEE, Piscataway, NJ, 2001), Vol. I, p. 310.

²¹J. F. Leon, R. B. Spielman, J. R. Asay, C. A. Hall, W. A. Stygar, and P. L'Eplattenier, in 12th IEEE International Pulsed Power Conference, Doubletree Hotel, 2 Portola Plaza, Fisherman's Wharf, Monterey, California U.S.A. 27–30 June 1999, *Digest of Technical Papers*, edited by H. Kirbie and C. Stallings (IEEE, Piscataway, NJ, 1999), Vol. I, p. 275.

²²P. L. Eplattenier, F. Lassalle, C. Mangeant, F. Hamann, M. Bavay, F. Bayol, D. Huet, A. Morell, P. Monjaux, G. Avriaud, and B. Lalle, in *Ref.* **17**, p. 51.

²³J. W. Thornhill, K. G. Whitney, and J. Davis, *J. Quant. Spectrosc. Radiat. Transf.* **44**, 251 (1990).

²⁴T. W. Hussey and N. F. Roderick, *Phys. Fluids* **24**, 1384 (1981).

²⁵A. G. Kulikovskii, *Dokl. Akad. Nauk SSSR* **114**, 984 (1957); F. S. Felber, *Phys. Fluids* **25**, 643 (1982); M. A. Liberman and A. L. Velikovich, *Nucl. Fusion* **26**, 709 (1986).

²⁶S. F. Grigor'ev and S. V. Zakharov, *Sov. Tech. Phys. Lett.* **13**, 254 (1987).

²⁷N. F. Roderick and T. W. Hussey, *J. Appl. Phys.* **59**, 662 (1986).

²⁸H. S. Carslaw and J. C. Jaeger, *Conduction of Heat in Solids* (Clarendon, Oxford, 1959).

²⁹G. Barenblatt, *Similarity, Selfsimilarity, and Intermediate Asymptotics* (Consultants Bureau, New York, 1979).

³⁰Ya. B. Zel'dovich and Yu. P. Raizer, *Physics of Shock Waves and High-Temperature Hydrodynamic Phenomena* (Dover, New York, 2002).

³¹A. A. Samarskii and Yu. P. Popov, *Finite-Difference Schemes for Gas Dynamics* (Nauka, Moscow, 1992) (in Russian); A. A. Samarskii, *The Theory of Difference Schemes*, Monographs and Textbooks in Pure and Applied Mathematics (Marcel Dekker, New York, 2001), Vol. 20.

³²V. A. Gasilov, A. S. Chuvatin, A. Yu. Krukovskii, L. E. Kartasheva, O. G. Olkhovskaya, A. S. Boldarev, D. S. Tarasov, N. V. Serova, S. V. Dyachenko, and O. V. Fryazinov, *Mat. Model.* **15**, 107 (2003) (in Russian).

³³Y. Song, P. Coleman, B. H. Failor, A. Fisher, R. Ingermansson, J. S. Levine, H. Sze, E. Waisman, R. J. Comisso, T. Cochran, J. Davis, B. Moosman, A. L. Velikovich, B. V. Weber, D. Bell, and R. Schneider, *Rev. Sci. Instrum.* **71**, 3080 (2000).

³⁴S. V. Lebedev, F. N. Beg, S. N. Bland, J. P. Chittenden, A. E. Dangor, M. G. Haines, S. A. Pikuz, and T. A. Shelkovenko, *Phys. Rev. Lett.* **85**, 98 (2000).

Chapter 5

Two and Three Wire Loads for Large Current Machines

5.1 Introduction

The use of a single wire load on large machines like "Z" is usually avoided due an excessive initial inductance and subsequent high voltages on upstream components. There is however a middle ground where a few larger wires can start well off axis and present much less initial inductance. Such loads will provide the lower inductance at the expense of more precursor plasma involvement.

In contrast to closed arrays with hundreds of fine wires, this relatively unexplored path to energetic implosions would use two or perhaps three load wires of appropriately heavier mass and aims to create a focused axial collision of dense wire cores amidst the assembled precursor plasma. The precursor, not confined by a cage of many wires, would presumably not much soften this collision.

Hence we must examine the trade between the implosion mass lost to precursor ablation and the mass available to deliver the wire core's kinetic energy.

A clear consequence of this load choice is a quite open geometry for which the transition to a highly conducting annular MHD plasma is neither an early nor a necessarily dominant feature of the electrodynamics. Generalizing slightly beyond MHD, we use a Lorentz gauge direct field solver to treat the TEM to TM mode set transition in the pinch region. The problem

is formulated using a scalar potential Φ and an axial vector potential A_z as unknowns, with the radial vector potential A_r being determined by the gauge constraint.

In contrast to earlier wire dynamic model (WDM) formulations with inductance matrix elements good only in the thin wire limit¹, the present work makes use of a new analytic Green's function for A_z that accounts for proximity effects among the wire cores and the return current structure.

The Green's function provides a first estimate for the axial vector potential solution $A_z(x, y)$ at the pinch midplane and the net load inductance arising among the heavy wire filaments. That solution is further refined by a current density source term representing the extended coronal plasma conductivity and flow.

The use of empirical mass source terms², for estimating the precursor mass ejection rate, ablative cooling rate, and ablation velocity, is then introduced to complete the picture.

5.2 Mathematical Formulation

There are two required innovations to carry out the desired calculations. First, we must go beyond the thin wire inductance limit, which is fine for wire core dynamics and current sharing, but starts to break down when the tenuous corona plasma jackets the wires and entrains current. Moreover, in the larger wires used for the loads we consider, proximity effects become noticeable as the wires approach one another. Hence a means of describing the extended conduction medium of the corona while maintaining contact with the lowest order inductive picture enforced by the wire cores is key to a versatile picture.

Second, we require a fluid description that admits a large adaptability in scale lengths in order to track the history of coronal plasma elements that drift radially to form the axial precursor. A smooth generalization of the discrete wire filaments into fluid particles allows a large dynamic range in mesh size for the field solver. The new fluid particle methods used here adapt easily to such grids because the projection of the fluid particle variables like density, velocity, and energy onto the Eulerian grid is virtually exact. The resulting errors in working with the tabular collisional radiative equilibrium (TCRE) algorithms will also be minimized.

5.2.1 Energy Transfer in a Circuit Model

For the original WDM the direct interaction among an ensemble of current elements is equivalent to a potential energy defined by the array inductance. Within the ensemble are symmetry groups of multiplicity S , e.g.

$$I = \sum_{i=1}^{N,S} J_{i,s} = I \sum_{i=1}^N S \alpha_i, \quad (5.1)$$

where α_i is any S -wise invariant current fraction contained in any particular wire path represented by a series resistance and inductance.

By construction then the sum of all α_i is one. Since the wire paths are in parallel, the voltage seen by each path α_i is equal in the absence of (small) wave transit time effects. If we examine the voltage $V_e(t)$ impressed at the entrance or feed of a wire array cage, then from the following figure, the resolution of the set α_i and the total current I admitted to the array are seen to be two distinct problems. From the view of the external generator $V_g(t)$, the array is a two terminal device and the energy into it must be the same for all sets α_i that show the same net impedance.

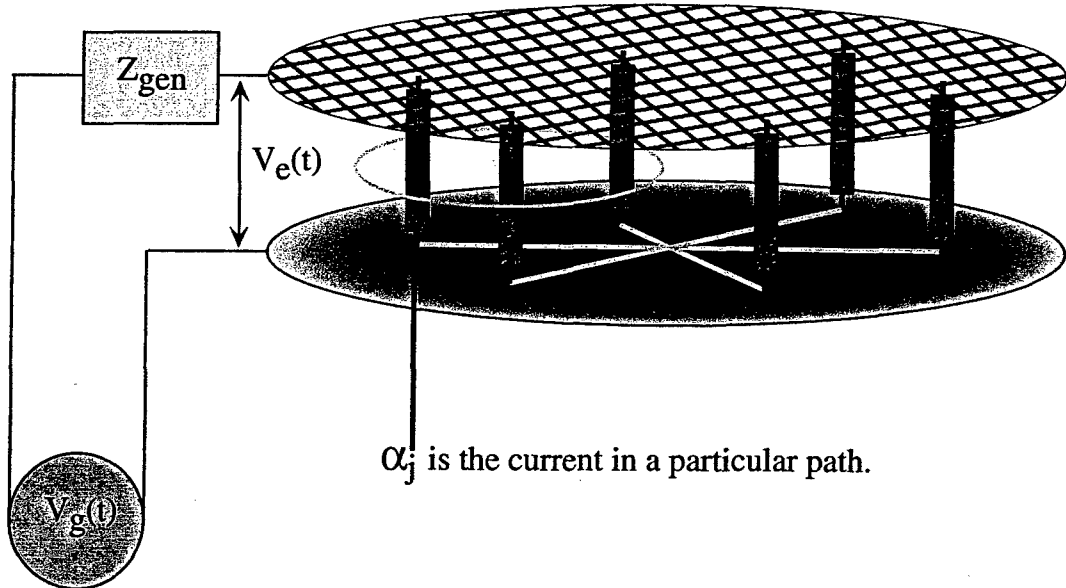


Figure 1. WDM circuit elements can decompose into symmetry groups, with each element representing a resistance and inductance.

As illustrated in Fig. 1, maintaining equal voltage at each circuit element, the equations fixing the current fractions α_i for any given $V_e(t) = V_g(t) -$

$Z_{gen}I$ and I can be written as,

$$V_e(t) = R_i(t)\alpha_i I + \left(\frac{d}{dt} \mathbf{L}_{ij} \cdot \alpha_j I \right), \quad (5.2)$$

and then integrated over a time interval $\delta \equiv \frac{V_e(t)}{dV_e/dt}$ to eliminate the time derivative. Denote by $\Delta\Psi_e$ the change in flux over this interval, and the matrix relation

$$\frac{\Delta\Psi_e}{I} \mathbf{u}_i = \delta R_j \mathbf{I}_{ij} \cdot \alpha_j + \mathbf{L}_{ij} \cdot \alpha_j \quad (5.3)$$

emerges, with \mathbf{I}_{ij} the diagonal identity matrix, \mathbf{u}_i a unit vector over the local group.

In the limit of vanishing inductance, or slow timescales ($\delta \gg L_i/R_i$), it is easy to see that the $\alpha_i = Z_{||}/R_i(t)$ and thus they clearly add up to unity.

5.2.2 Field Methods for Open Geometries

Loads with fewer wires using larger initial wire diameters and load radii will present a lower initial inductance at the expense of more precursor plasma involvement. In contrast to closed arrays with hundreds of fine wires, this very open field geometry is positioned on the edge of validity for a conventional inductance and MHD picture due to the large dynamic range in scale lengths and magnetic Reynolds number. The limit of spatially constant voltage throughout the corona is probably pretty good but by no means certain.

Mode Transitions from TEM to TM

With $Z_o = \sqrt{\epsilon_o/\mu_o} = 367.7\Omega$, an inlet TEM boundary condition on the scalar potential $\Phi(r, z, t)$

$$V_{in} = Z_L I_c = \left[\frac{Z_o}{2\pi} \ln\left(\frac{r_{>}}{r_{<}}\right) \right] I_c, \quad (5.4)$$

determines all the fields near the inlet, where $\mathbf{A} \rightarrow 0$.

Elsewhere, the time integral of the scalar potential forms a useful generalization of the familiar inductive "flux function", viz. let $\Psi(r, z, t) = \int^t dt_1 \Phi(r, z, t_1)$, and

$$\Psi(r_>) - \Psi(r_<) = \int_{r_<}^{r_>} \mathbf{A}_r(z_c, r_1, t) dr_1, \quad (5.5)$$

$$\Psi(z_>) - \Psi(z_<) = \int_{z_<}^{z_>} \mathbf{A}_z(z_1, r_c, t) dz_1, \quad (5.6)$$

on radial z_c and axial r_c conductor boundaries to ensure that the tangential component of electric field vanishes.

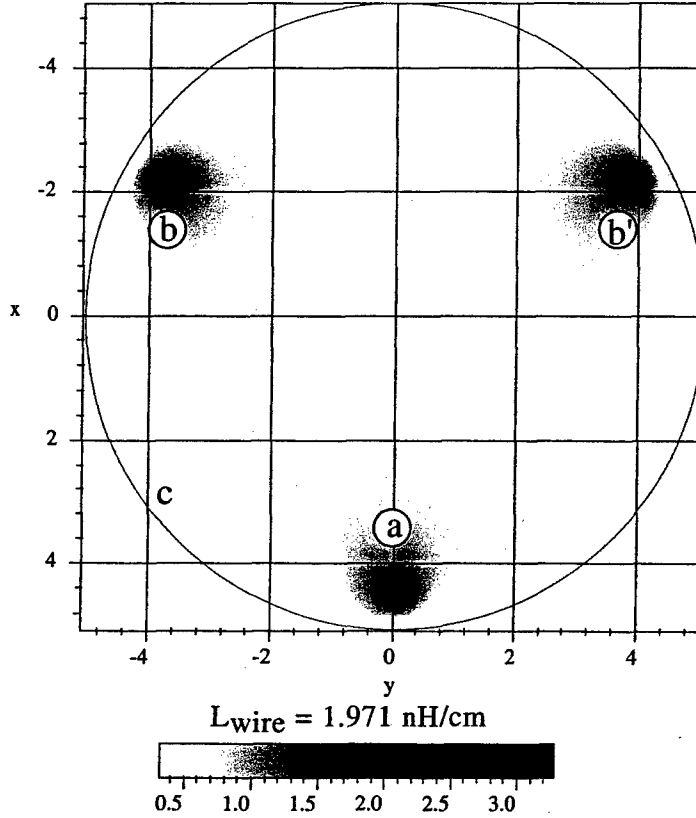


Figure 2. Three 1000 μm Wire Vector Potential $A_z(x, y)$

Utility of the Lorentz Gauge

The Lorentz gauge condition choice

$$r^{-1} \partial_r (r \mathbf{A}_r) + \partial_z \mathbf{A}_z + c^{-2} \partial_t^2 \Phi \equiv 0, \quad (5.7)$$

allows the dynamics to concentrate on the solution of $\mathbf{A}_z(z, r, t)$ only. One may in fact examine only two coupled wave equations for the needed fields.

$$\nabla^2 \Phi - c^{-2} \partial_t^2 \Phi = 0, \quad (5.8)$$

$$\nabla^2 \mathbf{A}_z - c^{-2} \partial_t^2 \mathbf{A}_z = -\mu_o \mathbf{J}_z, \quad (5.9)$$

with the axial current density near the wires given by

$$\mathbf{J}_z = \sigma_{\perp} [\mathbf{E}_z + \mathbf{V}_r \times \mathbf{B}_{\theta}(\mathbf{A})] . \quad (5.10)$$

For the inhomogeneous wave equation involving $\mathbf{A}_z(x, y)$, a Green's function can be developed for the problem at the diode midplane which captures the proper boundary conditions on the outer return current surface and on the finite size conducting wire cores. The function can be built up piecewise from image currents generated by a source cylinder (a), any number of floating cylinders b, b', ... and the return cylinder (c),

$$\begin{aligned} \mathcal{G}(x, y|s = a, b, b' \dots) = & g_a(x, y) + g_b(x, y) + \\ & g_{b'}(x, y) + g_{xb}(x, y) + g_{xb'}(x, y) + \dots , \end{aligned} \quad (5.11)$$

and over the symmetry groups $\mathbf{A}_z(x, y) = \Sigma_s \mathcal{G}(x, y|s)$. This \mathbf{A}_z "diagonalizes" the inductance matrix.

An example is shown in Fig. 2 above with quite large wires close to the return current can where the thin wire inductance would be inaccurate.

Variational Form of the Field Problem

The dimensionless spatial variables are based on a characteristic time t_o of the input pulse line, $\lambda_o = ct_o$, and a skin depth $\delta_o = \sqrt{\frac{2t_o}{\mu_o \sigma_{\perp}}}$.

With $\mathcal{E}_z = t_o \mathbf{E}'_z$, action integrals advance all fields,

$$\mathcal{L}(\Phi) = \int d\tau dA [(\nabla \Phi)^2 - (\partial_{\tau} \Phi)^2] , \quad (5.12)$$

$$\mathcal{L}(\mathbf{A}_z) = \int d\tau dA \left[(\nabla \mathbf{A}_z)^2 - (\partial_{\tau} \mathbf{A}_z)^2 - \mathbf{A}_z \left(\frac{2\lambda_o}{\delta_o} \right)^2 \mathcal{E}_z \right] . \quad (5.13)$$

The finite element (FE) representation employs value and time derivative degrees of freedom, e.g. $\vec{\Phi} = [\Phi, \partial_{\tau} \Phi]$. The variation

$${}_{i+1} \mathbf{W}_{i+1} \cdot {}^{i+1} \vec{\Phi} + {}_{i+1} \mathbf{W}_i \cdot {}^i \vec{\Phi} + {}_{i+1} \mathbf{W}_{i-1} \cdot {}^{i-1} \vec{\Phi} \equiv 0 , \quad (5.14)$$

is equivalent to solving the PDE problem (Eqn. 12). The symmetric positive definite weight matrices have the general form, ${}_i\mathbf{W}_m = T_{lm} \otimes (G_x + G_y)\lambda_o^2 - T'_{lm} \otimes V$ with integrals of squared time values T , time derivatives T' , spatial gradients G , and spatial values V taken over each cell. A similar formulation resolves Eqn. 13, here $\vec{A} = [A_z, \partial_\tau A_z]$

$${}_{i+1}\mathbf{W}_{i+1} \cdot {}^{i+1}\vec{A} + {}_{i+1}\mathbf{W}_i \cdot {}^i\vec{A} + {}_{i+1}\mathbf{W}_{i-1} \cdot {}^{i-1}\vec{A} \equiv \vec{S} \cdot \vec{\mathcal{E}}(\vec{A}, \vec{\Phi}), \quad (5.15)$$

with $\mathcal{S} = (\frac{4\lambda_o^2}{\delta_o^2})T_{lm} \otimes V$ and $\mathcal{E} = t_o(-(\frac{1}{\lambda_o}\partial_\tau A_z + \partial_z \Phi) + \mathbf{V}_r \times (\nabla \times \mathbf{A}))$. With the equation for Φ homogeneous, the potential variable can actually be replaced by its axial derivative, the static electric field component, $-\partial_z \Phi$.

5.2.3 Particle Methods

An early formulation³ of the fluid particles we want used freely drifting particles only and focused on particle annihilation and creation rules to track emerging features.

The novel particle solutions used here are drift kinetic fluid particles (DKFP) and track precisely the distribution function evolving under the action of the drift velocity \mathbf{C} and acceleration \mathbf{A} which are functions of local position \mathbf{x} , $\mathbf{C} = \mathbf{V} + \mathbf{x} \cdot \delta/h$, $\mathbf{a} = \mathbf{A} + \mathbf{x} \cdot \alpha/h$.

These DKFP contain three common factors which represent the dilation of the initial size (due to the shear in the velocity and acceleration), and the (asymmetric) movement of the initial domain boundaries. For a 1D particle class these are:

$$D(t) = (1 + \frac{t\delta}{h} + \frac{1}{2} \frac{t^2\alpha}{h}), \quad (5.16)$$

$$h_\pm(t) = \pm h + (V + \pm\delta)t + \frac{1}{2}(A + \pm\alpha)t^2. \quad (5.17)$$

The expected profile for number density (per unit length, area, or volume) $n(X, t) \equiv \langle N \rangle / \ell$ is then:

$$n(X, t) = \frac{N}{2hD(t)} \left(\text{erf} \left(\frac{(h_+(t) - X)}{\sqrt{2}Ut} \right) + \text{erf} \left(\frac{(X - h_-(t))}{\sqrt{2}Ut} \right) \right) \quad (5.18)$$

with similar expressions for momentum and enthalpy. The fluid properties, needed by the electrodynamics to support the evaluation of a magnetic Reynolds number ($\mathcal{R}_m = 2\ell_B t_o V_r / \delta_o^2$) and the source term above, are then easily projected into each node or cell of the field solution grid with virtually no error.

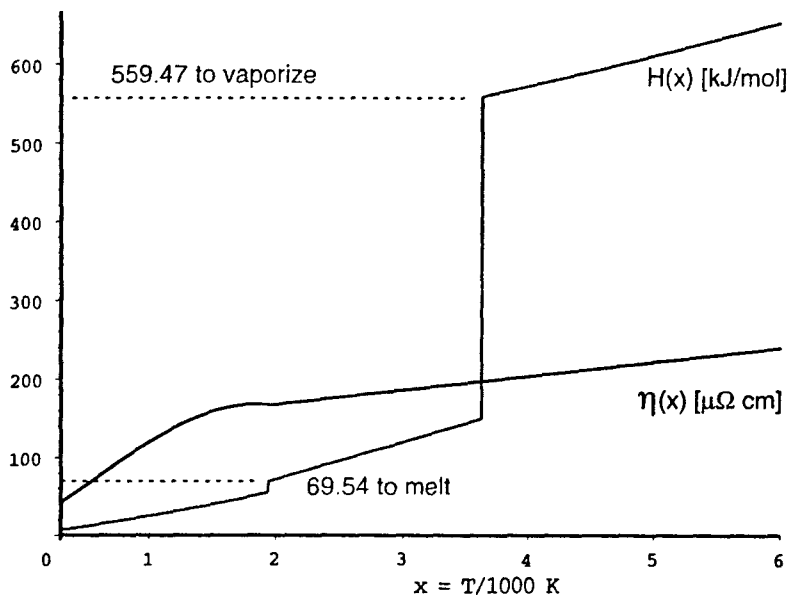
Source Boundary Conditions at the Wire Core

The detailed accounting of material phase changes as the wires vaporize and ionize is left to future refinements. A reasonably simple and apparently accurate approximation is to balance the force of the wire core attraction with a "rocket" force due to the inward flow of coronal plasma². Here a strict balance is too specialized, for what is needed is a path to account for wire loads that do not hang at the initial radius until they virtually disintegrate. From earlier work⁴ we know that Al foil switches exhibit an areal mass loss rate that scales directly with the surface magnetic energy density, viz. $\partial_t m = -\kappa \frac{B^2}{8\pi}$, and a flow velocity determined by a sound speed⁵ or, as seen for switch foils, an Alfvén speed characterized by the local field. Here the "private flux" near the wire plays the same role and this leads to a mass loss estimate, for a wire of length ℓ and radius r_{wire} , that scales like

$$\dot{m} \approx 10\kappa(\ell/r_{wire})I_{[MA]}^2[\mu g/ns] . \quad (5.19)$$

Typical values for κ are [5-25] $\mu g cm/ergs$ and we find that, in keeping with the other models cited here, only a small fraction of the wire current ($\approx 10^{-2}$) can be viewed as directly participating in any core erosion process.

Low Pressure Enthalpy and Resistivity for Titanium
linear $\eta(H)$ implies progressive wave solutions



The larger current fraction must be concentrated outside the core in the vapor and plasma emitted by the wire. If in fact the material outside the wire tends to a state such the magnetic Reynolds number is about one, then a similar analysis reveals that

$$\dot{m} \approx (\ell/41.09Z \ln \Lambda \alpha_{\perp}(Z, \omega\tau)) I_{[MA]}^2 T_e^{3/2} [\mu g/ns] . \quad (5.20)$$

The expected resistivity of the wire core can be modeled as a function of absorbed enthalpy $H(x)$ as shown above in Fig. 3. At the larger temperature values on this plot we join the TCRE model table for radiation and transport functions, using a magnetoplasma conductivity rather than $\eta(H(x))$.

Magnetoplasma Conductivity and Effective Resistance

The Epperlein-Haines⁶ formulation for the required skin depth δ_o in the wire corona can be written

$$1/\sigma_{\perp} \equiv \eta_{\perp} = \eta_0 \alpha_{\perp}(Z, \omega\tau) \quad (5.21)$$

with, $\alpha_{\perp}(Z, \omega\tau)$ a rational function, and

$$\eta_0 \equiv \left[\frac{m_e}{e^2 n_e \tau_e} \right] = 1.147519 \cdot 10^{-14} \frac{Z \ln \Lambda}{T_{[eV]}^{3/2}} [s]. \quad (5.22)$$

Using the resistivity of Fig. 3 for the core and this formulation for the ablative corona, the parallel combination of resistances becomes

$$R_{eff} = \frac{R_{core}(\eta(x))}{(1 + \frac{12\eta(x)}{\eta_{\perp}(x_{TCRE})})^2} [\Omega] , \quad (5.23)$$

and determines the ohmic heating rate for the core material consistent with the mass loss model.

As needed in the A_z source term for the coronal plasma,

$$\left(\frac{\lambda_o}{\delta_o} \right)^2 = 1.218472 \cdot 10^{-2} \frac{\lambda_o^2}{2t_o \ln \Lambda} \frac{T_{[eV]}^{3/2}}{Z \alpha_{\perp}(Z, \omega\tau)} \quad (5.24)$$

is the (dimensionless) equivalent, for a fiducial time t_o .

5.3 Early Inductance And Stagnation Energy

First we have examined the question of initial inductances for loads that might be contemplated on larger machines like "Z". For 1,2, and 3 wire loads set at 0.9 of the return current radius, one sees quite favorable inductances for diameters near or above $100\mu\text{m}$.

In the following Table 1, the subscripts on the inductance denote the number of wires and the larger masses implied for diameters above $100\mu\text{m}$ clearly would not be viable implosion loads, but here hollow loads of large radius and lower mass should be examined. The advantages of larger radius will also be reflected in the mass ablation and core cooling rates.

Clearly once two or three wires are used the initial inductance is quite modest and, as expected, this presents no noticeable voltage load for the run down phase of the implosion.

Table 1. Initial Inductances and Masses for Ti Loads

Dia. μm	L_1 $\frac{\text{nH}}{\text{cm}}$	L_2 $\frac{\text{nH}}{\text{cm}}$	L_3 $\frac{\text{nH}}{\text{cm}}$	Mass $\frac{\mu\text{g}}{\text{cm}}$
1000	5.88	2.95	1.97	...
500	7.27	3.64	2.43	...
200	9.11	4.56	3.05	1,426
100	10.49	5.25	3.51	357
50	11.98	5.95	3.97	89.2
20	13.71	6.86	4.58	14.26
10	15.10	7.55	5.04	3.57

With a load mass m_i in μgm per wire, inductance L in nH, driver voltage V in MV, and pinch dimensions of length ℓ , and radius r_0 in cm, the available wire core energy at stagnation scales as,

$$K_{imp,2} = 522.4 \left(r_0 (m_i \ell)^{1/2} V/L \right) [kJ]. \quad (5.25)$$

One expects, $K_{imp,3} = \sqrt{4/3} K_{imp,2}$ for the three wires.

As shown in Table 2, in an initial survey of the expected behavior for these loads, the model was used in the limiting case of (small) fixed wire resistance

and a fixed mass erosion constant so that for given current histories smaller diameter wires would lose a higher mass fraction.

Table 2. Energy Transfers for Ti Loads

Dia. & Case μm — Z,DE	H_2 kJ	H_3 kJ	Mass μg
1000 — Z	428.2	591.6	1,125
500 — Z	552.6	802.2	1,125
200 — Z	631.8	1,017	1,125
100 — Z	662.4	1,004	1,125
100 — DE	78.8	94.47	180

The 2 and 3 wire loads were set at 0.8 of the return current radius, and run for a fixed mass erosion coefficient. On Z the optimizing 3 wire case picked the best final mass at implosion for the 200 μm case. The lower masses lost available stagnation kinetic energy due to mass ablation, the larger ones lost it due to poor machine coupling. On DE the wires were placed at 0.6 of the return current radius.

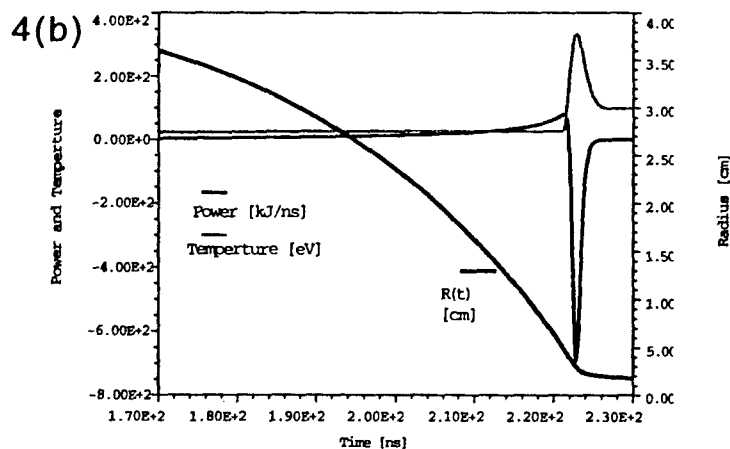
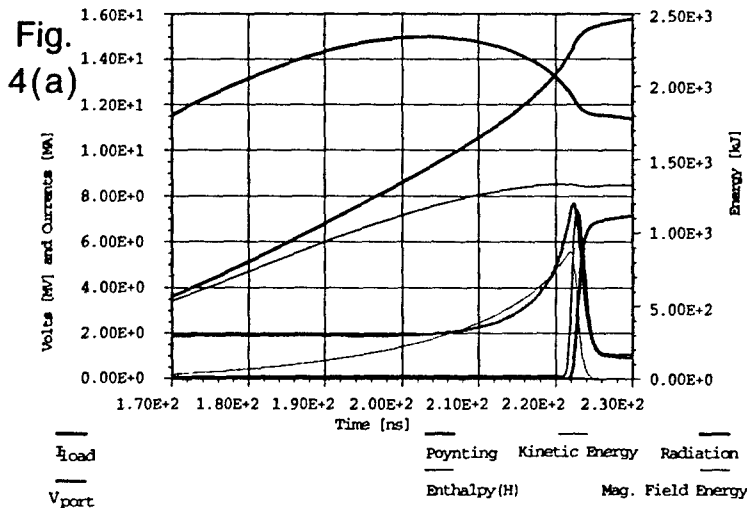
With a good load on "Z", Fig. 4(a,b) shows the radiation yield and power accessible in a high density stagnation, using the further features of TCRE radiation losses⁷ and an explicit calculation of the stagnation heating with viscous drag forces slowing the model wire cores. These very prompt and large heating rates are seen to extract over half the available energy (0.57) and show net cooling rates clearly comparable to expected stagnation heating rates. The achieved temperatures are also quite high enough to extract some K-shell radiation from the Ti load.

5.4 Conclusion

We have (i) modified the wire dynamic model (WDM) to the calculation of kinetic energy transfer to such low wire number loads on both Double Eagle and "Z" class drivers. and (ii) assessed the load energy and upstream voltages.

For DE any initial mounting of two or three 50 to 200 μm Ti wire loads at radii in excess of 0.6 of the return current radius will easily preclude early

voltages near the insulator stack from rising above one half the open circuit voltage as the load initiates and starts to run in. The best available kinetic energies are about 80 kJ for two wire loads, and about 100 kJ for three wire loads. The (60-80 $\mu\text{g}/\text{cm}$) masses required are typical for DE, the inductive current "bite" is clear.



For "Z" again initial mounting of similar wire loads at radii in excess of 0.6 of the return current radius will also keep early voltages in bounds. The best available kinetic energies are about 600 kJ for two wire loads, and about 100 kJ for three wire loads. The (250-375 $\mu\text{g}/\text{cm}$) masses used are an excellent match in "Z". In both cases the result of too much mass erosion is

to degrade the available kinetic energy at stagnation.

5.5 References

1. R. E. Terry, *et al*, Phys.Rev.Lett., **83**(21), 1999.
2. S. V. Lebedev, *et al*, Phys.Plasmas, **8**(8), 3744(2001).
3. W. Bateson and D. Hewett, JCP **144**, 358-378(1998).
4. J. E. Brandenburg, R. E. Terry, N. R. Pereira, "Mass Erosion in Foil Switches", *Fourth Int'l Conf on Megagauss Fields*, Plenum Press, New York, 1986, p.543.
5. M. G. Haines, Phys.Plasmas, **30**(2), 588(2002).
6. E. M. Epperlein and M. G. Haines, Phys. Fluids, **29**(4), 1986.
7. J. W. Thornhill, *et al*, Phys.Plasmas, **8**(7), 3480(2001).

Chapter 6

Flashover and Energy Coupling in the DQ Machine

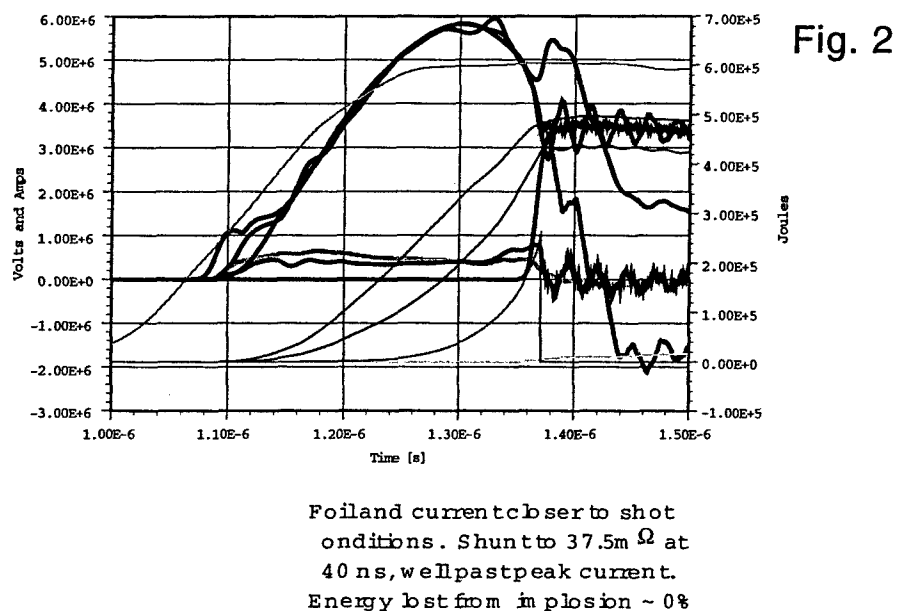
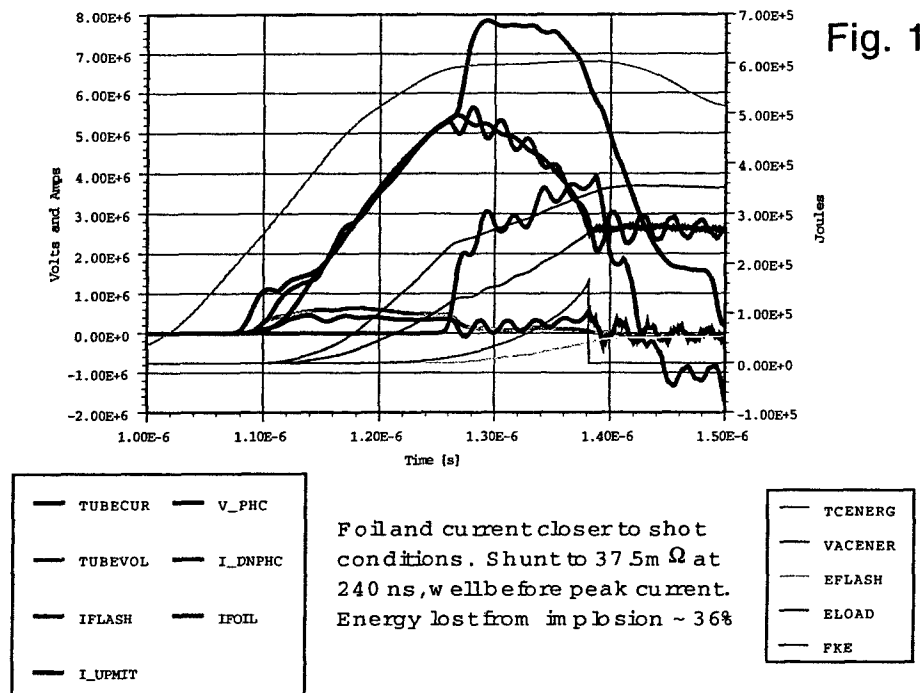
6.1 Observations and Analysis

The last experimental campaign on Decade Quad comprised a set of 7 gas puff shots, preceded by some wire calibration shots. For the gas puff series it would appear as if the insulator stack flashed over on all of them, although two of the shots had no "tube current" monitor working to confirm the event. When the tube current monitor was operating, all these events show a marked surge in the tube current and usually show an associated weakening of the downstream MITL and load currents. On one shot, 548, where both front and rear insulators appeared to flash and the tube current surge was the highest, the MITL and load currents appear to rise in late time. Such behavior could arise with a load plasma rebound against a fully closed short at the insulator stack that has electrically isolated the front end.

Within experimental uncertainty, the K-shell x-ray yields on these shots are quite comparable with earlier gas puff experience. In fact one of the best yields is seen on shot 548 with the strongest flashover event. So while it might be tempting to hope that the correction of such insulator breakdown will lead to a better performance, the studies summarized here show that, energetically at least, the flashover is too little, too late to be having any serious effect on the K-shell yield in these events.

The experimental implosions were examined with three distinct computational methods. First a transmission line code was set to model the insulator

breakdown as a time dependent shunt resistance which initiates at a fixed



time and drops its resistance to a specified asymptote. The upstream circuit

model includes the monitors for tube current and voltage, while downstream it is equipped with a MITL model and a Z-flow shunt which joins a post hole convolute model and a PRS load model.

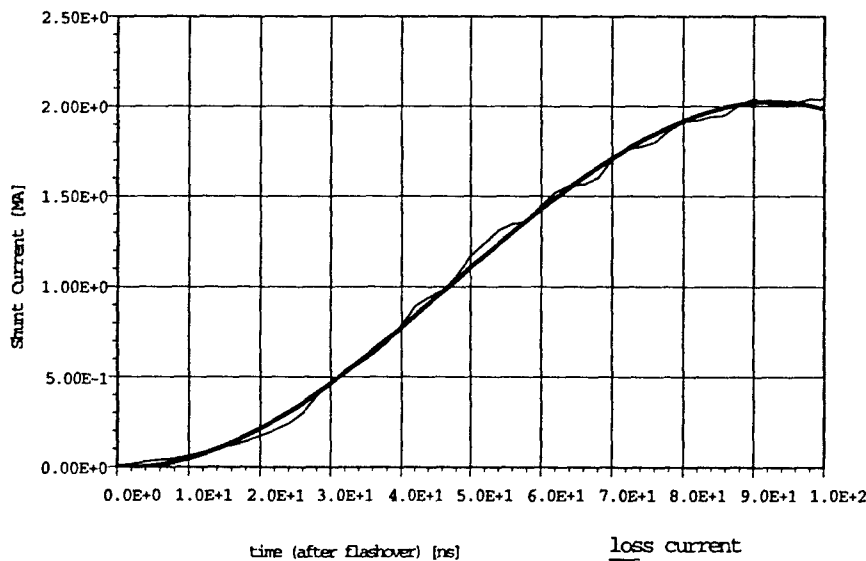
In the figures above note the tube current, foil current and voltage, the flashover current, the energy into the flashover, and the foil kinetic energy. An early flashover is shown to rob foil energy while a late one does not. Tube voltage suppression occurs to the same value for equal shunt impedance at either timing, but this is not a strong indicator. In Fig. 1, are the characteristics of an early breakdown with a large tube current surge; in Fig. 2, a breakdown in keeping with the experimental timing shows virtually no energy loss to the implosion.

The shunt $37.5m\Omega$ impedance used here was found to be about the best mimic of the experimental behavior allowing peak shunted currents on the order of 2 to 3 MA, and the decay time of the shunt resistor was kept short compared to the other timescales in the problem at about 2ns. Hence within the limitations of this single line circuit model, the flashover event is captured reasonably well.

Fig. 3 Decade Shot544:

Observed Loss Current Fit to a Cubic att= 1.590E-6 s

$$I(t) = -5.34263294E-6 * t^3 + 7.55674806E-4 * t^2 + -2.28795080E-3 * t$$



Alternatively, using the observed current loss from shot 544 (c.f. Fig. 3) instead of an arbitrary shunt resistance, the free variables are reduced to

only the breakdown time. The only modification of the equivalent circuit is to lower the "output voltage" by the machine impedance times the observed shunt current, viz.

$$V_{oc}(t) \mapsto V_{oc}(t) - Z_{eq}I_{obs}(t) , \quad (6.1)$$

with $I_{obs}(t)$ a known function of time as modeled in Fig. 3. In order to examine K-shell yield sensitivity rather than simple energy transfer the 1D code DZAPP was also applied to these cases and equipped with a standard equivalent circuit driver. Again, using the *experimentally observed current loss*, the shunt timing was the primary factor in setting the expected K-shell yield. An early shunt at 140 ns quenched the yield, while a late one (at 210 ns like in the experiment) showed virtually no effect.

Table 1. Shunt Effects with Shot 544 Loss Current

Shunt Time [ns]	Y_T kJ/cm	Y_K kJ/cm	Current [MA]
none	52.0	10.0	5.45
210	50.0	10.0	5.45
140	38.0	0.059	4.75

When the same model is applied in 2D, the Mach2 code shows the same result. These two cases differ only in that Fig. 4 has no shunt, while Fig. 5 uses the experimental trace and timing. The change in K-shell yield is almost imperceptible even though the late time currents and magnetic energy in the front end differ markedly.

6.2 Conclusions

From the foregoing analysis it would appear that DQ was not hampered significantly by the insulator flashover events, even though the yields were not much improved over earlier lower diameter nozzle shots. Insofar as the 2D calculation showed some Rayleigh Taylor modulation and some zippering (in keeping with the experiment) these effects alone were not enough to quench the K-shell yield. This is not to say that azimuthal perturbations and more

pronounced r-z perturbations, perhaps brought on by an asymmetric power flow from the flashover or a tube misalignment, could not account for the observed performance. Indeed since the one flashover event (548) that seems to have involved both front and back insulators showed a slightly enhanced yield, the largest tube current surge, and currents rising after compression in the load region, there is a strong anticorrelation of flashover with poor yield in the dataset! The fact that a clean strong flashover isolating the front end might have helped the pinch may indicate that tube misalignment is a good candidate problem area to clear. Perhaps the poor yields are arising in part from asymmetric power flow causing more zippering or other incoherent assemblies.

However, for the Decade Quad in the shot series examined here, what seems clear is that (i) the observed yield variations do not correlate well with "strong" or "weak" flashover events, and (ii) the general energetics and observed timings of the flashover events do not imply significantly lower yield expectations. Moreover, these conclusions are largely independent of the analysis scheme (0D, 1D, or 2D) used to examine the issue.

6.3 References

1. DQ Shot # 543-549 Data Package, Titan PSD, 13 Oct 03.
2. Loss Current, T. Holt and R.J.Commisso, NRL, 11 Dec 03.

Mach2 Analysis Without and With the 544 Shunt

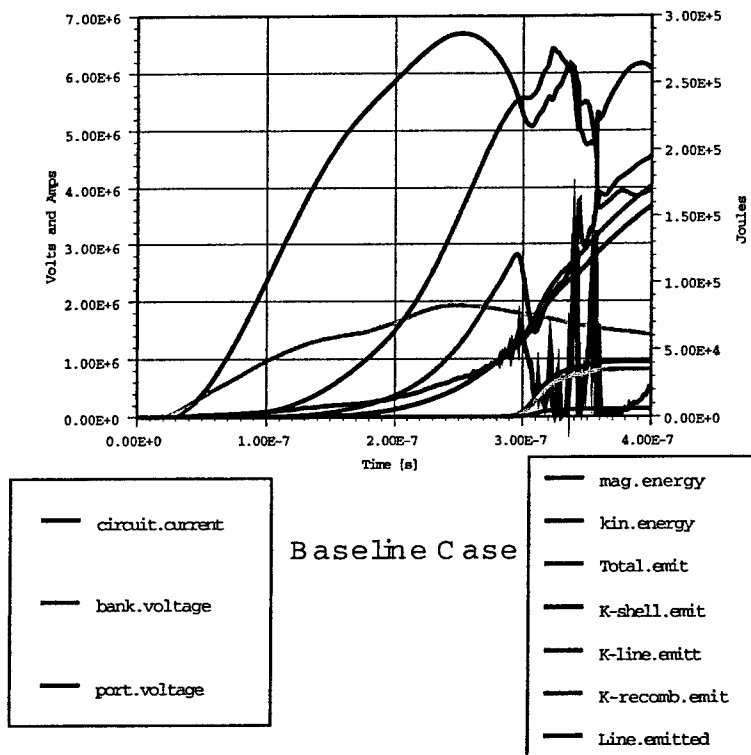


Fig. 4

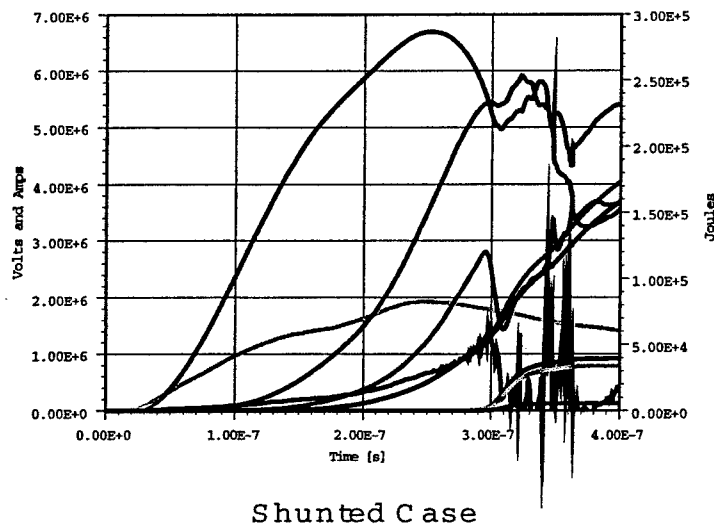


Fig. 5

Gas Puff Nozzle Design for Argon Z Pinches Using MACH2 Simulations

Final Report
Report 03-04

Sherry D. Frese, Gerald G. Craddock, Jr., and Michael H. Frese
Submitted October 14, 2003

Naval Research Laboratory
Contract No. N00173-03-P-6201

NumerEx

2309 Renard Place SE, Suite 220, Albuquerque, NM 87106-4259

505.842.0074